MALTE WROBEL

Fortschrittsberichte aus der Regelungstechnik
und Prozessautomatisierung

Band 02

MODEL- AND DATA-BASED ESTIMATOR AND CONTROL DESIGN FOR METAL FORMING PROCESSES

Karlsruher Institut für Technologie

Malte Wrobel

Model- and Data-Based Estimator and Control Design for Metal Forming Processes

Fortschrittsberichte aus der Regelungstechnik
und Prozessautomatisierung
Band 02

Herausgeber: Prof. Dr.-Ing. habil. Thomas Meurer

Model- and Data-Based Estimator and Control Design for Metal Forming Processes

by
Malte Wrobel

Karlsruher Institut für Technologie

Karlsruher Institut für Technologie
Institut für Mechanische Verfahrenstechnik und Mechanik

Model- and Data-Based Estimator and Control Design for Metal Forming Processes

Zur Erlangung des akademischen Grades eines Doktors der Ingenieurwissenschaften von der KIT-Fakultät für Chemieingenieurwesen und Verfahrenstechnik des Karlsruher Instituts für Technologie (KIT) genehmigte Dissertation

von Malte Wrobel, M.Sc.

Tag der mündlichen Prüfung: 30. Juli 2024
Erstgutachter: Prof. Dr.-Ing. habil. Thomas Meurer
Zweitgutachter: Prof. Dr.-Ing. Dr. h.c. Oliver Sawodny

Impressum

Karlsruher Institut für Technologie

Karlsruher Institut für Technologie (KIT)
Kaiserstraße 12
76131 Karlsruhe

Institut für Mechanische Verfahrenstechnik und Mechanik
www.mvm.kit.edu

2024

ISSN 2943-0887
DOI 10.5445/IR/1000174023

Preface

This dissertation is essentially based on the results of two research projects. In the project ZF4558805RU8 funded by the German Zentrales Innovationsprogramm Mittelstand (ZIM) the active thermal control for a deep drawing tool was developed. Here, I worked as part of the Chair of Automatic Control at Kiel University in cooperation with the companies Dornbusch GmbH and Hotset GmbH from May 2019 to December 2021. The implementation of a comprehensive property control in a multistage press hardening is the overall objective of the project 424334660 (Tekkaya/ Meurer) within the Priority Program SPP2183 ”Property-controlled forming processes” funded by the Deutsche Forschungsgemeinschaft (DFG). Here, I worked from January 2022 to January 2023 as part of the Chair of Automatic Control at Kiel University and from February 2023 until January 2024 as part of the Digital Process Engineering Group of the Institute of Mechanical Process Engineering and Mechanics at KIT. This project is a cooperation with the Institute of Forming Technology and Lightweight Components of Dortmund University. Experiments for the research projects were carried out at Dornbusch GmbH and at the Institute of Forming Technology and Lightweight Components of Dortmund University.

This work is mainly based on the following publications:

- M. Wrobel and T. Meurer. “Optimal Sensor Placement for Temperature Control in a Deep Drawing Tool”. In: IFAC-PapersOnLine 54.11 (2021). 6th IFAC Workshop on Mining, Mineral and Metal Processing, pp. 91–96. doi: 10.1016/j.ifacol.2021.10.056. [76]
- M. Wrobel and T. Meurer. “Optimal sensor placement and estimator-based temperature control for a deep drawing process”. In: Journal of Process Control 124 (2023), pp. 92–104. doi: 10.1016/j.jprocont.2023.02.014. [75]
- M. Wrobel, J. Martschin, T. Meurer, and E. Tekkaya. “Data-Driven Temperature Estimation for a Multi-Stage Press Hardening Process”. In: IFAC-PapersOnLine 56.2 (2023). 22nd IFAC World Congress, pp. 4252–4257. doi: 10.1016/j.ifacol. 2023.10.1785. [74]
- J. Martschin, M. Wrobel, J. Grodotzki, T. Meurer, and A. E. Tekkaya. “Soft Sensors for Property-Controlled Multi-Stage Press Hardening of 22MnB5”. In: Automotive Innovation 6 (2023), pp. 252–363. doi: 10.1007/s42154-023-00238-z. [46]
- M. Wrobel, J. Martschin, A. E. Tekkaya, and T. Meurer. “Data-based Control of a Multistage Press Hardening Process”. In progress.

This dissertation thesis is based on these publications and extends them by comprehensive supplementary information to derive and outline the main results.

Danksagung

Mein besonderer Dank gilt Herrn Prof. Dr.-Ing. habil. Thomas Meurer für die ausgezeichnete Betreuung bei der Durchführung der Arbeit. Hierbei sind die Unterstützung der Forschungsarbeit, die guten Arbeitsbedingungen, das außerordentliche Engagement und die Hilfsbereitschaft und Offenheit bei Fragen jeglicher Art zu nennen.

Mein Dank gilt auch Herrn Prof. Dr.-Ing. Dr. h.c. Oliver Sawodny für die Übernahme des Zweitgutachtens.

Ich danke der Dornbusch GmbH und der Hotset GmbH für die sehr gute Zusammenarbeit im Projekt ZF4558805RU8 des Zentralen Innovationsprogramms Mittelstand (ZIM).

Zudem danke ich Herrn Prof. Dr.-Ing. A. Erman Tekkaya und insbesondere Juri Martschin für die vertrauensvolle und erfolgreiche Zusammenarbeit im Projekt 424334660 (Tekkaya/ Meurer) des Schwerpunktprogramms SPP2183 ”Eigenschaftsgeregelte Umformprozesse” der Deutschen Forschungsgemeinschaft (DFG).

Außerdem bedanke ich mich bei den Kollegen und Kolleginnen der Lehrstühle ACON in Kiel und DPE in Karlsruhe für das gute Arbeitsklima. Mein besonderer Dank gilt dabei Dirk Wolfram, Marcel Jiokeng und Denis Ratke.

Abschließend bedanke ich mich bei Brit und meinen Eltern für die Unterstützung und das Verständnis.

Abstract

This work considers the model- and data-based estimation and control design for metal forming processes. It specifically addresses two distinct processes: deep drawing and multistage press hardening.

Deep drawing is an important technique for shaping flat sheet blanks. However, it poses challenges such as wrinkle formation and crack occurrence, especially in geometrically complex areas. To enhance material formability and reduce defects, this work focuses on precisely controlling the temperature of the deep-drawing mold's die. It employs a systematic placement of sensors to develop a spatial-temporal temperature estimator, which is subsequently utilized for tracking control through embedded actuation devices. This involves modeling the temperature distribution in the die as a continuum representation, which is then approximated using high-order finite element (FE) techniques to accommodate the tool's intricate geometry. Parameter identification is carried out based on measurement data to refine the FE model, and model order reduction (MOR) methods are applied to create a more manageable system representation. An optimization problem, incorporating observability Gramian variations, is formulated and solved to determine optimal sensor locations. Furthermore, a Kalman filter, based on a reduced order model, is designed, along with a linear-quadratic regulator that includes an integral component to efficiently respond to disturbances. Alternatively a proportional derivative controller is built. The proposed theoretical framework is finally validated in a real experiment.

In the context of multistage press hardening, where a sheet material undergoes rapid austenitization, tempering, stretch-forming, and die bending, the resulting product properties are influenced by the thermo-mechanical history. This work aims to estimate and directly control the spatial-temporal temperature distribution in the sheet by developing a data-driven estimation in order to control the product properties of the formed blanks. A data-driven dynamical model is constructed using dynamic mode decomposition (DMD) based on finite element simulation data. This model is further extended to account for variations in the process parameters like stroke rate, blank holder force, and austenitization temperature (parametric DMD). The approach is validated by comparing it with the original FE model, and model accuracy is improved through experimental analysis of the influence of process parameters. Various temperature measurement instruments are discussed, compared, and their dynamics is identified. To estimate the spatial-temporal temperature distribution, a Kalman filter is developed based on the parametric DMD model. A time-varying or stage-dependent output matrix is employed to account for different numbers and locations of thermocouples in the three stages. Optimal control strategies are then implemented to achieve desired temperature trajectories, allowing targeted manipulation of the blank's properties. Experimental validation of this system design and control strategy is carried out under real-time constraints.

In conclusion, this work provides a comprehensive framework for both deep drawing and multistage press hardening processes, with a focus on model- and data-based techniques to improve control and estimation, ultimately leading to enhanced product quality and reduced defects.

Zusammenfassung

Diese Arbeit befasst sich mit dem modell- und datenbasierten Schätzer- und Regelungsentwurf für Metallumformprozesse. Dabei geht es speziell um zwei unterschiedliche Prozesse: Tiefziehen und mehrstufiges Presshärten.

Das Tiefziehen ist eine zentrale Technik zur Erzeugung flacher Blechzuschnitte. Es birgt jedoch Herausforderungen wie Faltenbildung und Rissbildung, insbesondere in geometrisch komplexen Bereichen. Um die Formbarkeit des Materials zu verbessern und Defekte zu reduzieren, liegt der Schwerpunkt dieser Arbeit auf der präzisen Regelung der Temperatur in der Matrize des Tiefziehwerkzeugs. Dazu wird eine systematische Platzierung von Sensoren genutzt, um einen räumlich-zeitlichen Temperaturschätzer zu entwickeln, der anschließend zur Regelung durch eingebettete Aktuatoren verwendet wird. Dazu gehört die Modellierung der Temperaturverteilung in der Matrize in einer Kontinuumsdarstellung, die dann mithilfe von Finite-Elemente-Techniken (FE) höherer Ordnung angenähert wird, um die komplizierte Geometrie des Werkzeugs zu berücksichtigen. Zur Verfeinerung des FE-Modells erfolgt eine Parameteridentifikation auf der Grundlage von Messdaten und es werden Methoden zur Modellordnungsreduktion angewendet, um eine besser handhabbare Systemdarstellung zu erstellen. Ein Optimierungsproblem, das die Gramsche Beobachtbarkeitsmatrix einbezieht, wird formuliert und gelöst, um optimale Sensorpositionen zu bestimmen. Darüber hinaus wird ein Kalman-Filter basierend auf einem Modell reduzierter Ordnung sowie ein linear-quadratischer Regler entwickelt, der eine Integralkomponente enthält, um effizient auf Störungen zu reagieren. Alternativ wird ein Proportional-Differentialregler entworfen. Das vorgestellte theoretische Konzept wird schließlich in einem realen Experiment validiert.

Im Rahmen des mehrstufigen Presshärtens, bei dem ein Blechmaterial einer schnellen Austenitisierung, Temperierung, Streckformung und einem Gesenkbiegen unterzogen wird, werden die resultierenden Produkteigenschaften durch die thermomechanische Historie beeinflusst. Ziel dieser Arbeit ist es, die räumlich-zeitliche Temperaturverteilung im Blech mit Hilfe eines datenbasierten Schätzers zu rekonstruieren und direkt zu regeln, womit die Produkteigenschaften der geformten Bleche gezielt beeinflusst werden können. Ein datenbasiertes dynamisches Modell wird mithilfe der Dynamic Mode Decomposition (DMD) basierend auf FE-Simulationsdaten erstellt. Dieses Modell wird erweitert, um Prozessparameter wie Hubfrequenz, Niederhalterkraft und Austenitisierungstemperatur (parametrische DMD) zu berücksichtigen. Der Ansatz wird durch den Vergleich mit dem ursprünglichen FE-Modell validiert und die Modellgenauigkeit wird durch experimentelle Analyse der Einflüsse der Regelungsparameter verbessert. Verschiedene Temperaturmessinstrumente werden diskutiert, verglichen und ihre Dynamik identifiziert. Zur Abschätzung der räumlich-zeitlichen Temperaturverteilung wird ein Kalman-Filter auf Basis des parametrischen DMD-Modells entwickelt. Eine zeitvariable, stufenabhängige Ausgangsmatrix wird verwendet, um unterschiedliche Anzahlen und Positionen von Thermoelementen in den drei Stufen zu berücksichtigen. Anschließend wird ein optimaler Regelungsalgorithmus implementiert, um die gewünschten Temperaturverläufe zu erreichen und so die Eigenschaften des Blechs gezielt zu beeinflussen. Die experimentelle Validierung dieser Systementwurf- und Regelungsstrategie erfolgt unter Echtzeitbedingungen.

Zusammenfassend stellt diese Arbeit umfassende Strategien sowohl für den Tiefzieh- als auch für den mehrstufigen Presshärteprozess bereit, wobei der Schwerpunkt auf modellbasierten und datengetriebenen Techniken zur Verbesserung der Regelung und Schätzung liegt, was letztendlich zu einer verbesserten Produktqualität und weniger Fehlern führt.

Contents

Acronyms and Symbols

In the following only the most important acronyms and symbols are summarized.

Acronyms

FE	Finite element
PDE	Partial differential equation
ODE	Ordinary differential equation
MOR	Model order reduction
ROM	Reduced order model
SVD	Singular value decomposition
BT	Balanced truncation
IRKA	Iterative rational Krylov algorithm
POD	Proper orthogonal decomposition
DMD	Dynamic mode decomposition
DMDc	Dynamic mode decomposition with control
LQ	Linear quadratic
P(I)D	Proportional (integral) derivative
CAD	Computer aided design
TDC	Top dead center
BDC	Bottom dead center
PLC	Programmable logic controller

Symbols

$T(x,t)$	Temperature at point $x = (x_1, x_2, x_3)$ and time $t \geq 0$
ρ	Density
c_p	Specific heat
λ	Thermal conductivity
h	Convective heat transfer between steel and air
E	Thermal damping matrix
A	Thermal stiffness matrix
C	Output matrix
B	Input matrix
$\boldsymbol{T}$	Nodal temperature vector
$\boldsymbol{u}$	Input vector
$\boldsymbol{y}$	Output vector
E_r, A_r, B_r, C_r	Reduced order matrices
$\boldsymbol{T}_r$	Reduced nodal temperature vector
W_o	Observability Gramian
L	Static estimator gain matrix
τ_{cyc}	Stage time
τ_{Tr}	Transfer step time
τ_{Cl}	Closing step time
τ_{Fo}	Forming step time
τ_{Ho}	Holding step time
τ_{De}	Demould step time
τ_{Op}	Opening step time
f_{SR}	Stroke rate
F_{BH}	Blank holder force
T_γ	Austenitizing temperature
T_{Heat}	Heating temperature

p_{Air}	Air pressure
Φ	DMD modes
Λ	Diagonal matrix with eigenvalues λ_k
A_1	Area 1
A_2	Area 2
$\Delta \boldsymbol{s}$	Sheet thinning
$\boldsymbol{H}$	Hardness

1. Introduction

The production of increasingly complex structures has been a crucial requirement for the development of new products and a key contributor to the growth of a wide range of industrial sectors in recent decades. Metals, which are still the most widely used class of materials due to their outstanding mechanical properties, have entered new areas of application through a wide variety of manufacturing processes and, thanks to the latest technologies for component design, at competitive cost. Most of the metals are used in the industry with large lot productions, e.g., on average, a car consists of 90% components made by metal forming processes [26]. The focus for high-volume products, such as those in the automotive industry, is therefore on fast and cost-effective production with reproducible high quality, defined by design, surface quality, geometric accuracy, and hardness. These properties should usually also be achieved in a resource- and energy-saving manner [35], as the production of complex sheet metal components is labor- and energy-intensive. The fabrication of sheet parts, which are commonly composed of steel or aluminum, contributes more than 10% of the world's anthropogenic carbon dioxide emissions [18, 34, 21]. The material, which is usually supplied as sheet metal, undergoes a wide variety of forming and machining processes, and are nowadays typically completely automated.

1.1. Content Description and Classification

In order to deal with these requirements, methods from control theory are increasingly implemented in metal forming processes [1, 32]. This work deals with the modeling, estimator and controller development for two different processes, which differ in complexity and objective.

Model-Based Temperature Control for a Deep Drawing Process

The deep drawing process is one of the most important forming processes for shaping flat sheet blanks [14]. In deep drawing, wrinkles and cracks can occur, particularly in complex-shaped areas. To reduce these defects and enhance metal formability, raising the die temperature is a viable approach, as discussed in [73]. For energy-saving production, targeted temperature increases in critical areas are practical. To achieve this, in the project ZF4558805RU8 funded by the German Zentrales Innovationsprogramm Mittelstand (ZIM) an active thermal control using built-in actuators was developed. An experimental device was built with high geometric complexity, serving as a benchmark for other deep drawing tools.

Accurate active thermal control requires a mathematical model describing the spatial-temporal temperature evolution, which is derived based on the heat equation [71]. The finite element (FE) method described in [79] is then applied for spatial discretization due to the complex geometry as in [41, 4]. Based on this model a parameter identification problem is formulated to determine the unknown parameters. Different model order reduction (MOR) techniques (see, e.g., [8, 13]) are applied and compared to obtain a reduced order model (ROM) suitable for the controller and estimator design. For the latter an optimal sensor placement is addressed to improve the temperature estimation capabilities, combining mathematical model and local sensor information. In [9] different model order reduction methods are compared minimizing the covariance matrix in order to find the optimal sensor positions, while in [56] and [44] the balanced model reduction is used. Maximizing the controllability Gramian is the aim of [66] and [13] to find the optimal actuator positions. In this work, the latter approach is transferred to address the sensor placement problem by maximizing the observability Gramian and some related measure as, e.g., proposed by [72]. This directly contributes to the system design as the determined locations are transferred to the experimental setup. This goes along with the incorporation of different model order reduction techniques (see, e.g., the surveys in [3, 8]) and a comparison with the full model. In particular a Kalman filter is implemented based on a ROM to evaluate the performance of the different sensor configurations. This Kalman filter is later tested in an experimental setup to validate sensor placement.

The transition between different temperature profiles in the die can be realized efficiently within a specified time interval making use of a trajectory planning. Flatness based approaches are proposed by, e.g., [13, 2, 50] using, e.g., a Gevrey function [23]. For our purposes a feedback control based on a ROM combined with the implemented Kalman filter is developed. Therefore a linear quadratic (LQ) regulator is used as in [12] for the optimal cooling of steel profiles and in [22] to handle stochastic parameter uncertainties. The regulator is extended by an integral part as proposed in [78] to reduce estimator errors efficiently. For reasons of comparison a proportional derivative (PD) controller is also designed. The quality of the developed control loop is validated experimentally.

Data-Based Control of a Multistage Press Hardening Process

Press hardening of sheet metal in multistage dies enables the production of geometrically complex, hardened components in large batch sizes. Examples include the hot shearing and hardening of automotive belt buckles [53] and transmission parts [54]. Even in singlestage press hardening, the thermal and mechanical interactions and thus the resulting product properties are difficult to predict. In the case of multistage press hardening, the modeling effort to determine a functional process window increases considerably as shown by [19]. Furthermore in case of multistage press hardening, greater uncertainties in the prediction of the product properties are given by a multistage error propagation and an extended perturbation collective. To compensate for the uncertainties and thus to implement a robust and adaptable production, forming processes can be operated in a closed control loop [1]. The implementation of a comprehensive property control in a multistage press hardening, i.e., a multivariable control, is the overall objective of the project 424334660 (Tekkaya/ Meurer) within the Priority Program SPP2183 ”Property-controlled forming processes” by the Deutsche Forschungsgemeinschaft (DFG). Control of product properties requires that the latter are measured and fed back during the running process. This is complicated by the fact that online measurements of properties such as hardness in press hardening are currently only possible to a limited extent in the running process.

To address this, the present work considers the development of a data-driven temperature estimation scheme for the real-time reconstruction of the spatial-temporal temperature distribution in the workpiece. Knowledge of the temperature profile allows to predict the final microstructure, which is a preliminary for the realization of property-controlled multistage press hardening. In this context [38] proposed a temperature estimator design based on the proper orthogonal decompostion (POD) applied to a high-order FE approximation of the process. Differing from this the present work uses a data-driven approach to determine a reduced order mathematical process model [40]. For the actual evaluation the dynamic mode decomposition (DMD) is applied and extended to the present process characteristics using high-dimensional data generated from a detailed process simulation using the FE code `LSDyna`. Applications of DMD are numerous covering, e.g., fluid dynamics [65], power systems [6], and trading strategies [43]. Several extensions to the classical DMD exist involving in particular the DMD with control (DMDc) to handle known and unknown input operators [58]. The input-output DMD additionally takes input and output data into account for the modeling process [10]. In [64] several extensions are discussed to improve robustness and efficiency.

Differing from the summarized applications and techniques the considered multistage press hardening process is characterized by operator-defined process parameters such as stroke rate or blank holder force that can be changed only at certain operating times but not continuously over time. These, however, have to be included into a control concept addressing the evolution of the product properties. To address this a parametric DMD similar to [63, 33] is considered, where the data of different simulations for individual parameter sets are stacked. This resembles the so-called multidomain DMD for a phase-consistent model from multiple overlapping spatial domains [55]. To be able to switch between different process parameters in the resulting reduced order model Lagrangian interpolation is used. The resulting DMD-based model is used to design a state estimator to determine the spatial-temporal temperature distribution in the workpiece. Due to the sensor configuration with different sensor setups in the individual stages a time varying output matrix is introduced to capture the movement and processing of the workpiece(s) through the subsequent stages. As state estimator a Kalman filter is designed. Parameter identifications are performed for actuators and sensors. Here, different measurement instruments (see, e.g., [17]) are used and compared concerning their functionality during the process. In order to improve the robustness of the model a regularization term is added as suggested by [20]. Furthermore, an optimal control problem is formulated which aims to minimize the difference between estimated and target temperature trajectory, in order to reach the desired product properties. The whole developed framework is implemented at an experimental setup to validate its quality.

1.2. General Goals of this Work

Two different metal forming processes, which differ in complexity and objective, are to be discussed throughout this thesis. The first one is a singlestage deep drawing process, where the temperature distribution of the die, which is equipped with thermocouples and actuators, is controlled in combination with an estimation, in order to reduce the occurrence of wrinkles and cracks. The second one is a multistage press hardening process, where the development of the temperature distribution in the blank, which can be influenced with by constant process parameters need to be controlled together with a temperature estimation. Here, the control of product properties using the temperature knowledge is aimed. With these two independent setups different methods are investigated for temperature modeling, estimation and control.

While working on this thesis, the following publications were created with my participation: In [76] and [77] model-based order reductions were evaluated for the temperature distribution in the die during a deep drawing process and an optimal sensor placement for temperature estimation has been performed. This was supplemented by a control design and an experimental validation in [75]. A data-driven temperature estimation approach for a multistage press hardening process is presented in [74]. This was supplemented by the design of a forming and a microstructure soft sensor in [46] and [48]. A paper about the data-based control of this process is in progress. The potential for tailoring the hardness by gradually adapting the thermo-mechanical history throughout this process is discussed in [47]. The paper [45] deals with the quick prediction of thinning in stretch forming of hat shaped profiles during multistage hot sheet metal forming. As part of the Priority Program SPP2183 "Property-controlled forming processes" by the Deutsche Forschungsgemeinschaft (DFG) the collaborative publication [31] provides the scientific definition of a soft sensor based on examples, while [70] thematizes the decoupling of actuators in forming processes.

1.3. Structure

The thesis is structured as follows: Part I introduces a deep drawing process and presents the development and validation of an optimal sensor placement and an estimator-based temperature control. This section consists of Chapters 2 to 6 that provide a comprehensive overview of the deep drawing process. Chapter 2 provides a general description of the deep drawing process, detailing its configuration throughout this section. Chapter 3 introduces the thermal model for the deep drawing tool, its finite element approximation, and the parameter identification process for the actuators. Additionally, various model order reduction (MOR) techniques are briefly discussed. Chapter 4 addresses the optimal sensor placement strategy and the design of an estimator. Chapter 5 delves into the development of an estimator-based controller. Finally, Chapter 6 presents the experimental results validating the entire theoretical framework for the deep drawing process.

In Part II, the thesis explores a multistage press hardening process. This section adopts a data-based modeling approach and incorporates multiple temperature measurement instruments, an estimator design, a control strategy, and experimental validation. Chapter 7 provides an overview of the underlying physical process of the multistage press hardening. In Chapter 8, a data-driven reduced system model is developed using stacking and parametric dynamic mode decomposition (DMD), followed by a parameter identification process for the actuators. Chapter 9 discusses various temperature measurement instruments and introduces the design of a Kalman filter based on the reduced order model. Chapter 10 outlines the control loop, an optimization-based temperature control approach, and property control strategies. Chapter 11 presents the experimental results that validate the entire theoretical framework for the multistage press hardening process.

The last Part III concludes the thesis with a summary in Chapter 12 and an outlook in Chapter 13.

Part I.

Model-Based Temperature Control for a Deep Drawing Process

2. Deep Drawing Process

One of the most important forming processes for shaping flat sheet blanks is the deep drawing process described in [14], where the sheet metal, also known as the blank, is placed on the die and a defined force is applied via a drawing punch. Additionally so-called blank holders are used to ensure an adequate fixation of the sheet metal and to prevent slippage. Deep drawing is instrumental in transforming flat metal sheets into curved components or reducing the diameter of pre-existing curved details. Frequently, a sequence of deep drawing operations is conducted to progressively attain the desired final shape.

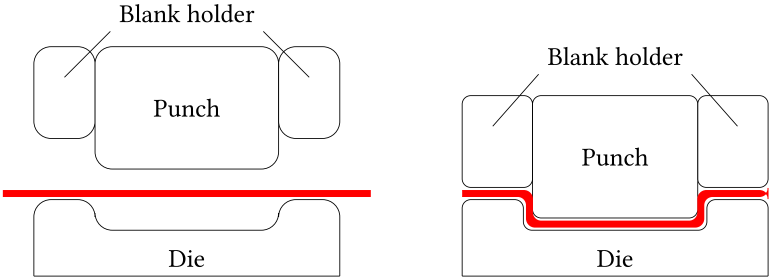

Figure 2.1.: Before (left) and after (right) the deep drawing process. The blank is marked in red.

During the deep drawing process, wrinkles and cracks can be encountered, especially in areas of high geometric complexity. To minimize the possibility of the occurrence of such quality-reducing defects, the temperature of the die can be increased during the process to improve the formability of the metal, as discussed in [73]. For cost-effective and resource-efficient production, it is reasonable to selectively increase the temperature in critical areas. To realize this, a targeted intervention involving built-in actuators is developed, along with the estimation of the spatial-temporal evolution of the temperature within the die. The aim is the development of active thermal control in specialized deep drawing tools. For this purpose, an experimental device, as shown in the computer aided design (CAD) image in Fig. 2.2, is constructed and suitably equipped. It exhibits high geometric complexity to ensure its transferability to other deep drawing tools as a benchmark. In six critical areas, a localized temperature increase is desired. For each of these areas, insertion elements are designed as part of the die and are equipped with actuators. The CAD sketch of the experimental die including these elements is depicted in Fig. 2.3. To obtain information about the temperature distribution within the die, thermocouples are strategically placed in both the insertion elements and the rest of the

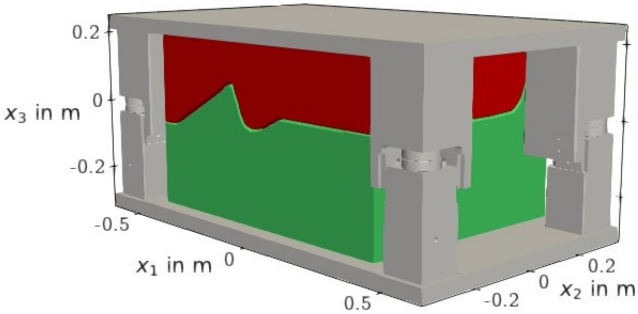

Figure 2.2.: Computer-aided designed experimental deep drawing tool in total. The punch is visualized in red and the die in green.

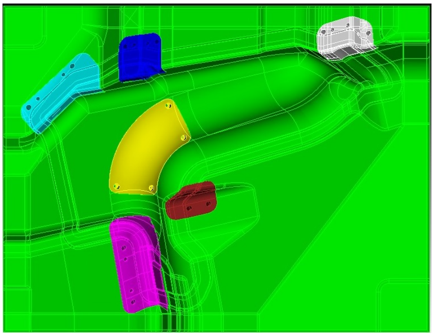

Figure 2.3.: Computer-aided designed experimental die (top view). Insertion element 1 is marked in yellow, 2 in magenta, 3 in light blue, 4 in dark blue, 5 in gray, and 6 in dark red.

die. It is noteworthy that, in this project, a thermal imaging camera was not used due to its requirement for close proximity to the tool. Measuring the temperature during the holding time of the forming process is not possible, and for the open tool, the optical measuring angle is quite limited. This measurement instrument is applied during the multistage press hardening process, as discussed in Part II.

The benefit of a heated die was observed in initial experiments with the experimental device. In Fig. 2.4, two parts of the formed sheet metal (1050 aluminum alloy with a thickness of 0.5 mm) are displayed: one without heating the die (left) and the other with the insertion elements heated open-loop to approximately $T = 150\,^{\circ}\mathrm{C}$ at critical areas (right). The colored ellipsoids mark the positions of the insertion elements with respect to the used colors in Fig. 2.3. Evidently, a reduction in wrinkles is achieved, although the number of cracks remains nearly unchanged. The chosen temperature was determined to be the most effective in reducing defects. One challenge encountered was the temperature decrease in the die due to the cold forming punch. These results unequivocally support the adoption of an actively thermally controlled forming tool to maintain the temperature at a suitably determined level during multiple consecutive forming steps. The development of such a control strategy is described in detail in the Chapters 3 to 6 of this part.

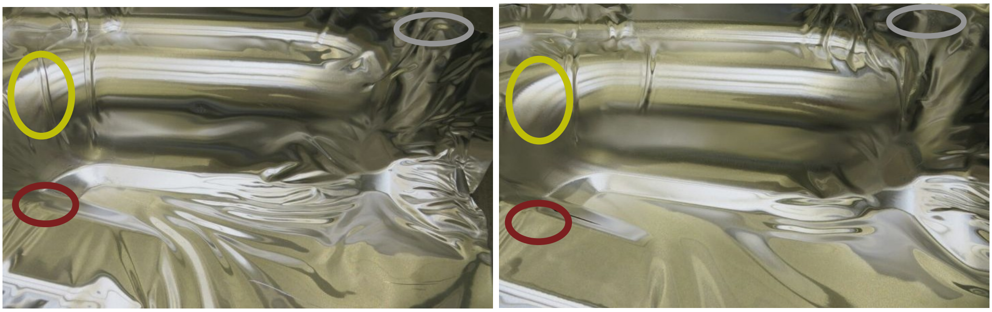

(a) First blank part without heating.

(b) First blank part with heating.

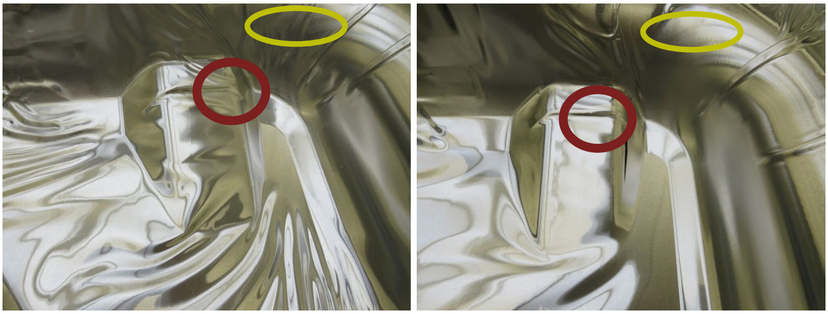

(c) Second blank part without heating.

(d) Second blank part with heating.

Figure 2.4.: Two parts of a shaped blank with and without heating. The colored ellipsoids mark the positions of the insertion elements with respect to the used colors in Fig. 2.3.

3. Modeling, Order Reduction and Parameter Identification

The heat equation is introduced to describe the spatial–temporal temperature evolution in the die. Based on this, a FE approximation is determined resulting in a system of ordinary differential equations. This is reduced using different MOR techniques. A parameter identification based on experimental data is considered to determine the model parameters.

3.1. Continuum Representation

Mathematical modeling of the temperature distribution $T(x,t)$ in the die of the deep drawing tool described in Chapter 2 leads to the heat equation [71]. This partial differential equation (PDE) describing the temperature distribution in a rigid body can be derived by using the first law of thermodynamics. Defining Ω as the spatial domain of this die and $T(x,t)$ as the temperature at point $x = (x_1, x_2, x_3)$ and time $t \geq 0$, the total amount of heat $H(t)$ contained in Ω can be expressed as

$$H(t) = \int_{\Omega} \rho c_p T(x,t)\ d\Omega.$$

Herein, $\rho = 7850\,\mathrm{kg\,m^{-1}}$ and $c_p = 460\,\mathrm{J\,kg^{-1}\,K^{-1}}$ denote the density ρ and specific heat c_p of the material, the tool steel 1.2312 (40CrMnMoS8-6). Note that these parameters may vary with $x = (x_1, x_2, x_3)$ to represent inhomogeneous or composite material. For reasons of simplicity they are chosen to be constant during the considered heating process. This is valid as the specific heat capacity of the steel is constant in the temperature range considered here. The change of heat can be formulated as

$$\partial_t H = \int_{\Omega} \rho c_p \partial_t T(x,t)\ d\Omega.$$

Following Fourier's law heat flows from hot to cold regions with the thermal conductivity $\lambda = 34.5\,\mathrm{J\,s^{-1}\,m^{-1}\,K^{-1}}$ of the material being proportional to the temperature gradient. Heat can enter or leave the domain Ω only through the boundary, which can be described by

$$\partial_t H = \int_{\partial\Omega} \boldsymbol{n} \cdot (\lambda \nabla T)\ d\Gamma.$$

Here, $\partial\Omega$ is the boundary of Ω, $\boldsymbol{n}$ is the outward unit normal vector to $\partial\Omega$ and $d\Gamma$ is the surface measure over $\partial\Omega$. Combining these two approaches, results in

$$\int_\Omega \rho c_p \frac{\partial T(x,t)}{\partial t}\, d\Omega = \int_{\partial\Omega} \boldsymbol{n}\cdot(\lambda\nabla T)\, d\Gamma.$$

Using the divergence theorem for a vector field [71], the right part of the equation can be reformulated, which results in

$$\int_\Omega \rho c_p \partial_t T(x,t)\, d\Omega = \int_\Omega \nabla\cdot(\lambda\nabla T)\, d\Omega.$$

Since the integrals cancel each other out, the derived heat equation for the temperature distribution $T(x,t)$ in the die is

$$\rho c_p \partial_t T - \nabla\cdot(\lambda\nabla T) = 0, \qquad (x,t)\in\Omega\times\mathbb{R}_0^+. \tag{3.1}$$

The model description goes along with the definition of two boundary and an initial condition

$$\boldsymbol{n}\cdot(\lambda\nabla T) = q_i u_i, \qquad (x,t)\in\Gamma_i\times\mathbb{R}_0^+,\ i\in I \tag{3.2a}$$

$$\boldsymbol{n}\cdot(\lambda\nabla T) = h(T_\infty - T), \qquad (x,t)\in\Gamma_a\times\mathbb{R}_0^+ \tag{3.2b}$$

$$T = T_0, \qquad x\in\Omega,\ t=0. \tag{3.2c}$$

The boundary $\partial\Omega$ of the domain Ω is subdivided into $m = 6$ actuated subsets Γ_i, $i\in I = \{1,\dots,m\}$, where the external heating power $q_i u_i$, with maximal power q_i and the degree of actuation $u_i\in[0,1]$ is applied, and the remaining surface Γ_a, which is in contact with the ambient air at uniform temperature T_∞. Convective heat transfer between steel and air is described by the parameter h with SI unit $\mathrm{W\,m^{-2}\,K^{-1}}$. Radiative heat transfer is neglected as its contribution is much smaller compared to convective heat transfer in the experimental temperature range. The surface normal is denoted as $\boldsymbol{n}$. The actuators are not part of the domain Ω.

3.2. Finite Element Approximation

To reduce the complexity of this distributed parameter system for estimator and control design, a discretization approach is performed. Incorporating the intricate geometry of the tool for control, the FE method is applied to (3.1) and (3.2). For this (3.1) is transformed into a weak formulation by multiplication with the test function $v\in V$, with V being a suitable function space for the solution of $\boldsymbol{T}$, and integration over the domain Ω [79]. This leads to

$$\int_\Omega \rho c_p \partial_t T v d\Omega - \int_\Omega \nabla\cdot(\lambda\nabla T) v d\Omega = 0.$$

The second term of this equation is integrated by parts, which results in

$$\int_\Omega \rho c_p \partial_t T v d\Omega + \int_\Omega (\lambda \nabla T) \nabla v \cdot d\Omega - \oint_\Gamma \boldsymbol{n} \cdot (\lambda \nabla T) v d\Gamma = 0.$$

Applying the boundary conditions (3.2a) and (3.2b) yields the weak formulation

$$\int_\Omega \rho c_p \partial_t T v d\Omega + \int_\Omega \lambda \nabla T \cdot \nabla v d\Omega - \int_{\Gamma_i} q_i v d\Gamma_i - \int_{\Gamma_a} h(T_\infty - T) v d\Gamma_a = 0. \tag{3.3}$$

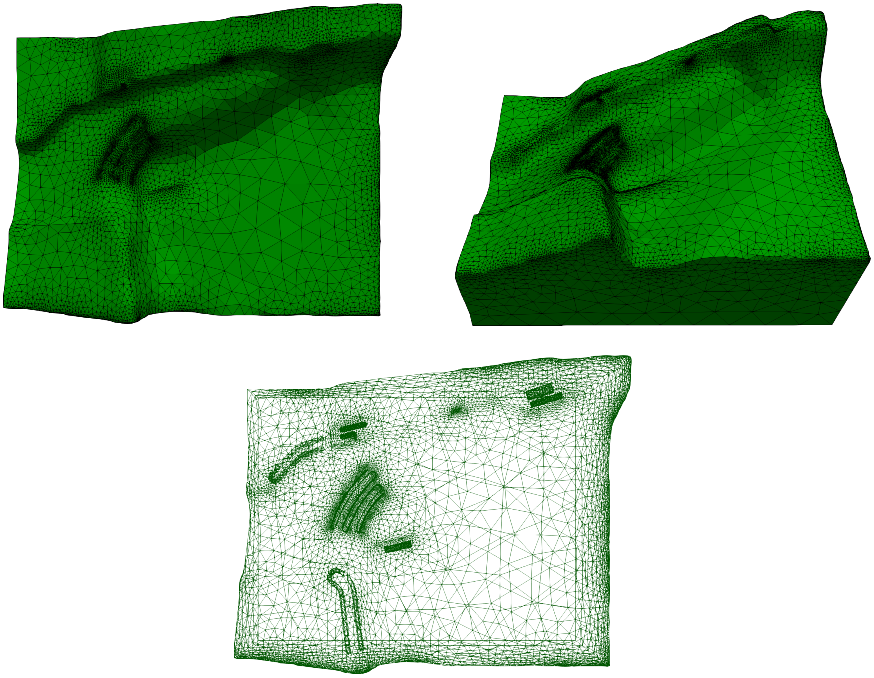

Figure 3.1.: Meshed die, top view (left above) and view of the back side from Fig. 2.2 (right above) and wireframe view (below).

The integral terms in this weak formulation are approximated to obtain a system of ordinary differential equations (ODEs). For this purpose, the entire volume is divided into tetrahedral disjoint finite elements. Based on the CAD construction of the tool shown in Fig. 2.2, the mesh of the die illustrated in Fig. 3.1 was generated using *Coreform Cubit 2020.2*. Critical areas involving curvatures at low radii can be clearly identified due to the comparatively tighter local mesh. The temperature distribution $T^e(x,t)$ in each element is approximated by the trial function

$$T^e(x,t) \approx \bar{T}^e(x,t) = \sum_{a=1}^{k} N_a^e(x)\bar{T}_a^e(t) = N^e(x)\bar{\boldsymbol{T}}^e(t),$$

where N_a^e denotes the local shape functions within the element e, the number of local nodes is denoted by k, and $\bar{T}_a^e$ are the coefficients associated with the respective shape function at each local node a. Local refers to the individual element and global to the whole entity of elements. The shape functions of each element are defined such that $N_a^e(x) = 0$ for $x \notin \Omega_e$ holds true, where Ω_e denotes the domain of an element. It can be concluded that the coefficients $\bar{T}_a^e$ correspond to the node temperatures. The global sum over all E elements

$$T(x,t) \approx \bar{T}(x,t) = \sum_{e=1}^{E} N^e(x)\bar{T}^e(t) = N(x)\bar{\boldsymbol{T}}(t)$$

then gives the approximation of the temperature distribution in the whole domain. The arbitrary test function is approximated by

$$v^e(x) \approx \sum_{b=1}^{k} w_b^e(x)\delta\bar{T}_b^e$$

with the arbitrary constant parameters $\delta\bar{T}_b^e$. The weighting functions w_b^e can be chosen in different ways. In this work the Galerkin-method is used, where the weighting functions are chosen equal to the initial functions, i.e. $w_b^e = N_b^e$. This often leads to symmetric matrices [79]. Thus the global test function as a sum over elements results in

$$v^e(x) \approx \sum_{e=1}^{E} N^{e^T}(x)\delta\bar{\boldsymbol{T}}^e = N^T(x)\delta\bar{\boldsymbol{T}}.$$

Using these test functions for the weak formulation (3.3) yields

$$\begin{aligned} \delta\bar{\boldsymbol{T}}\left[\left(\int_\Omega \rho c_p N N^T d\Omega\right)\partial_t\bar{\boldsymbol{T}}\right] &= \delta\bar{\boldsymbol{T}}\left[\left(\int_\Omega \lambda\nabla N\cdot\nabla N^T d\Omega + \int_{\Gamma_a} hNN^T d\Gamma_a\right)\bar{\boldsymbol{T}}\right] \\ &\quad + \delta\bar{\boldsymbol{T}}\left[\int_{\Gamma_a} hT_\infty N^T d\Gamma_a + \int_{\Gamma_i} q_i N^T d\Gamma_i\right]. \end{aligned}$$

The FE approximation (3.3) is evaluated using the software library *Firedrake* [60] in Python and leads to the finite-dimensional approximation in terms of the system of ODEs

$$E\dot{\boldsymbol{T}} = A\boldsymbol{T} + B\boldsymbol{u}, \quad t > 0, \quad \boldsymbol{T}(0) = \boldsymbol{T}^0. \tag{3.4}$$

Here, the nodal temperatures are summarized in the vector $\boldsymbol{T}(t) \in \mathbb{R}^n$ with $n = 42819$, the thermal damping matrix is

$$E = \int_\Omega \rho c_p N N^T d\Omega = \sum_{e=1}^{E} E^e \in \mathbb{R}^{n\times n},$$

and the thermal stiffness matrix

$$A = -\int_\Omega k\nabla N \cdot \nabla N^T d\Omega - \int_{\Gamma_a} h N N^T d\Gamma_a = \sum_{e=1}^{E} A^e \in \mathbb{R}^{n\times n}.$$

Here, the spectrum of A is contained in the open left half plane, i.e., $\sigma(A) \subset \mathbb{C}_0^-$. The ambient temperature T_∞ is assumed constant, so the mapping $T(x,t) \mapsto T(x,t) - T_\infty$ or respectively

$$\boldsymbol{T}(t) \mapsto \boldsymbol{T}(t) - T_\infty \mathbf{1} \tag{3.5}$$

with $\mathbf{1} \in \mathbb{R}^n$ composed of only ones is introduced for the subsequent analysis and design. The input vectors follow from

$$\boldsymbol{b}_i = \int_{\Gamma_i} q_i N^T d\Gamma_i = \sum_{e=1}^{E} \boldsymbol{b}_i^e,$$

and imply the input matrix $B = [\boldsymbol{b}_1, \boldsymbol{b}_2, \ldots, \boldsymbol{b}_m] \in \mathbb{R}^{n\times m}$ for domain Ω. The individual matrices for the elements result with the respective trial and test functions to

$$\begin{aligned} E^e_{ba} &= \int_\Omega \rho c_p N_a N_b d\Omega, \\ A^e_{ba} &= -\int_\Omega k\nabla N_a \cdot \nabla N_b d\Omega - \int_{\Gamma_a} h N_a N_b d\Gamma_a, \\ \boldsymbol{b}^e_{i,ba} &= \int_{\Gamma_i} q_i N_b d\Gamma_i. \end{aligned}$$

The input vector reads $\boldsymbol{u}(t) = [u_1(t), u_2(t), \ldots, u_m(t)]^T$ with $u_i(t) \in [0,1],\ i = 1, \ldots, m$ entering the system via the input vectors $\boldsymbol{b}_i$. This represents the heating elements with maximal power q_i for $u_i = 1$ defined in (3.2a).

The output matrix $C \in \mathbb{R}^{p\times n}$ extracts the local temperatures at to be determined measurement locations inside and on the die, i.e.,

$$\boldsymbol{y} = C\boldsymbol{T}, \quad t \geq 0 \tag{3.6}$$

with $\boldsymbol{y}(t) \in \mathbb{R}^p$. In particular, p sensors are placed using the optimization setup addressed in Chapter 4.

3.3. Model Order Reduction

The large number of $n = 42819$ nodes leads to a computationally intensive calculation for simulation, one time step takes 1.2462 s, and makes the model unusable for estimator and control design purposes, which are discussed in Chapter 4 and 5. To cope with this difficulty a reduced order model (ROM) of significantly lower dimension $r \ll n$ is determined, which approximates the dynamics of the full order system with sufficient accuracy. Due to the model availability in terms of (3.4) and (3.6) projection-based MOR is considered. Following [8] the unknown state variables in a basis of reduced dimension are approximated and the governing equations are projected onto a suitably defined subspace of small dimension. The projection matrices $V \in \mathbb{R}^{n\times r}$ and $W \in \mathbb{R}^{n\times r}$ are used, where $\mathcal{V} = \text{range}(V)$ is an r-dimensional test subspace and $\mathcal{W} = \text{range}(W)$ an associated trial subspace. Approximating the full state $\boldsymbol{T}(t)$ evolving in the r-dimensional subspace $\mathcal{V}$ in terms of $\boldsymbol{T}_r(t) \in \mathbb{R}^r$,

$$\boldsymbol{T} \approx V\boldsymbol{T}_r, \tag{3.7}$$

is written. Taking into account the Petrov-Galerkin condition [8]

$$W^T\left(EV\dot{\boldsymbol{T}}_r - AV\boldsymbol{T}_r - B\boldsymbol{u}\right) = 0,$$

the substitution of (3.7) into (3.4), (3.6) yields

$$E_r\dot{\boldsymbol{T}}_r = A_r\boldsymbol{T}_r + B_r\boldsymbol{u}, \quad t > 0, \quad \boldsymbol{T}_r(0) = \boldsymbol{T}_r^0 \tag{3.8a}$$

$$\boldsymbol{y} = C_r\boldsymbol{T}_r. \tag{3.8b}$$

Herein, the reduced order matrices $E_r \in \mathbb{R}^{r\times r}$, $A_r \in \mathbb{R}^{r\times r}$, $B_r \in \mathbb{R}^{r\times m}$ and $C_r \in \mathbb{R}^{p\times r}$ are determined as

$$E_r = W^TEV,\ A_r = W^TAV,\ B_r = W^TB,\ C_r = CV. \tag{3.9}$$

The calculation time of one time step reduces significantly to 0.0147 s for an exemplary reduction order $r = 95$. Subsequently, three different MOR techniques based on this projection are evaluated, namely the balanced truncation (BT), the iterative rational Krylov algorithm (IRKA) and the proper orthogonal decomposition (POD). Note that the POD only makes use of one-sided projections with $V = W$.

3.3.1. Balanced Truncation

The controllability and observability Gramians depend on the respective choice of the coordinate system and will transform under a change of coordinates. A transformation with respect to the controllability and observability is called balanced, if the gramians W_c and W_o reduce to $W_{c,r} = W_{o,r}$ becoming equal and diagonal [15].

Given (3.4), (3.6) and the fact that the spectrum of A is contained in the open left half plane, i.e., $\sigma(A) \subset \mathbb{C}_0^-$, the controllability and observability Gramians W_c and W_o can be calculated via the generalized Lyapunov equations

$$AW_cE^T + EW_cA^T + BB^T = 0, \tag{3.10a}$$

$$A^TW_oE + E^TW_oA + C^TC = 0. \tag{3.10b}$$

To solve these efficiently the low-rank alternating-direction implicit (ADI) method presented in, e.g., [11, 57] is applied. Using the Cholesky decompositions $W_c = W_{c,C}W_{c,C}^T$, $W_o = W_{o,C}W_{o,C}^T$ and the singular value decomposition (SVD)

$$W_{c,C}^T W_{o,C} = \begin{bmatrix} U_1 & U_2 \end{bmatrix} \begin{bmatrix} \Sigma_1 & 0 \\ 0 & \Sigma_2 \end{bmatrix} \begin{bmatrix} V_1^T \\ V_2^T \end{bmatrix}$$

leads to the balancing transformations [49]

$$W = W_{o,C}V_1\Sigma_1^{-\frac{1}{2}}, \quad V = W_{c,C}U_1\Sigma_1^{-\frac{1}{2}}.$$

For BT these matrices are used to evaluate (3.8). Herein, the MESS toolbox [52] in MATLAB is used for numerical evaluation.

3.3.2. Iterative Rational Krylov Algorithm

Moment matching (MM) methods in general aim at the construction of a lower degree rational transfer function $G_r(s) = C_r\,(sE_r - A_r)^{-1}\,B_r$ that interpolates the transfer function $G(s) = C\,(sE - A)^{-1}\,B$ of the full order system and its derivatives at certain points $\sigma_i \in \mathbb{C}$ in the complex domain. The iterative rational Krylov algorithm (IRKA) is a MM method using an $\mathcal{H}_2$-optimal shift set to determine W and V iteratively [27, 7, 62]. The interpolation between the transfer functions only takes place along certain directions, which is called tangential interpolation. This leads to

$$G(\sigma_i)\boldsymbol{r}_i = G_r(\sigma_i)\boldsymbol{r}_i, \quad \boldsymbol{l}_i^T G(\sigma_i) = \boldsymbol{l}_i^T G_r(\sigma_i), \qquad \text{for } i = 1, \dots, r,$$

where $G_r(s)$ is a right-tangential interpolant to $G(s)$ at the interpolation points $s = \sigma_i$ along the right tangent direction $\boldsymbol{r}_i \in \mathbb{C}^m$ and it is a left-tangential interpolant at these points along the left tangent direction $\boldsymbol{l}_i \in \mathbb{C}^p$. The pole-residue expansion of the reduced order model transfer function is defined as

$$G_r(s) = C_r\,(sE_r - A_r)^{-1}\,B_r = \sum_{i=1}^{r} \frac{\boldsymbol{l}_i\boldsymbol{r}_i^T}{s - \lambda_i},$$

where the poles λ_i are distinct. The left and right tangent directions $\boldsymbol{l}_i$ and $\boldsymbol{r}_i$ are associated with the pole λ_i of $G_r(s)$. The matrix $\boldsymbol{l}_i\boldsymbol{r}_i^T$ is the residue of $G_r(s)$ at $s = \lambda_i$.

The algorithm starts with initial interpolation points $\{\sigma_1, \dots, \sigma_r\}$ and tangent directions $\boldsymbol{r}_1, \dots, \boldsymbol{r}_r$ and $\boldsymbol{l}_1, \dots, \boldsymbol{l}_r$. Thereafter the transformation matrices V and W are calculated in a $\mathcal{H}_2$-optimal way (see Appendix A)

$$V = \begin{bmatrix} (\sigma_1 E - A)^{-1} B \boldsymbol{r}_1 & \dots & (\sigma_r E - A)^{-1} B \boldsymbol{r}_r \end{bmatrix}, \tag{3.11a}$$

$$W = \begin{bmatrix} (\sigma_1 E - A^T)^{-1} C^T \boldsymbol{l}_1 & \dots & (\sigma_r E - A^T)^{-1} C^T \boldsymbol{l}_r \end{bmatrix}. \tag{3.11b}$$

Here, an iterative procedure begins and runs until the relative change in $\{\sigma_i\} < r_{\text{tol}}$ occurs:

1. The reduced order system matrices E_r, A_r, B_r and C_r are computed using (3.9).
2. A pole-residue expansion of $G_r(s)$ is formulated

$$G_r(s) = C_r \left(sE_r - A_r\right)^{-1} B_r = \sum_{i=1}^{r} \frac{\hat{\boldsymbol{l}}_i \hat{\boldsymbol{r}}_i^T}{s - \lambda_i}.$$

3. The interpolation points and the tangential directions are set to new values

$$\sigma_i \longleftarrow -\lambda_i, \quad \boldsymbol{r}_i \longleftarrow \hat{\boldsymbol{r}}_i, \quad \boldsymbol{l}_i \longleftarrow \hat{\boldsymbol{l}}_i.$$

4. The transformation matrices V and W are calculated using (3.11a) and (3.11b).

Finally the reduced system is set up using (3.9). For the considered application the IRKA is solved using the sssMOR toolbox [16] in MATLAB.

3.3.3. Proper Orthogonal Decomposition

In contrast to BT, POD relies on simulations of the system and is independent of the input/output behavior. The selection of POD basis vectors or POD modes is an empirical process accomplished through the method of snapshots [69]. Let $\boldsymbol{T}(t)$ represent the solution to equations (3.4) and (3.6) at time t, given an initial state $\boldsymbol{T}^0$ and process input $\boldsymbol{u}$. To construct the snapshot matrix X, which captures the m state solutions, they are arranged as follows:

$$X = \begin{bmatrix} \boldsymbol{T}(t_0) & \boldsymbol{T}(t_1) & \dots & \boldsymbol{T}(t_{m-1}) \end{bmatrix} \in \mathbb{R}^{n \times m}.$$

The POD modes are created by performing a SVD on the snapshot matrix, approximating it as $X \approx U_r S_r V_r^*$. Here, $U_r \in \mathbb{C}^{n \times r}$ and $V_r \in \mathbb{C}^{m \times r}$ are the left and right singular vectors, respectively, and $S_r \in \mathbb{C}^{r \times r}$ is a diagonal matrix containing the singular values, with $\cdot^*$ indicating the complex conjugate transpose. The projection matrix V is composed of the leading first r column vectors U_j of U corresponding to the r largest singular values:

$$V = \begin{bmatrix} U_1 & U_2 & \dots & U_r \end{bmatrix}.$$

Given the size of the snapshot matrix X, a truncated SVD is often performed. The singular values can guide the determination of the number of basis vectors needed to achieve a sufficiently accurate snapshot reconstruction. To do this, a threshold H is considered:

$$H = \frac{\sum_{i=1}^{r} \sigma_i}{\sum_{i=1}^{n} \sigma_i} < \epsilon,$$

where ϵ is a specified tolerance, and H is often referred to as the energy of the snapshots captured by the POD modes. Using Galerkin-projection [8], the reduced system can be expressed as (3.8). The matrices E_r, A_r, B_r, and C_r are computed using (3.9) [39]. The states $\boldsymbol{T}$ of the full system can be recovered from $\boldsymbol{T}_r$ using (3.7). It is important to note that the POD method is optimal in the sense that it minimizes the least square error of the snapshot reconstruction but does not guarantee optimal reconstruction of the full model [61]. Therefore, selecting appropriate excitation signals $\boldsymbol{u}$ is crucial to account for any relevant system dynamics.

3.3.4. Comparison of MOR Techniques

In order to validate the presented MOR techniques, all three ROMs are simulated in an exemplary scenario with $\boldsymbol{u}(t) = [0.5, 0.5, 0.5, 0.5, 0.5, 0.5]^T$ for a duration of 5 min. After simulation the full order states are reconstructed via (3.7). Fig. 3.2 depicts the mean temperature development over all $n = 42819$ nodes from these reconstructions $\text{mean}(\boldsymbol{T})$. The difference between reconstructed and original full order model $\Delta\boldsymbol{T}$ is calculated. Its maximum value at certain time points $\max(\Delta\boldsymbol{T})$ is visualized by a gray error bar and its mean value over all nodes $\text{mean}(\Delta\boldsymbol{T}) = \sum_{i=1}^{n} \Delta T_i / n$ by a red error bar. For all three different MOR techniques the error is quite small. The mean error $\text{mean}(\Delta\boldsymbol{T})$ is below 1 °C at all time points for all MOR algorithms. The same can be said for the maximum error $\text{mean}(\Delta\boldsymbol{T})$ for BT and POD. For IRKA it sometimes is slightly above 1 °C. As a consequence all three techniques are valid approaches for model reduction.

3.4. Parameter Identification

Heating elements are installed in order to locally increase the temperature in the die. These are placed in the $m = 6$ insertion elements $I = \{1, \dots, 6\}$ which are fully integrated in the die and consist of the same tool steel 1.2312 (40CrMnMoS8-6). The dimensions of the heaters, their maximum heating power and the type are listed in Table 3.1. Elements $i \in \{1, 2, 3, 6\}$ are equipped with one heater, elements $i \in \{4, 5\}$ with two heaters controlled in parallel. A sensor is installed in each of the elements.

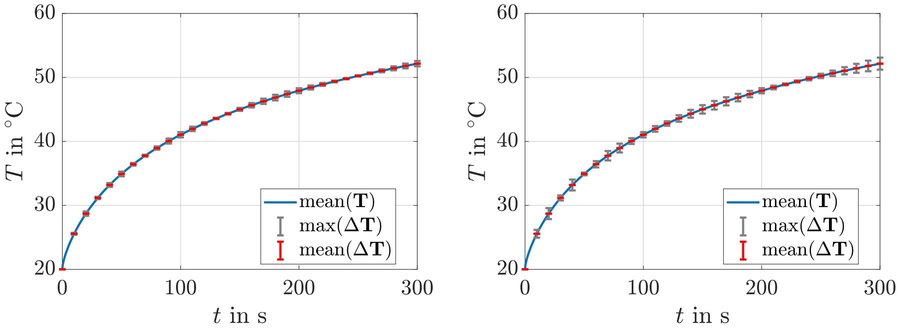

(a) BT reduced model. (b) IRKA reduced model.

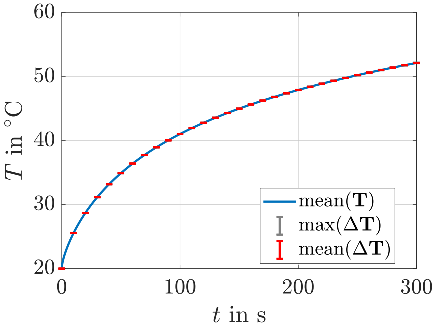

(c) POD reduced model.

Figure 3.2.: Mean temperature developments mean$(\boldsymbol{T})$ and reduction errors $\Delta\boldsymbol{T}$ for simulation of a test scenario for all three MOR techniques.

El. $i \in I$	Measures in mm	Power in W	Heater type
1	Ø4 × 930	1200	Coil
2	Ø8.5 × 468	1050	Tubular
3	Ø8.5 × 397	900	Tubular
4	Ø12.5 × 65	500	Cartridge
	Ø12.5 × 35	300	Cartridge
5	Ø20 × 50	600	Cartridge
	Ø12.5 × 70	550	Cartridge
6	Ø16 × 60	400	Cartridge

Table 3.1.: Properties of the heating elements in the six insertion elements.

Due to non-ideal assembly and imperfections in installation the transferred and experimentally observed heating power does not directly correspond to the nominal values listed in Table 3.1.

To address this and to cover the accumulated effects of the assembly and installation a parameter identification procedure is developed.

Together with the parameters of the actuators, the heat transfer coefficient of (3.2b) is adressed in this identification setup, as it is not exactly defined by the used material and therefore not known. For parameter identification, the insertion elements are considered as separate components detached from the die. They are fully surrounded by the ambient air at uniform temperature T_∞. A mathematical model for describing the temperature distribution over the respective domains is derived for all six insertion elements. The continuum representations are derived in the same way as in (3.1). To discretize the equations again the FE method is used. The meshes generated using *Coreform Cubit 2020.2* are illustrated in Fig. 3.3. As before the FE model is determined using the software library *Firedrake* [60] to obtain the set of ODEs

$$E_i \dot{\boldsymbol{T}}_i = A_i \boldsymbol{T}_i + B_i \boldsymbol{u}_i, \qquad t > 0, \quad \boldsymbol{T}_i(0) = \boldsymbol{T}_i^0, \tag{3.12a}$$

$$y_i = \boldsymbol{c}_i^T \boldsymbol{T}_i, \qquad t \geq 0. \tag{3.12b}$$

with

$$\begin{aligned} A_i &= A_{\lambda,i} + h A_{h,i}, \\ \boldsymbol{u}_i(t) &= p\eta_i \left(1 - e^{-\frac{t}{\tau_i}}\right) \begin{cases} 1, & i \in \{1,2,3,6\}. \\ \begin{bmatrix} 1 \\ 1 \end{bmatrix}, & i \in \{4,5\}. \end{cases} \end{aligned} \tag{3.12c}$$

The nodal temperatures are summarized in the vectors $\boldsymbol{T}_i(t) \in \mathbb{R}^{n_i}$ for n_i, $i = 1, \ldots, m$. The elements of the thermal damping matrices $E_i \in \mathbb{R}^{n_i \times n_i}$, the input matrices $B_i \in \mathbb{R}^{n_i \times 1}$ for $i \in \{1,2,3,6\}$ and $B_i \in \mathbb{R}^{n_i \times 2}$ for $i \in \{4,5\}$ and the thermal stiffness matrices $A_i \in \mathbb{R}^{n_i \times n_i}$ are obtained from the variational form of the continuum representation. Herein, $A_{\lambda,i}$ denotes the part of A_i resulting from (3.1) of the heat equation and $A_{h,i}$ the part from (3.2b). This splitting enables the parameter identification of the heat transfer coefficient h. The output vectors $\boldsymbol{c}_i^T \in \mathbb{R}^{1 \times n_i}$ are used to project the nodal temperature to the measured outputs y_i. In the equations p is the degree of actuation and η_i can be interpreted as efficiency factors. The variables τ_i describe the delayed start-up of the actuators following a PT_1 behavior. The measured sensor values $\tilde{y}_i$ are collected for all six insertion elements in two different scenarios resulting in two data sets $\{\tilde{y}_{p_1,i}\}_{i=1}^6$ and $\{\tilde{y}_{p_2,i}\}_{i=1}^6$. These differ in the used degree of actuation with

$$p_1 = \begin{cases} 0.1, & t \leq t_{1,i} \\ 0, & t > t_{1,i}. \end{cases}, \quad p_2 = \begin{cases} 1, & t \leq t_{2,i} \\ 0, & t > t_{2,i} \end{cases},$$

where $t_{1,i}$ and $t_{2,i}$ denote the points in time at which the degrees of actuation become zero to avoid extremely high temperatures. During the experiments, the insertion elements were detached from the die. Making use of (3.12a) numerical solutions are determined for each insertion element for both actuation scenarios in each iteration of the optimization problem

$$\min_{h,\boldsymbol{\eta},\boldsymbol{\tau}} J = \sum_{i=1}^{m} \left\| \tilde{y}_{p_1,i} - y_{p_1,i} \right\|_1 + \sum_{i=1}^{m} \left\| \tilde{y}_{p_2,i} - y_{p_2,i} \right\|_1,$$

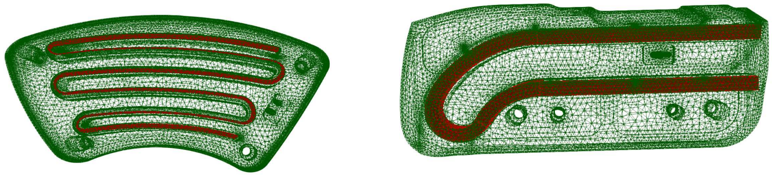

(a) Meshed insertion element 1 with an red marked coil heater.

(b) Meshed insertion element 2 with an red marked tubular heater.

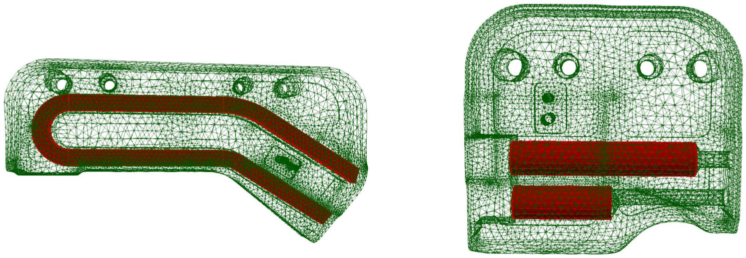

(c) Meshed insertion element 3 with an red marked tubular heater.

(d) Meshed insertion element 4 with two red marked cartridge heaters.

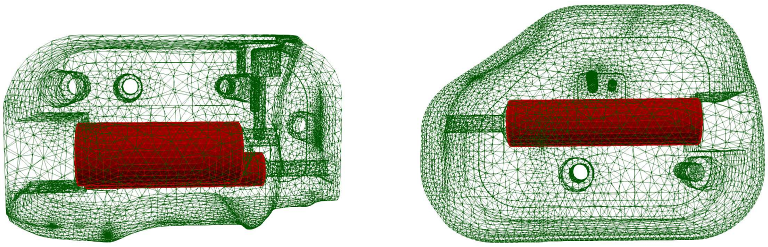

(e) Meshed insertion element 5 with two red marked cartridge heaters.

(f) Meshed insertion element 6 with an red marked cartridge heater.

Figure 3.3.: Meshes of the six insertion elements.

where $y_{p_1,i}$ and $y_{p_2,i}$ refer to the simulated outputs, h is the to be determined heat transfer coefficient, and $\boldsymbol{\eta} = [\eta_1, \ldots, \eta_6]^T$, $\boldsymbol{\tau} = [\tau_1, \ldots, \tau_6]^T$ are the parameters in (3.12c). The optimization problem results in $h = 6.6768$ and the values in Table 3.2. The optimization objective $J = 2321.5\,\mathrm{K}$, which is equivalent to a temperature difference of $T_{\mathrm{diff}} = 2321.5\,\mathrm{K}/n_{\Delta t} \approx 0.9625\,\mathrm{K}$ between optimized simulation and experimental data, is sufficiently small. Here, the total number of time steps in all data sets is $n_{\Delta t} = 2412$. Literature values for the heat transfer coefficient h between

No. i	η_i	τ_i
1	0.9409	40.4569
2	0.8738	16.7488
3	0.8824	27.0662
4	0.9561	9.9137
5	0.7836	9.9217
6	0.9063	31.5385

Table 3.2.: Opimized values of the heating elements.

steel and air are in the range of $h = 5\,\mathrm{W\,m^{-2}\,K^{-1}}$ and $h = 30\,\mathrm{W\,m^{-2}\,K^{-1}}$ [36], which fit with the determined value. The results for the efficiency factors $\boldsymbol{\eta}$ are also plausible. As expected, they are smaller than, but close to 1 and state that the actuators have maximum heating powers of 78.36 % to 95.61 % of the data sheet values. The optimized values of the delay variables $\boldsymbol{\tau}$ result in transient responses between 9.9137 s and 40.4569 s, with the maximum value for the coil heater.

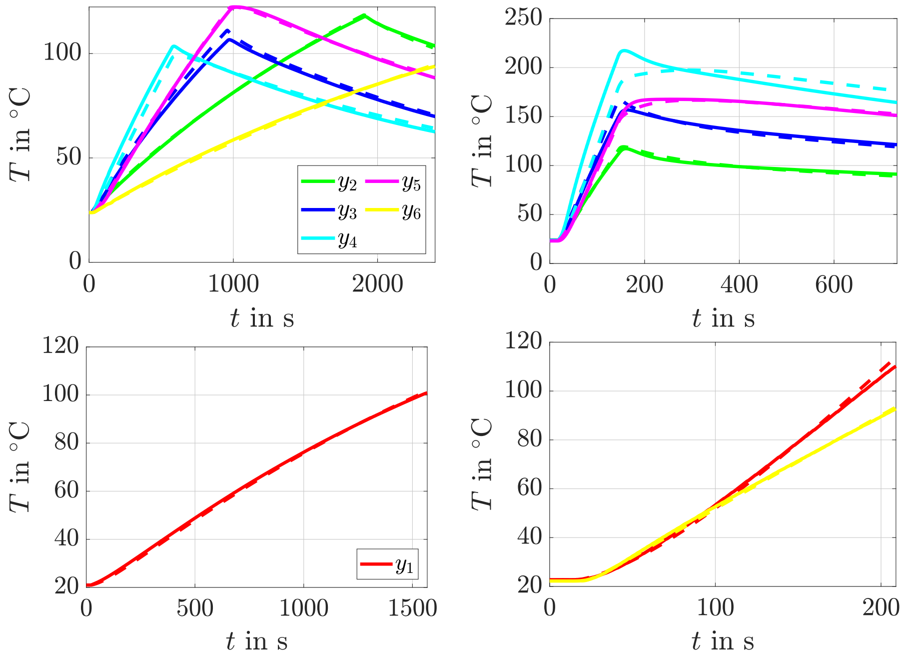

Figure 3.4.: Simulations (continuous lines) and experimental data (dashed lines) of the six insertion elements in the scenarios with $p = p_1$ (left) and $p = p_2$ (right).

Fig. 3.4 depicts the temporal evolution of the temperature in the two scenarios. The dashed lines represent the experimental data, while the continuous lines refer to the simulations results using (3.12a) with the determined parameters. The results clearly confirm that the dynamics of the insertion elements is rather accurately represented. Differences arise primarily for the fourth insertion element in the scenario p_2, where temperatures above 200 °C are induced. These may lead to simulation problems as the influence of the neglected effect of radiative heat transfer becomes more important. Finally, the identified actuator dynamics and heat transfer coefficient h supplement the mathematical model of the spatial–temporal temperature evolution in the die (3.4).

4. Optimal Sensor Placement

To determine the most reasonable sensor positions in the die, to gain insight into the process dynamics and to set up an estimator strategy an optimization-based approach is considered to place sensors. As the insertion elements are equipped with separate sensors a model of the die without these elements is used for optimization. This model is described in detail in [76]. The mesh is visualized in Fig. 4.1.

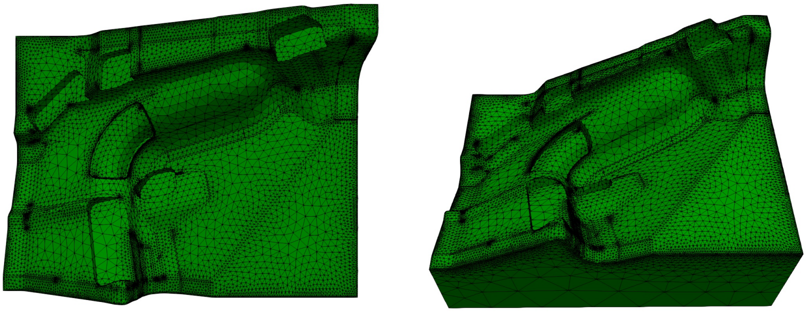

Figure 4.1.: Meshed die, top view (left) and view of the back side from Fig. 2.2 (right).

4.1. Segmentation

For sensor placement the model geometry is divided into segments illustrated in Fig. 4.2. Segments in this context represent possible sensor positions used as decision variables in the optimal sensor placement problem introduced subsequently. The segments are created by dividing the x_1-, x_2- and x_3-axes into 8, 7 and 4 elements, respectively. Since the surface in x_3-direction varies in height in total $p = 166$ segments are considered with some not fully occupied by the tool volume.

The output equation for the segmentation is defined as

$$\boldsymbol{y}_{\text{seg}} = C_{\text{seg}} \boldsymbol{T}, \quad t \geq 0 \tag{4.1}$$

amending the finite-dimensional approximation (3.4). The vector $\boldsymbol{y}_{\text{seg}}(t) \in \mathbb{R}^p$ is composed of the temperatures averaged over each possible segment. Therefore the nonzero elements of the

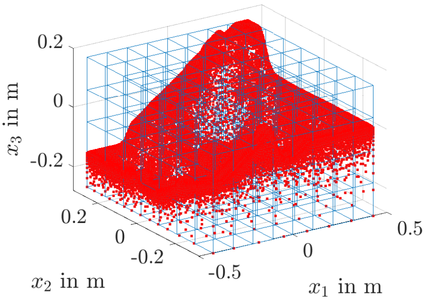

Figure 4.2.: Nodes (red dots) and segments (cuboids) of the die.

sparse output matrix $C_{\text{seg}} \in \mathbb{R}^{p \times n}$ are defined as q^{-1}, with q being the number of nodes in the specific segment.

4.2. Optimization Problem

To quantify the level of observability of a particular sensor configuration the observability Gramian W_o is used, which contains the observable subspace of a system [15]. This matrix describes to which extent the system dynamics can be reconstructed by the placed sensors. The observability Gramian W_o can be computed by means of the generalized Lyapunov equation (3.10b) using C_{seg} as output matrix. The Gramian W_o depends on C_{seg} and thus on the placed sensors. Hence, $W_o(\chi)$ with the binary vector $\chi \in \{0,1\}^p$ is used representing a possible sensor configuration and $\chi_i = 1$ denoting a chosen segment. This method enables the possibility to define non-feasible segments.

4.2.1. MAX-DET Optimization

By making use of the results of [66] for the dual problem of optimal actuator placement the maximization of the determinant of W_o is considered as the maximum represents the volume of the observable subspace. This leads to

$$\max_{\chi} \det \left(W_o\left(\chi\right)\right).$$

The observability Gramian $W_{o,i}$ is set up for each segment so that due to linearity

$$W_o\left(\chi\right) = \sum_{i=1}^{p} \chi_i W_{o,i}$$

with the decision variables $\chi_i \in \{0, 1\}$, $i = 1, \dots, p$. To accelerate the calculation, an SVD is performed, i.e., $W_o = USV^T$, and only the s largest singular values $U_{1:s}$ are considered in the reduced Gramian $W_{o,red} = U_{1:s} W_o U_{1:s}^T$, where the first s columns of U are used to reduce the size of W_o from $\mathbb{R}^{n \times n}$ to $\mathbb{R}^{s \times s}$. This extracts the most relevant information contained in the s largest singular values and yields the reduced optimization problem

$$\max_{\chi} \det \left(\sum_{i=1}^{p} \chi_i U_{1:s} W_{o,i} U_{1:s}^T \right).$$

The maximization problem can be recast into a minimization problem by considering the inverse matrix and making use of the logarithm for better scaling. This results in the mixed-integer optimization problem

$$\min_{\chi} \log \det \left(\sum_{i=1}^{p} \chi_i U_{1:s} W_{o,i} U_{1:s}^T \right)^{-1} \tag{4.2a}$$

$$\text{s.t.} \quad \sum_{i=1}^{p} \chi_i \leq p_{\max}, \quad \chi_i \in \{0, 1\}, \tag{4.2b}$$

where $p_{\max}$ is the maximal number of sensors to be embedded into the die.

4.2.2. Alternative Measures

Following, e.g., [72] measures other than the MAX-DET optimization seem reasonable. This includes $\max(-\operatorname{trace} W_o^{-1})$, which is proportional to the energy needed on average to observe the systems' states. Taking into account the previous exposition the resulting minimization problem reads

$$\min_{\chi} \operatorname{trace} \left(\sum_{i=1}^{p} \chi_i U_{1:s} W_{o,i} U_{1:s}^T \right)^{-1} \quad \text{s.t. (4.2b).} \tag{4.3}$$

The measure max trace W_o is inversely related to the average energy of the system and calculates the average observability in all directions. This implies

$$\min_{\chi} -\operatorname{trace} \left(\sum_{i=1}^{p} \chi_i U_{1:s} W_{o,i} U_{1:s}^T \right) \quad \text{s.t. (4.2b).} \tag{4.4}$$

To maximize the dimension of the observable subspace the rank of the Gramian can be maximized so that

$$\min_{\chi} -\operatorname{rank} \left(\sum_{i=1}^{p} \chi_i U_{1:s} W_{o,i} U_{1:s}^T \right) \quad \text{s.t. (4.2b).} \tag{4.5}$$

It might also be useful to maximize the smallest eigenvalue $\lambda_{\min}(W_o)$ of the observability Gramian. This measures the amount of energy, which is needed to move the system into the direction that is most difficult to observe and implies

$$\min_{\chi} -\lambda_{\min}\left(\sum_{i=1}^{p} \chi_i U_{1:s} W_{o,i} U_{1:s}^T\right) \quad \text{s.t. (4.2b).} \tag{4.6}$$

4.2.3. Optimization using ROMs

Solving the Lyapunov equation to obtain the observability Gramian W_o requires high computational power. Another intuitive way to calculate a reduced Gramian is solving the Lyapunov equation (3.10b) for the ROM (3.8). This allows to transfer any of the optimization problems (4.2) to (4.6) by replacing W_o with the resulting ROM-based Gramian $W_{o,r}$. Since the sensor-dependent output matrix C is not available, C_{seg} is used to create the ROM. Aiming, e.g., at the maximization of the smallest eigenvalue as in (4.6) this results in

$$\min_{\chi} -\lambda_{\min}\left(\sum_{i=1}^{p} \chi_i U_{1:s} W_{o,r,i} U_{1:s}^T\right) \quad \text{s.t. (4.2b).} \tag{4.7}$$

Subsequently, the distinction is made between the reduced observability Gramian $W_{o,r}$ computed using BT ($W_{o,\text{BT}}$), IRKA ($W_{o,\text{IRKA}}$), and POD ($W_{o,\text{POD}}$).

4.3. Optimal Sensor Configuration

Depending on the different measures (4.2) to (4.7) and observability Gramians the respective optimal sensor configurations are determined. For the numerical evaluations $s = 10$ is chosen so that the 10 largest singular values of the observability Gramian $W_{o,i}$ are used to represent the most relevant part of the dynamics.

4.3.1. Comparison of Measures

The first optimizations are set up with the full model and $p_{\max} = 8$. The optimality measure is varied to compare (4.2) to (4.6). For the solution of the mixed-integer optimization problems the Genetic Algorithm from the Global Optimization Toolbox of MATLAB is used as it can solve smooth and nonsmooth optimization problems including integer constraints. Here, different from the default settings, the function tolerance is reduced to 1×10^{-20}, the constraint tolerance to 1×10^{-6} and the maximal stall generations are increased to 50 000, in order to reduce the probability of reaching only local minimums. Fig. 4.3 shows the resulting sensor placement in the die, where the nodes inside the respective segments are marked red. Most of the chosen segments are distributed on the surface of the deep drawing tool. Covered segments include the

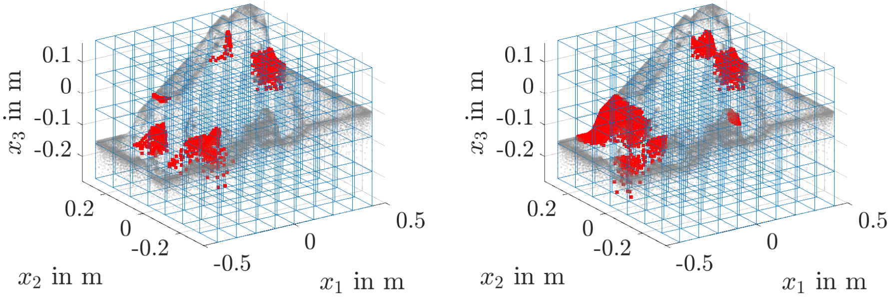

(a) Approach (4.2)

(b) Approach (4.3)

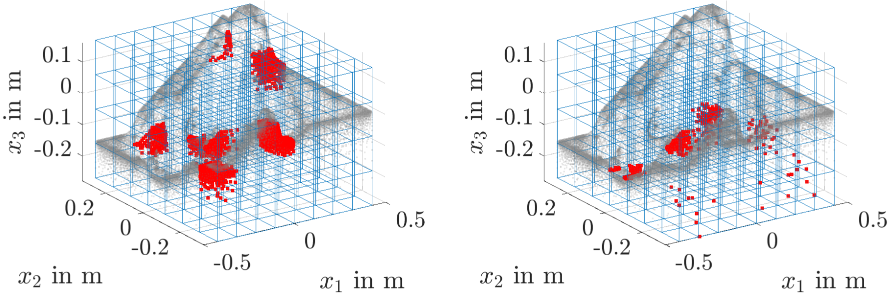

(c) Approach (4.4)

(d) Approach (4.5)

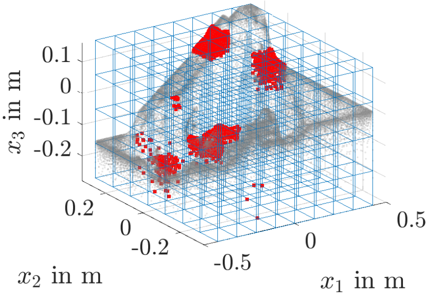

(e) Approach (4.6)

Figure 4.3.: Selected sensor segments for the different optimization routines based on the full model.

area with highest x_3-value, the center and the lower part in negative x_1-direction. The flat area with positive x_1- and negative x_2-value is neglected in most cases. Maximizing the rank of W_o differs significantly. In this case many segments are inside the tool.

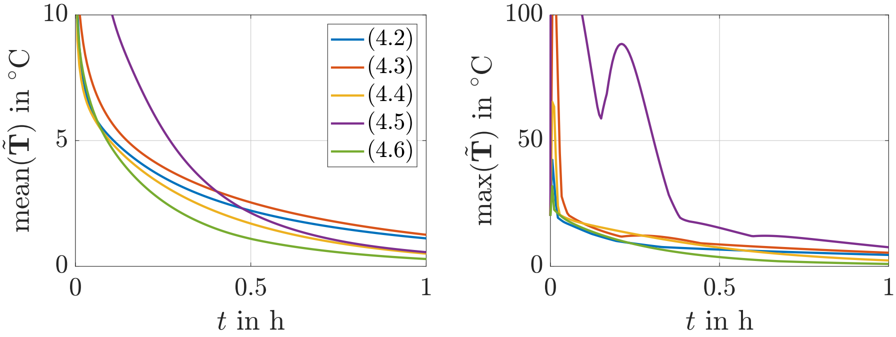

Figure 4.4.: Comparison of the resulting estimation error for the sensor locations of Fig. 4.3.

Remark 1 (Estimator Design) *To compare the performance of these sensor configurations an estimator is set up using the ROM* (3.8) *obtained from balanced truncation. There is a different ROM for each configuration, because the ROM depends on the output matrix C, which is set up by placing imaginary sensors at nodes near the center of the selected segments. For this purpose, a Kalman filter is used*

$$E_r\dot{\hat{\boldsymbol{T}}}_r = A_r\hat{\boldsymbol{T}}_r + B_r\boldsymbol{u} + L\left(\boldsymbol{y} - \hat{\boldsymbol{y}}\right), \qquad t > 0 \tag{4.8a}$$

$$\hat{\boldsymbol{T}}_r(0) = \hat{\boldsymbol{T}}^0 \tag{4.8b}$$

$$\hat{\boldsymbol{y}} = C_r\hat{\boldsymbol{T}}, \qquad t \geq 0. \tag{4.8c}$$

minimizing the variance of the estimation error $\tilde{\boldsymbol{T}}_r(t) = \boldsymbol{T}_r(t) - \hat{\boldsymbol{T}}_r(t)$ *under the assumption of zero mean Gaussian process and measurement noise with covariances Q and R [24]. The static estimator gain matrix from* (4.8) *follows as* $L = PC_r^TR^{-1}$ *with the covariance matrix P obtained from solving the algebraic Riccati equation*

$$0 = E_rPA_r^T + A_rPE_r^T - E_rPC_r^TR^{-1}C_rPE_r^T + Q.$$

This equation is not solvable for the full order model with a computer equipped with 16 GB *RAM, which justifies the usage of the ROM. In the evaluations an appropriate input* $\boldsymbol{u}$ *is chosen.*

Fig. 4.4 shows the estimation errors from the different sensor configurations. To guarantee comparability the matrices Q and R are identity matrices for all configurations. The errors from the full model $\tilde{\boldsymbol{T}} = V\tilde{\boldsymbol{T}}_r$ are compared. The average error considering all nodes' $\text{mean}(\tilde{\boldsymbol{T}}(t)) = \sum_{i=1}^{n} \tilde{T}_i(t)/n$ is shown on the left and the maximum error of all nodes $\max(\tilde{\boldsymbol{T}}(t))$ is shown on the right. Table 4.1 summarizes average estimation errors over a five hour time interval. Maximizing the rank of W_o in (4.5) gives poor results. The SVD reduced observability Gramian matrices has full rank in many cases, so this sensor configuration is nearly random. Maximizing the minimal eigenvalue of W_o using (4.6) emerges as the best sensor configuration. This measure is therefore given special consideration for comparison with the respective ROMs. Table 4.1 also shows the value of $\lambda_{\min}(W_o)$. This measure tends to evaluate sensor placement reasonably. Thus, (4.5) providing the worst observation result also implies the smallest value of $\lambda_{\min}(W_o)$.

Approach	mean($\tilde{T}(t)$)	max($\tilde{T}(t)$)	$\lambda_{\min}(W_o)$
(4.2)	0.7960	2.6708	1.2282e-05
(4.3)	0.8647	3.4461	7.8567e-06
(4.4)	0.5232	2.0963	1.1628e-07
(4.5)	0.8563	10.0819	1.1645e-10
(4.6)	0.4226	1.2924	7.1687e-05

Table 4.1.: Estimation error analysis for Fig. 4.4.

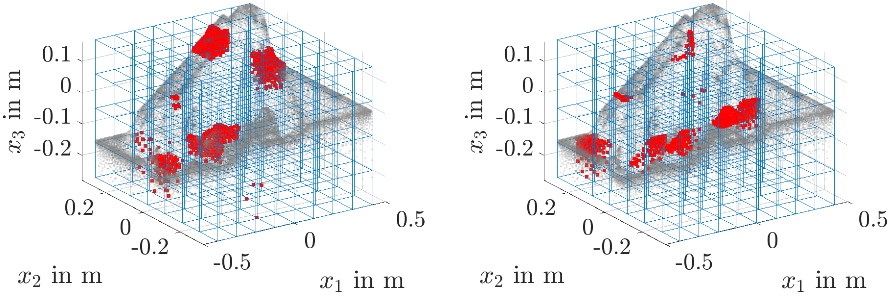

(a) Approach (4.6)

(b) BT

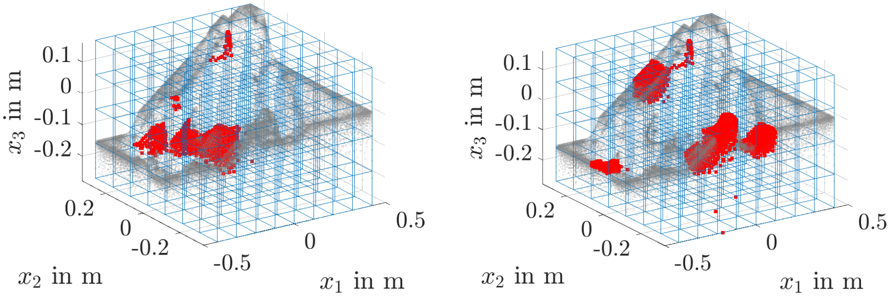

(c) IRKA

(d) POD

Figure 4.5.: Selected sensor segments for (4.7) using different ROMs. Subfigure 4.5(a) is added for comparison.

4.3.2. Comparison of ROMs

Secondly, the discussed ROMs are used for optimal sensor placement by making use of the measure (4.7) and $p_{\max} = 8$. The arising mixed-integer optimization problems are solved as before. Fig. 4.5 summarizes the resulting sensor locations based on the computation with the full order model (here (4.6) is applied) and ROMs based on BT, IRKA and POD. In comparison to

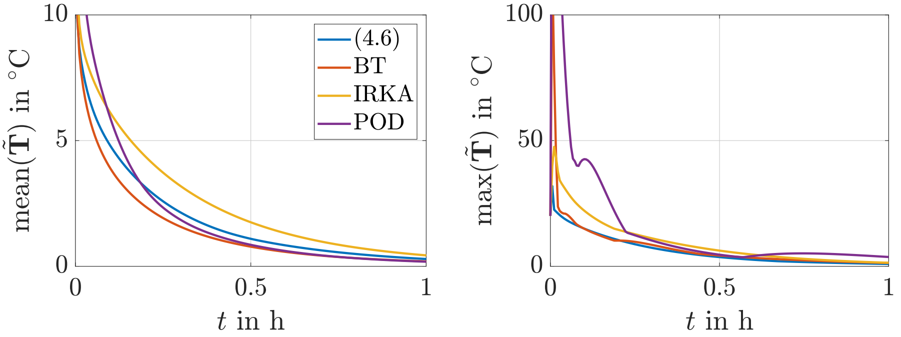

Figure 4.6.: Comparison of thew resulting estimation error for the sensor locations of Fig. 4.5 obtained for different ROMs.

Approach	$\mathrm{mean}(\tilde{T}(t))$	$\max(\tilde{T}(t))$	$\lambda_{min}(W_{o,BT})$
(4.6)	0.4226	1.2924	10.04
BT	0.3369	1.6438	96.33
IRKA	0.5740	2.0202	39.88
POD	0.4373	3.5061	4.68

Table 4.2.: Estimation error analysis for Fig. 4.6.

the sensor placement based on the full order model, the result obtained using the IRKA-ROM shows some tendency to locate sensors in the part with negative x_1-coordinate. The result of the BT-ROM configuration resembles the sensor segments of the full order model. The segments of the POD-ROM configuration are fewer represented in the middle of the tool. The performance of these sensor configurations is compared similarly to the previous case by setting up a respective estimator. As before the matrices Q and R are chosen as identity matrices for all configurations.

Fig. 4.6 and Table 4.2 enable to compare the estimator performances using the sensor locations determined based on the ROMs with those summarized in Fig. 4.4 and Table 4.1 obtained for the full order model. The mean estimation error is largest for model order reduction by the IRKA. The mean error for the POD is nearly equal to the error of the full model, but the maximum error is larger. Using MOR based on BT leads to the best estimation results. The average error in all nodes is even below the error of the full model. Table 4.2 also shows the function value of $\lambda_{\min}(W_{o,\mathrm{BT}})$. Here, a higher value does not automatically lead to a smaller estimation error.

4.3.3. Variation of the Number of Sensors

In the previous optimizations the maximum number of sensors was chosen to be $p_{\max} = 8$. To evaluate this choice the obtained values of measure (4.7) using the BT-ROM with increasing

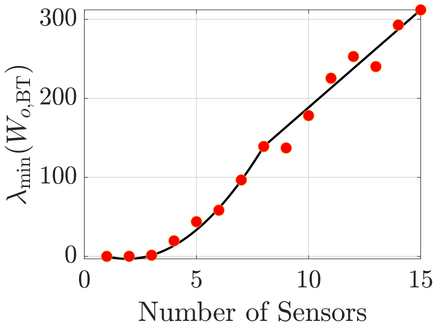

Figure 4.7.: Measure (4.7) using BT-ROM for different maximum number of sensors $p_{\max}$.

$p_{\max}$ are compared. This is depicted in Fig. 4.7. The value of $\lambda_{\min}(W_{o,\mathrm{BT}})$ is rising approximately exponentially until $p_{\max} = 8$ and then changes to a linear increase. Hence, assigning $p_{\max} = 8$ seems a reasonable choice and good compromise between effort and effect as can also be seen from the estimation results in Figs. 4.4 and 4.6. It is worth noting that the maximum number of sensors $p_{\max}$ is always equal to the actual number of sensors. It follows that (4.2b) can also be formulated as $\sum_{i=1}^{p} \chi_i = p_{\max}$.

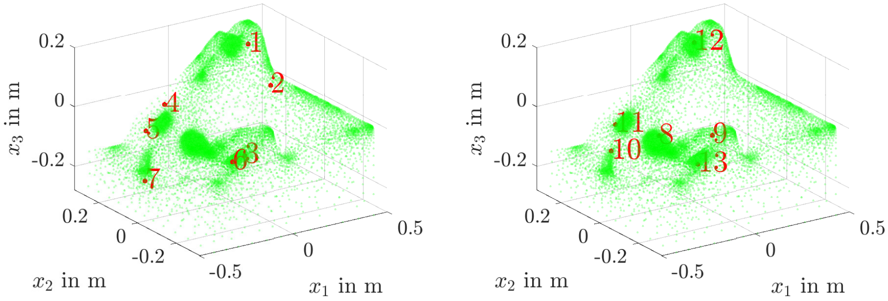

(a) Sensors in the outer die.

(b) Sensors in the insertion elements.

Figure 4.8.: Placed sensors in the die: outer die and insertion elements.

Based on the presented results for optimal sensor placement the sensor configuration depicted in Fig. 4.8(a) is realized. The sensors are placed in the segments selected from measure (4.7) using BT-ROM. Herein one segment, which is located right next to an actuator, was left out as this is covered by a local thermocouple built in near the used heating cartridges. The further sensors located in the insertion elements are depicted in Fig. 4.8(b). The resulting output equation corresponds to (3.6) with $p = 13$ sensors. The numbers next to the position points define the respective index in the output vector $\boldsymbol{y}$.

5. Feedback Control Design

Knowledge of the current spatial–temporal temperature distribution is the starting point for feedback control design. For this, a linear quadratic regulator with integral part is set up combined with a Kalman filter to react efficiently to changes in the distribution resulting from disturbances or from the forming process. For reasons of comparison also a proportional derivative (PD) controller is designed.

5.1. Desired Temperature Profile

For the deep drawing tool it is in particular required to achieve a desired transient temperature profile in the six zones shown in Fig. 5.1. These zones include the nodes of the top surfaces of the six insertion elements.

This profile is subsequently summarized in the vector

$$\boldsymbol{y}_{\text{targ}} = C_{\text{targ}}\boldsymbol{T}, \quad t \geq 0 \tag{5.1}$$

with the matrix $C_{\text{targ}} \in \mathbb{R}^{q \times n}$ extracting the mean value of the nodal temperatures from $\boldsymbol{T}(t)$ for each zone. The integer q is 6 as there are six zones. In steady state with the input $\boldsymbol{u}^s$ and the temperature profile $\boldsymbol{T}^s$ (5.1) can be expressed as

$$\boldsymbol{y}^s_{\text{targ}} = C_{\text{targ}}\boldsymbol{T}^s = C_{\text{targ}}(-A)^{-1}B\boldsymbol{u}^s.$$

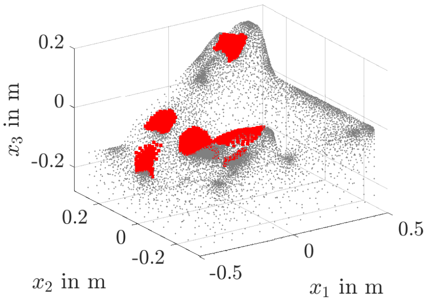

Figure 5.1.: Die with the six red marked critical areas.

Given steady state target temperatures $\boldsymbol{y}^s_{\text{targ}}$ the corresponding input $\boldsymbol{u}^s$ hence follows by making use of the the Moore–Penrose inverse, i.e.,

$$\boldsymbol{u}^s = (C_{\text{targ}}(-A)^{-1}B)^{\dagger}\boldsymbol{y}^s_{\text{targ}}. \tag{5.2}$$

Finally, (5.2) calculates the constant input $\boldsymbol{u}^s$ required to reach the desired temperatures in the target zones $\boldsymbol{y}^s_{\text{targ}}$ when steady state is reached. In steady state the die including the insertion elements approaches an almost constant temperature. The actuators only counteract the heat loss via convection.

The transition between different steady state temperature profiles in the die can be realized efficiently within a specified time interval making use of a trajectory planning. Flatness based approaches [23] are proposed by, e.g., [13, 2, 50] using, e.g., a Gevrey function. In the following remark an example is given for this deep drawing process.

Remark 2 (Flatness-based Trajectory Planning) *The flatness property of the system* (3.1) *can be used for a trajectory planning. In particular, a differential parameterization of all system states and inputs in terms of a flat output is determined following in principle an inversion approach. Thus, by specifying a suitable target trajectory for the flat output, a feedforward control can be developed directly by evaluating the input parameterization. This realizes the corresponding system behavior described by the corresponding evaluation of the state parameterization in open loop under nominal conditions. It is advantageous that the evaluations are purely algebraic and, in contrast to methods of optimal control, do not require the solution of differential equations.*

The reduced system (3.8) *with dimension r is used for trajectory planning. Assuming mutually disjoint eigenvalues of system dynamic matrix A, the Laplace transform of* (3.8)

$$s\hat{\boldsymbol{T}}_r = A_r\hat{\boldsymbol{T}}_r + B_r\hat{\boldsymbol{u}} \tag{5.3}$$

is taken to parameterize the flat output. A rearrangement of equation (5.3) *is built to get an expression for $\hat{\boldsymbol{T}}_r$. This leads to*

$$\hat{\boldsymbol{T}}_r = (sI - A_r)^{-1}B_r\hat{\boldsymbol{u}} = -(I - sA_r^{-1})^{-1}A_r^{-1}B_r\hat{\boldsymbol{u}} = -\frac{\operatorname{adj}(I - sA_r^{-1})}{\det(I - sA_r^{-1})}A_r^{-1}B_r\hat{\boldsymbol{u}}.$$

The differential operators

$$D^x(s) = \operatorname{adj}(I - sA_r^{-1}) = \operatorname{diag}\left[\prod_{\substack{j=1\\ j\neq k}}^{r}\left(1 - \frac{s}{\lambda_j}\right)\right]_{k=1}^{r},$$

$$D^u(s) = \det(I - sA_r^{-1}) = \prod_{j=1}^{r}\left(1 - \frac{s}{\lambda_j}\right)$$

are defined. Introducing the flat output $\hat{\boldsymbol{\zeta}}(s) = \dfrac{\hat{\boldsymbol{u}}(s)}{D^u(s)}$ *leads to the state and input parametrizations*

$$\hat{\boldsymbol{T}}_r = -D^x(s)A_r^{-1}B_r\hat{\boldsymbol{\zeta}}, \quad \hat{\boldsymbol{u}} = D^u(s)\hat{\boldsymbol{\zeta}}.$$

The expressions are transformed to the time domain, which leads to

$$\boldsymbol{T}_r = -D^x\left(\frac{d}{dt}\right) \circ A_r^{-1}B_r\boldsymbol{\zeta}, \tag{5.4a}$$

$$\boldsymbol{u} = D^u\left(\frac{d}{dt}\right) \circ \boldsymbol{\zeta} = \sum_{i=0}^{r} p_i \partial_t^i \boldsymbol{\zeta}(t). \quad p_0 = 1 \tag{5.4b}$$

As described in Section 5.1 it is in particular required to achieve a desired transient temperature profile in the six zones of the deep drawing tool shown in Fig. 5.1. In steady state $\boldsymbol{u}^s = \boldsymbol{\zeta}^s$ *holds true. Using* (5.2) *and defining* $\boldsymbol{\zeta}_T^s$ *as the input needed to reach the temperature profile* T *in steady state*

$$\boldsymbol{\zeta}_T^s = (C_{\text{targ}}(-A)^{-1}B)^{\dagger}\boldsymbol{y}_{\text{targ}}^* \tag{5.5}$$

can be derived. A target trajectory for implementing a transition between two operating points described by the value of the flat output at the start time and the value of the flat output at the end time can be given by

$$\boldsymbol{\zeta}^* = \boldsymbol{\zeta}_0^s + (\boldsymbol{\zeta}_T^s - \boldsymbol{\zeta}_0^s)\Phi_T.$$

Here, for formal mathematical reasons, a so-called Gevrey function (introduced, i.e., in [23]) is selected. This function can be defined as

$$\Phi_T(t) = \begin{cases} 0, & t \leq 0 \\ 1, & t \geq T \\ \frac{\int_0^t \Theta_{\omega,\tau}(\tau)d\tau}{\int_0^T \Theta_{\omega,\tau}(\tau)d\tau}, & t \in (0,T) \end{cases}$$

with

$$\Theta_{\omega,\tau}(\tau) = \begin{cases} 0, & t \notin (0,T) \\ \exp\left(-\left(\left[1 - \frac{t}{T}\right]\frac{t}{T}\right)^{-\omega}\right). & t \in (0,T) \end{cases}$$

The parameter T *defines the transition time and* ω *tunes the steepness of* $\Phi_T(t)$. *The demanded temperature of* $T = 150\,^{\circ}\mathrm{C}$ *within the target zones is attained by defining* $\boldsymbol{\zeta}_T^s$ *as:*

$$\boldsymbol{\zeta}_T^s = \begin{bmatrix} 0.2489 & 0.2699 & 0.2865 & 0.1641 & 0.2191 & 0.6315 \end{bmatrix}^T.$$

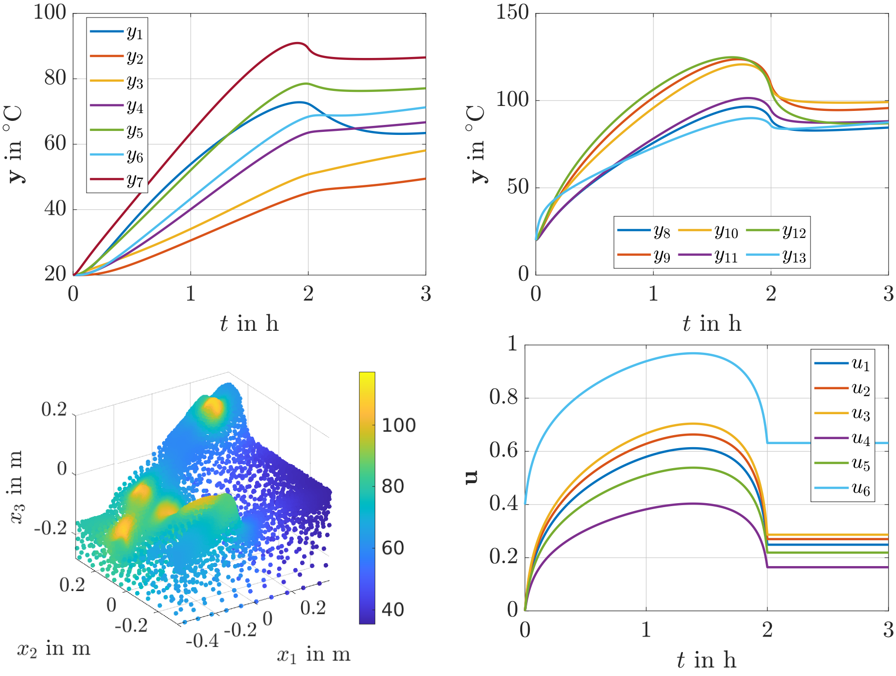

Figure 5.2.: Temperature evolution in the die (left above) and in the insertion elements (right above), the temperature profile after three hours (left below) and the input (right below) for the simulative flatness based trajectory planning for the die.

This definition is based on the utilization of (6.1) *from Section 6.2.1. The starting profile,* $\boldsymbol{\zeta}_0^s$, *is employed as:*

$$\boldsymbol{\zeta}_0^s = \begin{bmatrix} 0 & 0 & 0 & 0 & 0 & 0.4 \end{bmatrix}^T .$$

The transition time is configured to $T = 7200\,\mathrm{s}$ *and the steepness parameter,* ω, *is set at* 0.25. *The determination of* $\boldsymbol{u}$ *from* $\boldsymbol{\zeta}$ *is accomplished using Equation* (5.4b), *and this process incorporates 95 derivatives in the differential operator by setting* $r = 95$. *Efficient evaluation of* (5.4b) *is enabled through the utilization of the* (q, ξ)*-approximate* k*-summation, denoted as* $S_k^{q,\xi}$, *as introduced in [51]. It is defined as follows:*

$$\boldsymbol{u} \mapsto \left(S_k^{r,\xi}\boldsymbol{u}\right) = \frac{\sum_{j=0}^{q} \boldsymbol{s}_j \frac{\xi^j}{\Gamma(1+jk)}}{\sum_{j=0}^{q} \frac{\xi^j}{\Gamma(1+jk)}} .$$

Here, the partial sum $\boldsymbol{s}_j$ *is represented as the sum of* p_i *times* $\partial_t^i \boldsymbol{\zeta}(t)$, *with* $q \leq r$ *denoting the number of used derivatives. The appropriate selection of summation parameters is characterized by* $\xi = 0.4$ *and* $k = 1$.

The chosen scenario was simulated and the temperature profile after three hours (left below), temperature development inside the outer sensors (left above), the sensors next to the actuators (right above), and the input (right below) are depicted in Fig. 5.2.

5.2. Linear Quadratic Gaussian Control

As soon as the (nearly) steady state of the temperature distribution in the die is reached, the deep drawing operations can be carried out with the die. It is expected that during a cycle the die will cool down considerably due to the cold sheet metal, which is pressed against the die by the cold punch. For this process, a controller must be designed to adjust the heating power of the actuators in such a way that the reaction to the heat loss is as fast and efficient as possible. To this end, a linear quadratic (LQ) regulator is designed, which is supplemented by an integral component to counteract possible model inaccuracies. This model-based controller is amended by a Kalman filter as a state estimator. The design of the Kalman filter is described in Section 4.3. Both controller and estimator are based on the BT reduced model of dimension $r = 95$ for computability reasons.

For control design the model (4.8) is extended by an integral part [78]. Let $\boldsymbol{y}_{8:13}(t) \in \mathbb{R}^{6\times r}$ denote the (measured) sensor values in the insertion elements according to Fig. 4.8(b) and let $C_{8:13}$ and $C_{r,8:13}$ denote the corresponding submatrices of the output matrix C for the full model and for the BT-ROM. With this consider the extended system

$$\underbrace{\begin{bmatrix} E_r & 0 \\ 0 & I_6 \end{bmatrix}}_{=E_{r,\text{ex}}} \begin{bmatrix} \dot{\boldsymbol{T}}_r \\ \dot{\boldsymbol{e}}_I \end{bmatrix} = \underbrace{\begin{bmatrix} A_r & 0 \\ -C_{r,8:13} & 0 \end{bmatrix}}_{=A_{r,\text{ex}}} \begin{bmatrix} \boldsymbol{T}_r \\ \boldsymbol{e}_I \end{bmatrix} + \underbrace{\begin{bmatrix} B_r \\ 0 \end{bmatrix}}_{=B_{r,\text{ex}}} \boldsymbol{u} + \begin{bmatrix} 0 \\ \boldsymbol{y}_{8:13} \end{bmatrix} \tag{5.6}$$

with I_6 denoting the 6×6 identity matrix. Here, $\boldsymbol{e}_I = \int_0^t (\boldsymbol{y}_{8:13} - \hat{\boldsymbol{y}}_{8:13}) dt$ is the integrated estimator error of the sensors in the insertion elements. Once (5.6) is asymptotically stable, i.e., its rest position is reached, it follows that $\boldsymbol{y}_{8:13} - \hat{\boldsymbol{y}}_{8:13} = 0$ due to $\dot{\boldsymbol{e}}_I = 0$. The state feedback control is then set up according to

$$\boldsymbol{u} = -K \begin{bmatrix} \boldsymbol{T}_r \\ \boldsymbol{e}_I \end{bmatrix} + H\boldsymbol{r} \tag{5.7a}$$

with $H \in \mathbb{R}^{m\times 6}$ a prefilter matrix and $\boldsymbol{r}(t) \in \mathbb{R}^6$ some reference trajectory. For the determination of K the quadratic cost functional[1]

$$J = \int_0^\infty \begin{bmatrix} \boldsymbol{T}_r \\ \boldsymbol{e}_I \end{bmatrix}^T Q \begin{bmatrix} \boldsymbol{T}_r \\ \boldsymbol{e}_I \end{bmatrix} + \boldsymbol{u}^T R \boldsymbol{u}.$$

---

[1] Note that alternatively the linear quadratic regulator can be set up to minimize the weighted difference between $\boldsymbol{y}_{\text{targ}}(t)$ and $\boldsymbol{r}(t)$.

is minimized with the positive definite matrices Q and R to balance the individual contributions of the extended state $[\boldsymbol{T}_r(t), \boldsymbol{e}_I(t)]T \in \mathbb{R}^{n_x}$, $n_{\text{ex}} = r + 6$ and the input input $\boldsymbol{u}$. Subsequently, diagonal matrices $Q \in \mathbb{R}^{n_{\text{ex}} \times n_{\text{ex}}}$ and $R \in \mathbb{R}^{m \times m}$ are assigned. With this

$$K = R^{-1} B_{r,\text{ex}}^T P. \tag{5.7b}$$

is obtained [24], where P solves the Riccati equation

$$0 = A_{r,\text{ex}}^T P E_{r,\text{ex}} + E_{r,\text{ex}}^T P A_{r,\text{ex}} - E_{r,\text{ex}}^T P B_{r,\text{ex}} R^{-1} B_{r,\text{ex}}^T P E_{r,\text{ex}} + Q$$

Similar to the estimator design this equation is not solvable for the full order model on a standard PC, which justifies the use of the ROM for controller design. The prefilter matrix H is in this setup used to impose that $\boldsymbol{y}_{\text{targ}}(t)$ defined in (5.1) approaches the reference trajectory $\boldsymbol{r}(t)$ asymptotically as $t \longrightarrow \infty$. Substitution of (5.7a) into (5.6) and taking into account (5.1), i.e.,

$$\boldsymbol{y}_{\text{targ}} = C_{\text{targ}} \boldsymbol{T} = C_{\text{targ},r} \boldsymbol{T}_r = C_{\text{targ},r,\text{ex}} \begin{bmatrix} \boldsymbol{T}_r \\ \boldsymbol{e}_I \end{bmatrix},$$

yields for $t \longrightarrow \infty$

$$H = -\left(C_{\text{targ},r,\text{ex}} \left(A_{r,\text{ex}} - B_{r,\text{ex}} K \right)^{-1} B_{r,\text{ex}} \right)^{\dagger}. \tag{5.7c}$$

Due to the integral part in terms of $\boldsymbol{e}_I(t)$ an anti-windup scheme is required to address the input constraints $u_j \in [0, 1]$, $j = 1, \dots, m$. The integration is stopped whenever the constraints are violated as described in [29].

Fig. 5.3 provides a block diagram of the closed control loop including the BT reduced model, Kalman filter, LQ regulator with integral part and reference trajectory.

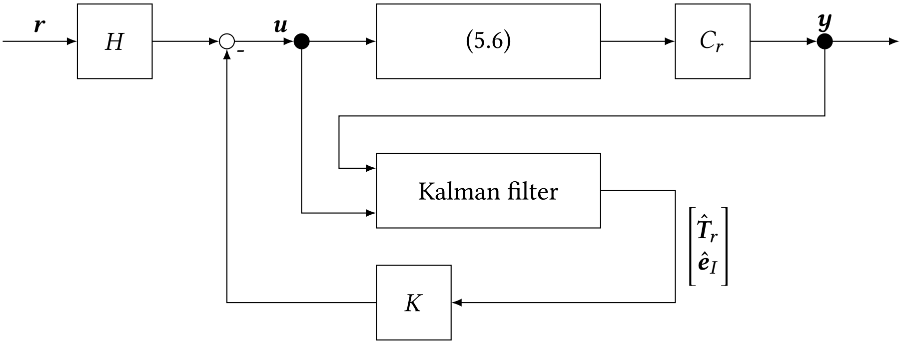

Figure 5.3.: Block diagram of the closed control loop including the BT reduced model, Kalman filter, LQ regulator with integral part and reference trajectory.

5.3. Proportional Derivative Control

Alternatively a proportional derivative (PD) controller is designed, which uses the knowledge of temperature model to calculate the target values $\boldsymbol{y}^s_{8:13}$ of the thermocouples in the insertion elements, but runs without estimator and simulator only using the input/output (I/O) behavior. This is advantage concerning real-time applicability, but it does not provide full information about the temperature profile during the process. The target output values $\boldsymbol{y}^s_{8:13}$ are calculated using (5.2):

$$\boldsymbol{y}^s_{8:13} = C_{r,8:13}(-A_r)^{-1}B_r\boldsymbol{u}^s. \tag{5.8}$$

The constant input $\boldsymbol{u}^s$ is required to reach the desired temperatures in the target zones $\boldsymbol{y}^s_{\text{targ}}$ when steady state is reached. Here, $\boldsymbol{y}^s_{8:13}$ is the temperature at the thermocouples. The control law of the PD controller is

$$\begin{aligned} \boldsymbol{u}(t_k) =& K_p\left(\boldsymbol{y}^s_{8:13} - \boldsymbol{y}_{8:13}(t_k)\right) \\ &+ K_d\frac{\left(\boldsymbol{y}^s_{8:13} - \boldsymbol{y}_{8:13}(t_k)\right) - \left(\boldsymbol{y}^s_{8:13} - \boldsymbol{y}_{8:13}(t_{k-1})\right)}{\Delta t}. \end{aligned} \tag{5.9}$$

Fig. 5.4 provides a block diagram of the closed PD control loop including the I/O behavior of the model, target temperatures $\boldsymbol{y}^s_{8:13}$, inputs $\boldsymbol{u}$ and outputs $\boldsymbol{y}_{8:13}$.

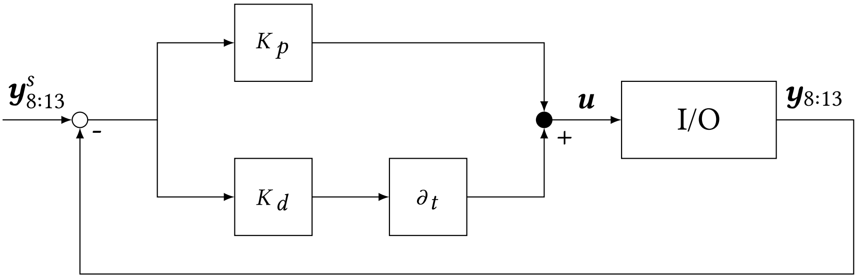

Figure 5.4.: Block diagram of the closed PD control loop including the I/O behavior of the model, target temperatures $\boldsymbol{y}^s_{8:13}$, inputs $\boldsymbol{u}$ and outputs $\boldsymbol{y}_{8:13}$.

6. Experimental Validation

After briefly describing the experimental setup, the determined model (3.4) and (3.6), the estimator design based on the BT reduced model in (4.8), the chosen controller based on the BT reduced model in (5.6), and the PD controller in (5.9) are validated experimentally.

6.1. Experimental Setup

The used experimental die and punch are shown in Fig. 6.1. The colored ellipsoids indicate the positions of the insertion elements, corresponding to the colors used in Fig. 2.3.

For control purposes a hot runner controller (Hotset HR30 from Hotset GmbH) is used, which is connected to the embedded actuators and the sensors placed in the insertion elements. An USB data acquisition device (RedLab TC from Meilhaus Electronic) reads out the temperature of the sensors placed in the outer die. Moreover, a serial connection between the COM port of an USB converter connected to a computer and the COM port of the hot runner controller via RS485 is established in the software MATLAB. Estimator and controller are implemented using MATLAB and are evaluated online on the computer with a sampling time of $\Delta t = 1\,\mathrm{s}$. The whole setup is visualized schematically in Fig. 6.2.

The sheet examined is a 1050 aluminum alloy with a thickness of 0.5 mm. Fig. 6.3 depicts three formed products after the completed deep drawing process. The colored ellipsoids again mark

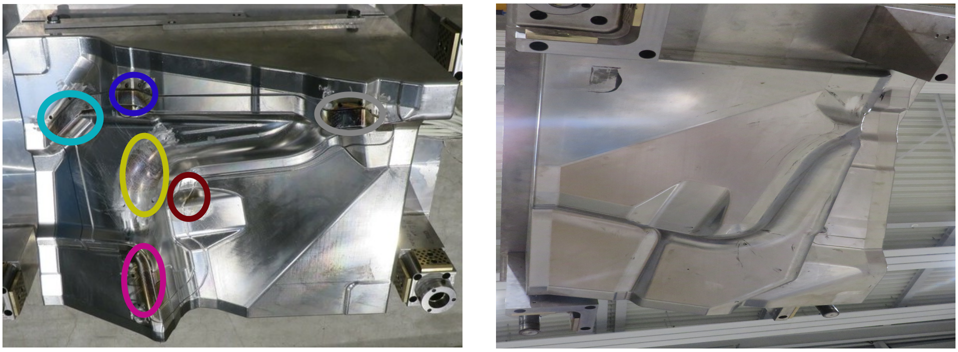

Figure 6.1.: Top view of the experimental die (left) and punch (right). The colored ellipsoids mark the positions of the insertion elements with respect to the used colors in Fig. 2.3.

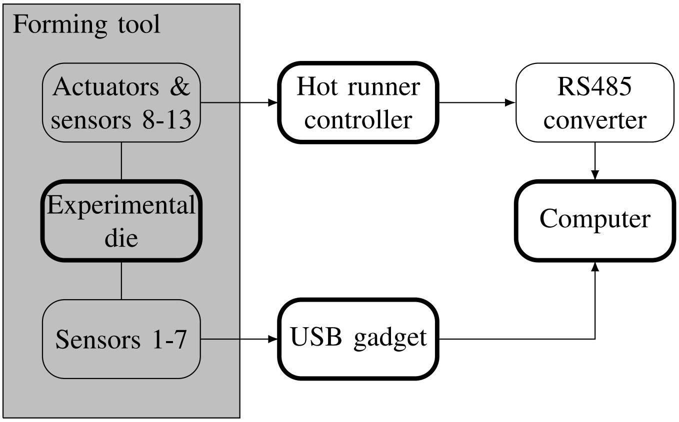

Figure 6.2.: Interactions between die, hot runner controller, USB gadget and computer in the experimental setup.

the positions of the insertion elements with respect to the used colors in Fig. 2.3. The blank in Fig. 6.3(a) was produced without heating the die. Here, many wrinkles occur. The blank in Fig. 6.3(b) was produced in a controlled process with the effect of an enormous wrinkle reduction. However, there are still many wrinkles, but this was expected due to the very complex setup in order to serve as a benchmark process. The results are similar to those of Fig. 2.4, where the desired temperature profile was achieved in an open control loop. Closed loop control is necessary in order to ensure the desired temperature in the long term. The process was also run with a calotted 1050 aluminum alloy with a thickness of 0.5 mm. Fig. 6.3(a) shows a finished calotted sheet metal after a controlled process. This material constitution reduces the occurrence of wrinkles and cracks beside the temperature of the die. Note that the black rectangles in the pictures are placed in order to hide writings on the finished blanks.

6.2. Estimator Validation

To analyze the performance of the Kalman filter designed based on the BT-ROM (3.8) eleven sensors are used for the estimator, while sensors no. 4 and 11 of Fig. 4.8 are used for validation purposes. This enables us to compare the temperatures estimated by the filter with the temperatures measured by the sensors. From these, one is located in an insertion element while the other one is placed in the outer die. However, this setup weakens the functionality of the estimator in comparison to the one using all thirteen sensors for estimation. Two experimental scenarios are considered for the validation. The matrices Q and R are identity matrices again. The ambient temperature $T_\infty = 20\,^\circ\mathrm{C}$ is subtracted from the output $\boldsymbol{y}$ as (3.5) still holds.

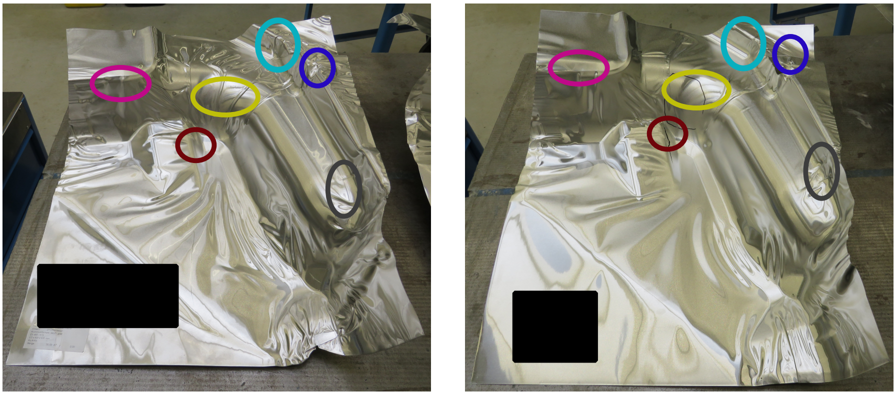

[redacted]

[redacted]

(a) Formed blank without control.

(b) Formed blank with control.

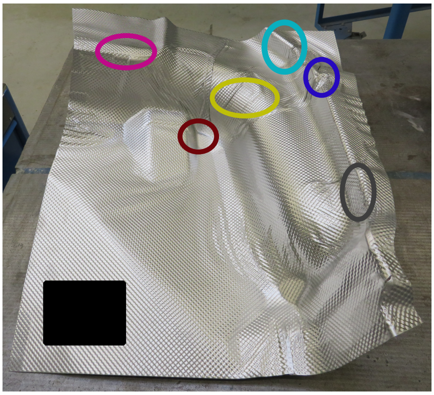

[redacted]

(c) Formed calotted blank with control.

Figure 6.3.: Formed blanks after the completed deep drawing process. The colored ellipsoids mark the positions of the insertion elements with respect to the used colors in Fig. 2.3.

6.2.1. Heat-up with forming step

To validate the Kalman filter a scenario with constant input

$$\boldsymbol{u}^s = [0.2489, 0.2699, 0.2865, 0.1641, 0.2191, 0.6315]^T \tag{6.1}$$

is set up. This input corresponds according to (5.2) to a target temperature profile of $\boldsymbol{y}^s_{\text{targ}} = 130 \times \mathbf{1}\,^\circ\text{C}$ under steady state conditions inside the target zones. Due to the mapping (3.5) with an ambient temperature of $T_\infty = 20\,^\circ\text{C}$ this equals a temperature of $150\,^\circ\text{C}$.

Applying $\boldsymbol{u}(t) = \boldsymbol{u}^s$ the temperature in the tool rises from the initial temperature of $25\,^\circ\text{C}$ for a period of about $1600\,\text{s}$. Fig. 6.4 shows the evolution of the sensor values in the outer die

(Fig. 6.4(a)) and inside the insertion elements (Fig. 6.4(b)). The respective estimator errors at all sensor locations are visualised below for those in the outer die (Fig. 6.4(c)) and in the insertion elements (Fig. 6.4(d)). The vertical magenta dotted line indicates the point at which the punch reaches the bottom dead center during the forming step. Snapshots of the temperature profiles reconstructed by the estimator using the projection (3.7), i.e., $\hat{\boldsymbol{T}} = V\hat{\boldsymbol{T}}_r$, at $t = 5$ s and $t = 1600$ s are provided in Fig. 6.4(e) and Fig. 6.4(f). At the sensors placed inside the die the measured temperature rises nearly linear except for sensors 5 and 7, where the increase slows down a little as the steady state temperature value becomes closer. The sensors inside the insertion elements reach appropriately their steady state temperature during this scenario. At $t = 1303$ s a forming step starts with the punch moving downwards. At $t = 1323$ s the bottom dead point is reached and and is held for 30 s. At $t = 1353$ s the punch starts moving upwards to its upper dead center. Due to the contact of the die with the metal sheet, which is inserted at room temperature, a temperature drop can be observed, which is followed by a slow increase. This effect can be seen also, but to a much lower extent, in the sensors in the outer die. The evolution of the estimation errors confirms that the estimator works well. At the validation point given by sensor 4 the error reaches a negligible value of about 0.5 °C. The error is higher in the insertion elements, which is confirmed by the estimator error obtained at the position of sensor 11, where a difference of up to 20 °C between the Kalman filter estimation and the measurement becomes apparent that decreases successively. After the forming step this error increases again due to the contact with the metal sheet. It is worth noting that this particular difference appears next to an actuator. The difference in the outer die is much smaller, so that this error probably is just around the heater. In the whole estimator using the test sensors for estimation this error will likely be much smaller. However, no further test sensor has been placed to prove this. Despite these local differences in the quality of the estimation it can be concluded that the BT-ROM is suitable for estimator design and that the Kalman filter provides a sufficiently accurate temperature estimation in the complete die. In particular the estimator enables to reconstruct the spatial-temporal temperature profile in the tool as can be seen in terms of the snapshots shown in Fig. 6.4 (bottom).

6.2.2. Cool down with forming step

As a seconds scenario the cool down of the die is considered for $\boldsymbol{u} = \boldsymbol{0}$ in Fig. 6.5. Starting with temperatures of up to 500 °C in the die the decay behavior, shown in Fig. 6.5(a) for the sensor in the outer die and Fig. 6.5(b) for those in the insertion elements, is obtained. Forming steps are performed at times $t = 423$ s and $t = 1532$ s. In both cases the punch needs 20 s to reach the bottom dead center and stays there for 30 s. At times $t = 473$ s and $t = 1582$ s the punch starts moving upwards to its upper dead center. The vertical magenta dotted line again marks the point, where the punch reaches the bottom dead point during the forming step. Due to the contact with the sheet entering the tool at approximately ambient temperature a significant cooling at the insertion elements is initiated. The estimator errors converge to zero in both the outer die (see validation sensor 4 in Fig. 6.5(c)) and the insertion elements (see validation sensor 11 in Fig. 6.5(d)). During the forming steps a short rise can be seen due to the changed contact situation. The estimated spatial-temporal temperature profiles shortly after the beginning and at the end of the cool down with forming steps are depicted in Fig. 6.5(e) and Fig. 6.5(f).

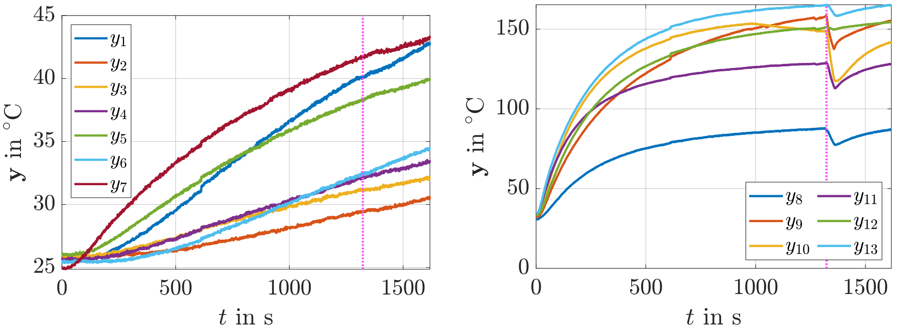

(a) Temperature evolution in the outer die.

(b) Temperature evolution in the insertion elements.

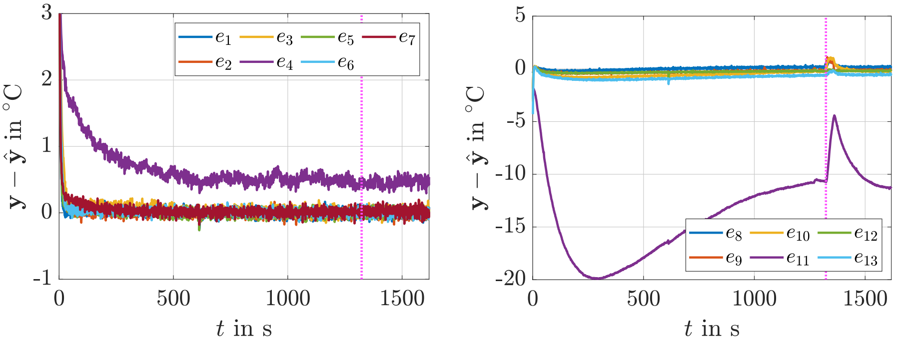

(c) Estimator error for sensor positions in the outer die.

(d) Estimator error for sensor positions in the insertion elements .

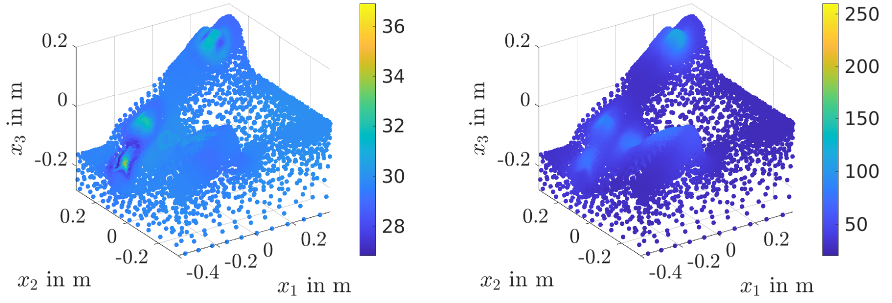

(e) Snapshot of the estimated temperature profile at $t = 5$ s.

(f) Snapshot of the estimated temperature profile at $t = 1600$ s.

Figure 6.4.: Temperature evolutions, estimator errors and snapshots of the heat-up with forming step. The vertical magenta dotted line marks the point, where the punch reaches the bottom dead point during the forming step.

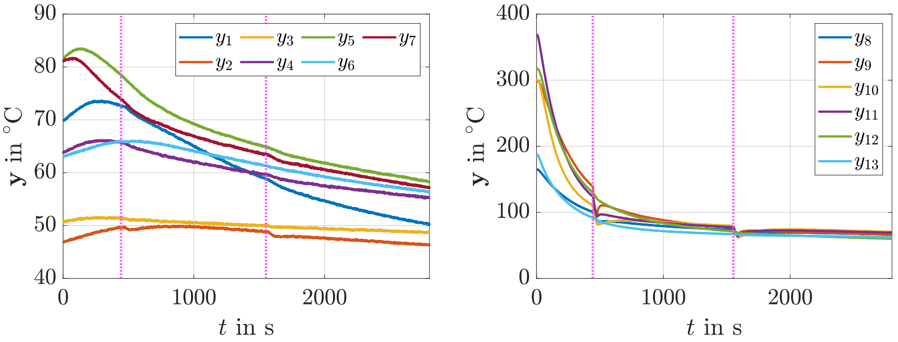

(a) Temperature evolution in the outer die.

(b) Temperature evolution in the insertion elements.

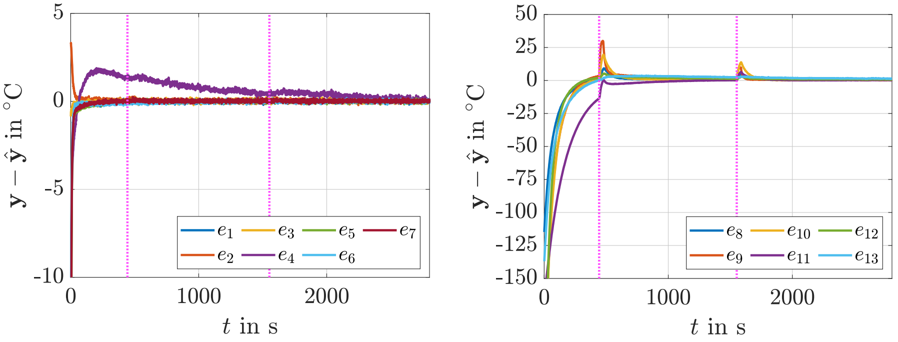

(c) Estimator error for sensor positions in the outer die.

(d) Estimator error for sensor positions in the insertion elements .

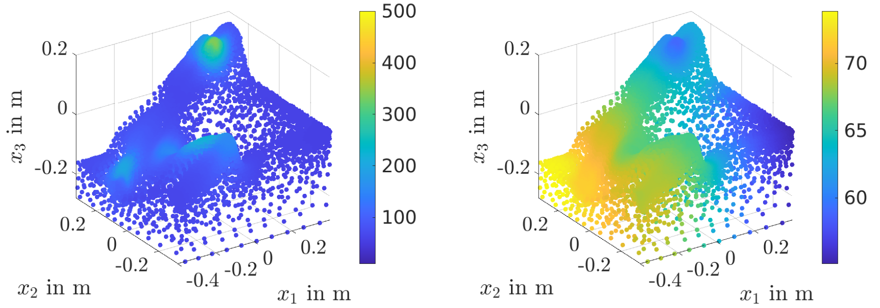

(e) Snapshot of the estimated temperature profile at $t = 100$ s.

(f) Snapshot of the estimated temperature profile at $t = 2800$ s.

Figure 6.5.: Temperature evolutions, estimator errors and snapshots for the scenario with zero input $\boldsymbol{u} = \mathbf{0}$. The vertical magenta dotted line again marks the point, where the punch reaches the bottom dead point during the forming step.

6.3. Controller Validation

For closed control loop first the LQ regulator with integral part from Section 5.2 is validated followed by the PD controller from Section 5.3.

6.3.1. LQ Control

The controller presented in Section 5.2 is experimentally validated. Starting with a non-steady state profile the state feedback (5.7) is evaluated using the estimated states obtained from the Kalman filter (5.6). While the latter is again tuned with the identity matrices Q and R, the LQ controller is tuned with an identity matrix Q_c and a diagonal matrix R_c with

$$\operatorname{diag} R_c = [1.8, 1.45, 1.2, 1.05, 1.4, 1.25]^T 10^6.$$

The reference trajectory is assigned constant with

$$\boldsymbol{r}(t) = [130, 130, 130, 130, 130, 130]^T \,{}^\circ\mathrm{C}$$

to reach the demanded temperature of 150 °C in the target zones for $T_\infty = 20\,^\circ\mathrm{C}$. This ambient temperature is again subtracted from the output $\boldsymbol{y}$ as (3.5) still holds true. The considered scenario includes two forming steps, which are performed at times $t = 730$ s and $t = 1134$ s. In both cases the punch again needs 20 s to reach the bottom dead center and stays there for 30 s. At times $t = 780$ s and $t = 1184$ s the punch starts moving upwards to its upper dead center.

The obtained results are summarized in Fig. 6.6. The vertical magenta dotted line again marks the point, where the punch reaches the bottom dead point during the forming step. The temperature at the sensors in the die rises approximately linearly (Fig. 6.6(a)), while the sensors in the insertion elements all reach a nearly constant temperature after about $t = 500$ s except during forming, see Fig. 6.6(b). Starting when the die is at the bottom dead center during the forming steps, it takes about 120 s until the sensors in the insertion elements reach the temperature level before forming. This is a significant improvement towards the heat-up case in Fig. 6.4, where it takes about 300 s. Fig. 6.6(c) shows the input vector $\boldsymbol{u}$ and Fig. 6.6(d) the target output $\boldsymbol{y}_{\mathrm{targ}}$. The input is nearly constant after about 500 s but is rising to maximum power when the forming operations take place. The values are nearly proportional to the input (6.1), which guarantees the desired temperature profile in the steady state. As the steady state is not completely reached the inputs are higher by a factor of about 1.5. The reached target outputs are slightly larger than the desired 150 °C. This might be due to the rising input power during the forming steps. However, as the target temperatures almost never fall below the reference the formability of the metal during the forming process is guaranteed.

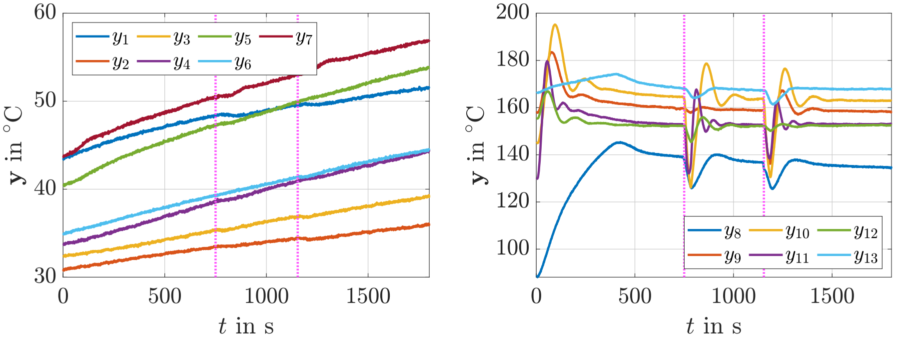

(a) Temperature evolution in the outer die.

(b) Temperature evolution in the insertion elements.

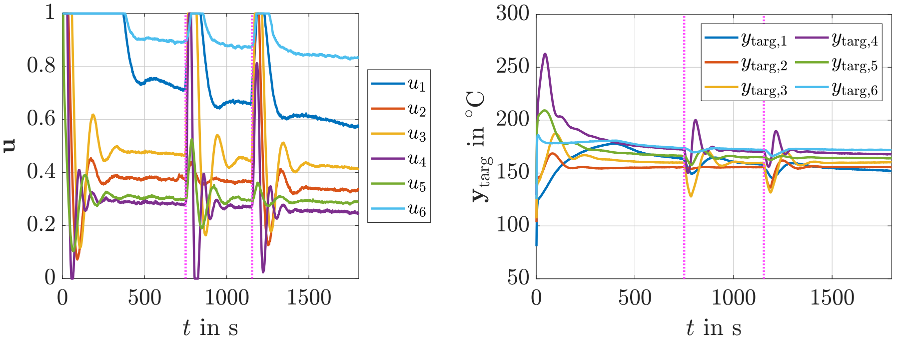

(c) Applied control inputs.

(d) Target outputs.

Figure 6.6.: Temperature evolutions, applied control inputs and target output for the LQ-regulator with integral part. The vertical magenta dotted line again marks the point, where the punch reaches the bottom dead point during the forming step.

6.3.2. PD Control

The controller presented in Section 5.3 is experimentally validated, starting with a non-steady state profile. The steady state input is set to

$$\boldsymbol{u}^s = [0.2489, 0.2699, 0.2865, 0.1641, 0.2191, 0.6315]^T,$$

which corresponds to a target temperature profile of $\boldsymbol{y}^s_{\mathrm{targ}} = 130 \times \mathbf{1}\,°\mathrm{C}$ inside the target zones. Due to the mapping (3.5) with an ambient temperature of $T_\infty = 20\,°\mathrm{C}$ this equals a temperature of 150 °C. The target output values are calculated via (5.8) as

$$\boldsymbol{y}^s_{8:13} = [141.15, 151.77, 151.44, 142.05, 142.84, 147.32]^T.$$

The ambient temperature is again subtracted from the output $\boldsymbol{y}$. The controller parameters $K_p = 0.01$ and $K_d = 0.005$ are chosen. The considered scenario includes two forming steps, which are performed at times $t = 396$ s and $t = 474$ s. The first one is performed without blank. Here, the temperature decrease from the punch should be evaluated. In both cases the punch again needs 20 s to reach the bottom dead center and stays there for 30 s. At times $t = 446$ s and $t = 524$ s the punch starts moving upwards to its upper dead center.

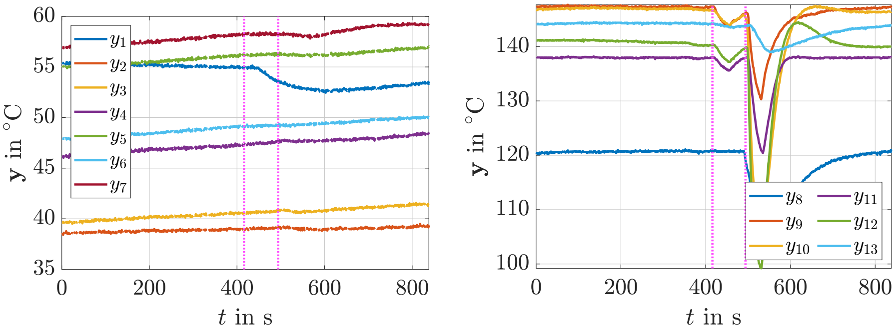

(a) Temperature evolution in the outer die.

(b) Temperature evolution in the insertion elements.

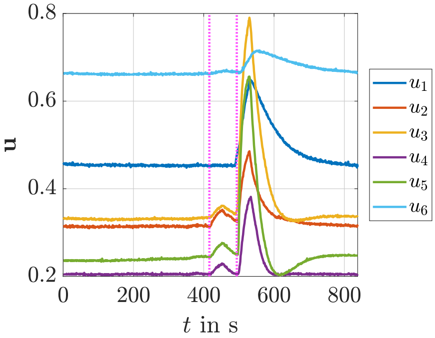

(c) Applied control inputs.

Figure 6.7.: Trajectory planning for the die.

The obtained results are summarized in Fig. 6.7. The temperature at the sensors in the die rises approximately linearly (Fig. 6.7(a)), while the sensors in the insertion elements all reach a nearly constant temperature except during forming, see Fig. 6.7(b). The forming step without blank only leads to a negligibly small temperature decrease. Starting when the die is at the bottom dead center during the forming step with blank, it takes about 120 s until the sensors in the insertion elements reach the temperature level before forming. This is comparable to the LQ regulator with integral part. Fig. 6.7(c) shows the input vector $\boldsymbol{u}$, which is nearly constant but is rising to higher power when the forming operations take place.

This controller operates model free, which leads to the disadvantage of missing information about the temperature in the target zones. With the chosen $\boldsymbol{y}^s_{8:13}$ these should have the desired values in the steady state, but since it is not reached, the desired values in the target zones cannot be guaranteed. For the process, which is not operating in a steady-state the LQ regulator with integral part is the better choice. In steady state this conclusion may be questioned. The PD controller has a much less computation time, which would allow lower sample times Δt, however the LQ regulator might be more reliable, if disturbances arise. It furthermore gives useful information about the temperature distribution in the whole die.

The obtained experimental results clearly support the applicability of this consistent design process and confirm the control and estimation performance to maintain desired prescribed local target temperatures during forming. It is also shown that in a scenario with multiple consecutive forming steps the demanded temperature can be kept at the demanded level. Further evaluations and possible improvements of the presented approach in future research are made in Chapter 12 and 13 of Part III.

Part II.

Data-Based Control of a Multistage Press Hardening Process

7. Multistage Press Hardening Process

In the introductory Chapter 1 the press hardening of sheet metals in multistage dies was motivated. Besides the advantages like the production of geometrically complex, hardened components in large batch sizes, there are some challenges. These include the difficult prediction of product properties due to a multistage error propagation and an extended perturbation collective. To compensate for the uncertainties and thus to implement a robust and adaptable production, forming processes can be operated in a closed control loop [1].

The implementation of a comprehensive property control is the overall objective for the multistage press hardening process. The aim is to control the product properties based on the microstructure such as the distribution of hardness and the sheet thinning, while simultaneously maintaining a desired product geometry during a multistage press hardening process. For developing such a multivariable closed-loop control, multistage press hardening in a progressive die operated in a servo press having the stage sequence presented in Fig. 7.1 is considered. The material used for this forming process is the press hardening steel 22MnB5, with its microstructure evolution having a pronounced sensitivity towards the thermo-mechanical treatment during the multistage process. When this steel is quenched after austenitizing at cooling rates greater than the critical cooling rate $r_{c,crit}$, the final microstructure of the selected material becomes almost completely martensitic. At lower cooling rates ($r_c < r_{c,crit}$) a mixed microstructure with lower hardness is formed. Furthermore, the critical cooling rate for achieving a martensitic microstructure increases with strain imposed by forming the 22MnB5 sheet material in the austenitic state. The material to be processed with the progressive die having initially a ferritic-pearlitic microstructure is in the form of slit strip with a sheet thickness $s = 2\,\text{mm}$ and a strip width of 200 mm.

7.1. Stages and Steps

Fig. 7.1 gives an overview of the relevant stages in the underlying press hardening process. While Fig. 7.1(a) gives an schematic overview, Fig. 7.1(b) shows the experimental stages and Fig. 7.1(c) the respective products. During preliminary stages (not shown in Fig. 7.1) the slit strip is precut at room temperature into rectangular blanks with a width of 60 mm and a length of 140 mm. They are linked to each other by a strip connection for the transfer through the tool stages. In the first control-relevant die stage, the precut rectangular blanks are heated to the austenitizing temperature T_γ by an induction coil. In the tempering stage, a temperature profile is set along the longitudinal direction of the blank using resistance heating in one area of the

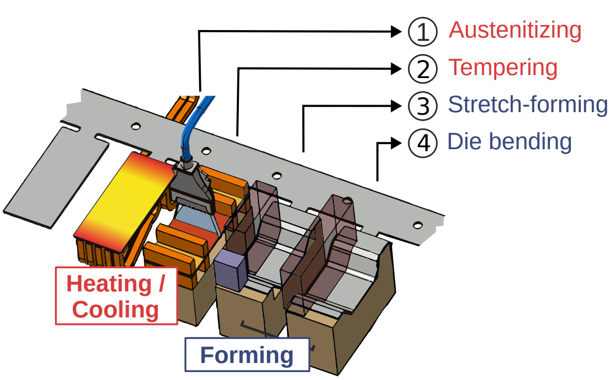

(a) Schematics of the stages from the multistage press hardening process (according to [46]).

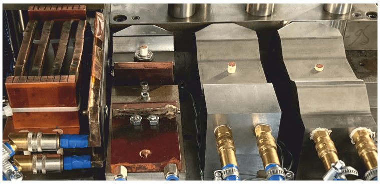

(b) The experimental stages.

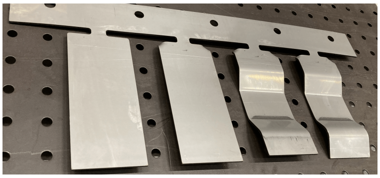

(c) The respective product blanks.

Figure 7.1.: Schematics of the stages from the multistage press hardening process, the experimental stages and the respective product.

blank and cooling with compressed air from flat fan nozzles in another one. Hereby it is aimed to tailor the phase transformation by the temperature-dependent flow of the material in the subsequent forming stages as well as the thermal history. In the stretch-forming stage, a hat shaped profile is formed. Finally, during die bending, a side wall of the previously formed hat shaped profile is bent and the final geometry is calibrated by completing the quenching in the closed die.

Each stage consists of six transitioning steps. The first step involves transferring the blank from one stage to another. In the middle of this stage, the press reaches its top dead center (TDC) placing the blank in its highest position. This is followed by the closing of the tools with no prior contact between the tools and the blank. The next step involves the actual forming of the blank. The subsequent holding step is the longest and reaches the bottom dead center (BDC) of the press. During this stage, the blank undergoes heating or cooling in two temperature stages and its obtained geometry solidifies in the forming stages. This step is particularly relevant for control purposes. Afterward, the demolding of the blank takes place, followed by the final step, which is the opening of the tools without contacting the blank. The simulated temperature and geometry development throughout these steps and stages is described in Section 8.1.

The duration of a stage depends on some parameters: The stroke rate f_{SR} relates to the press velocity and is described more detailed in Section 7.2. The contact ratio $\xi = 0.75$ refers to the percentage of the duration of a stage, in which the press in the BDC. The percentages $p_{\mathrm{Tr}} = \frac{4}{7}$, $p_{\mathrm{Cl}} = \frac{1}{7}$, $p_{\mathrm{Fo}} = \frac{2}{7}$ define the temporal relations between the transfer, closing and forming steps. The duration of a whole stage is

$$\tau_{\mathrm{cyc}} = \frac{1}{f_s},$$

and the durations of the transfer, closing, forming, holding, demould and opening steps are given by

$$\tau_{\mathrm{Tr}} = p_{\mathrm{Tr}}\tau_{\mathrm{cyc}}\frac{1-\xi}{2}, \quad \tau_{\mathrm{Cl}} = p_{\mathrm{Cl}}\tau_{\mathrm{cyc}}\frac{1-\xi}{2}, \quad \tau_{\mathrm{Fo}} = p_{\mathrm{Fo}}\tau_{\mathrm{cyc}}\frac{1-\xi}{2},$$
$$\tau_{\mathrm{Ho}} = \tau_{\mathrm{cyc}}\xi, \quad \tau_{\mathrm{De}} = \tau_{\mathrm{Fo}}, \quad \tau_{\mathrm{Op}} = \tau_{\mathrm{Cl}}.$$

Exemplarily, for a stroke rate $f_{\mathrm{SR}} = 6\,\mathrm{min}^{-1}$ the duration of a cycle is $\tau_{\mathrm{cyc}} = \frac{60\,\mathrm{s\,min}^{-1}}{6\,\mathrm{min}^{-1}} = 10\,\mathrm{s}$. With the above formulas the step durations are $\tau_{\mathrm{Tr}} \approx 0.71\,\mathrm{s}$, $\tau_{\mathrm{Cl}} = \tau_{\mathrm{Op}} \approx 0.18\,\mathrm{s}$, $\tau_{\mathrm{Fo}} = \tau_{\mathrm{De}} \approx 0.36\,\mathrm{s}$ and $\tau_{\mathrm{Ho}} = 7.5\,\mathrm{s}$.

7.2. Control Variables

The process has five control variables, which are schematically shown in Fig. 7.2. The stroke rate f_{SR} is related to the velocity of the press. It effects all four process stages. By adjusting the stroke rate f_{SR} of the press, the contact time of the tools with the hot sheet can be adjusted, which allows to vary the average cooling rate during the multistage process. The influence of the stroke rate f_{SR} concerning the time between TDC and BDC is visualized in Fig. 7.2(a). The blankholder force F_{BH} can be adjusted during stretch-forming, which allows the sheet draw-in E and thus also the sheet thinning Δs to be set. Hereby, Fig. 7.2(b) depicts the influence of F_{BH} during the third stage and Fig. 7.2(c) the resulting geometry defined by E, Δs and the bending angle α. As already elaborated in Section 7.1 a uniform temperature T_γ can be set in the first stage by an induction coil and a temperature profile along the longitudinal direction of the blank can be adjusted in the second stage. Here, one area of the blank is heated to temperature T_{Heat} using resistance heating and another area is cooled with compressed air from flat fan nozzles with an air pressure p_{Air}. The influence of the control variables T_γ, T_{Heat} and p_{Air} is visualized in Fig. 7.2(d).

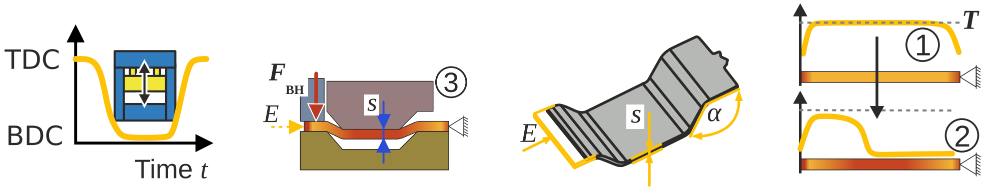

(a) Impact of control variable f_{SR}.

(b) Impact of control variable F_{BH}.

(c) Resulting product geometry.

(d) Impacts of control variables T_γ, T_{Heat}, and p_{Air}.

Figure 7.2.: Impacts of control variables f_{SR}, F_{BH}, T_γ, T_{Heat}, and p_{Air} and the resulting product geometry (according to [46]).

A multivariable control, in this case the simultaneous control of different product properties and the geometry needs multiple control variables, so that the target properties can be set in a decoupled manner via the available degrees of freedom. The decoupling of actuators in this multistage press hardening process is discussed more detailed in [47, 70]. In these publications, the potential for tailoring the hardness by gradually adapting the thermo-mechanical history throughout the process has also been demonstrated.

7.3. Property Control Loop

The overall objective is to control the product properties based on the microstructure, while simultaneously maintaining a desired product geometry during a multistage press hardening process, as depicted in Fig. 7.3 The relevant properties are the sheet thinning Δs and the hardness H. For a reconstruction of the product properties with a soft sensor cascade the temperature is measured locally with four spring loaded thermocouples installed in the die stages and two pyrometers, while the ram is near the BDC. In addition, the temperature distribution is observed with a thermal imaging camera. This instrument is only used for model and sensor validation, since the temperature can only be measured, while the ram is near the TDC. Based on these measurements, the spatial-temporal temperature distribution is determined using the estimator developed in Chapter 9 utilizing the DMD model derived in Chapter 8. This distribution provides the baseline for calculating the plasticity and thus the geometry using suitable gray-box models and predicting the hardness H and sheet thinning Δs by an artificial neuronal network, see [46]. The resulting values are then compared with the target value to adjust the input variables f_{SR}, F_{BH}, T_γ, T_{Heat} and p_{Air} accordingly.

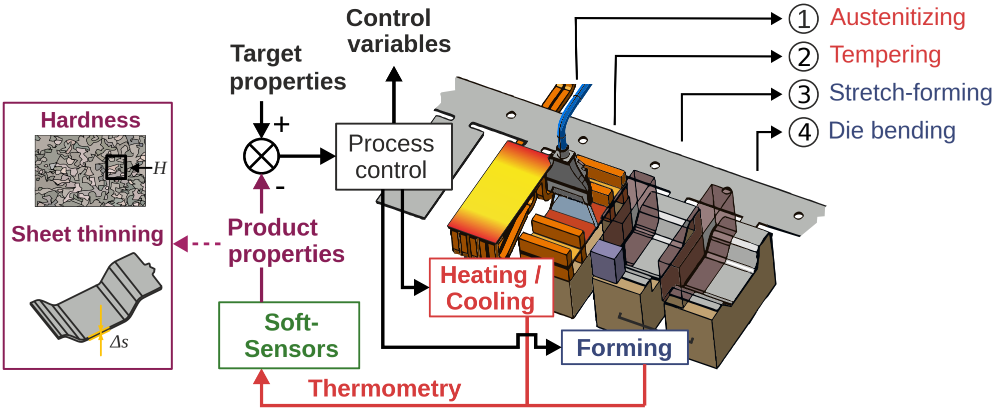

Figure 7.3.: Schematics of the control loop of the multistage press hardening process (according to [46]).

8. Data-Based Modeling and Parameter Identification

In this chapter a mathematical model for the evolution of the temperature distribution in the blank is derived. First a high fidelity model is determined to describe the temperature distribution $T_{\mathrm{Sim}}(x,t)$ in the sheet during the tool stages of the progressive die. A dynamic mode decomposition (DMD) is performed using snapshot matrices of the system solution in order to get a data-based model with reduced system order. This is extended by a parametric DMD to include temperature developments with different control variable configurations. Using experimental data an identification of the process parameters is performed and the DMD algorithm is supplemented by a regularization term.

8.1. High Fidelity Model

To determine the temperature distribution $T_{\mathrm{Sim}}(x,t)$ in the sheet during the tool stages of the progressive die, the multistage process is simulated with the FE code `LSDyna` (solver: R12.0.0). The basic structure for modeling each of the process stages follows the setup described in [30]. Heat exchange between sheet, tools and the environment as well as the flow stress and Young's modulus of the 22MnB5 sheet material are modeled with values based on [67]. The tools are meshed with rigid and the blank with elasto-viscoplastic 12 node thermal thick shells, whereby the heat flow in the sheet thickness direction can be accounted for. The meshed blank is shown in Fig. 8.1. The spatial positions of the nodes change over time as seen in the difference between the start of the forming process in Fig. 8.1(a) and the end in Fig. 8.1(b). Gray nodes serve as positions for fixture elements and are not relevant for the forming process. The red and green nodes are relevant to the forming process. For reasons of simplicity only the temperatures of the green nodes are later evaluated for the reduced system as the temperatures do not change significantly in x_1-direction.

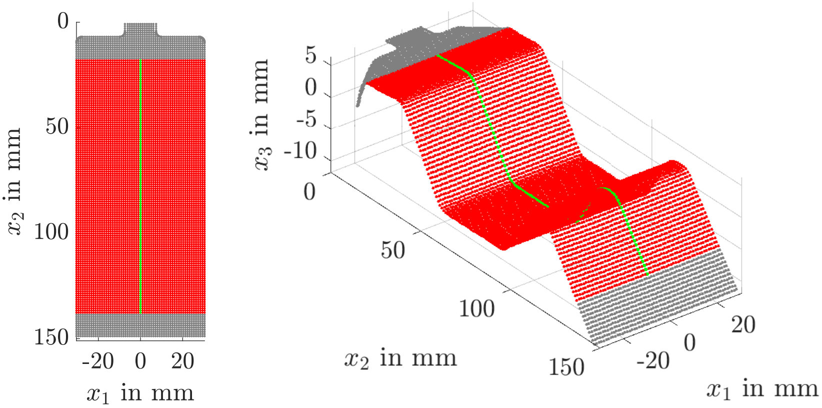

(a) 2D-Mesh at the start of the forming process.

(b) 3D-Mesh at the end of the forming process.

Figure 8.1.: Blank mesh evolution during the forming process.

The microstructure evolution governed by the diffusionless phase transformation from austenite to martensite and the phase transformation by diffusion from austenite to bainite, ferrite or pearlite is modeled with the material model Mat248 based on [28]. A strain dependent scaling of the activation energy for phase transformation is used to cover the effect of forming the 22MnB5 in the austenitic state on microstructure evolution as proposed by [5]. The inductive heating of the blank in the austenitizing stage is not simulated. Before the transfer to the tempering stage, a fully austenitized blank with a defined temperature distribution is assumed. Also, the resistance heating as well as the cooling by compressed air in the tempering stage is taken into account in a simplified way by a thermal boundary condition imposed on the nodes of the sheet.

In order to describe the temperature and geometry development in the blank simulated via this FE approximation, snapshots at the end of every step in the three relevant stages are depicted in Fig. 8.2, 8.3 and 8.4. The simulation is calculated for $T_\gamma = 1050\,°\mathrm{C}$, $T_{\mathrm{Heat}} = 1000\,°\mathrm{C}$, $f_{\mathrm{SR}} = 6\,\mathrm{min}^{-1}$ and $F_{\mathrm{BH}} = 20\,\mathrm{kN}$. The influence of p_{Air} is treated in the mentioned simplified way, with an end temperature in area A_1 during the tempering stage of 900 °C.

Fig. 8.2 visualizes snapshots of the temperature distribution and the underlying geometry in the blank gained from the FE simulation at the end of each step in the tempering stage. First the transfer between the austenitizing and the tempering stage is simulated in Fig. 8.2(a). There is no contact between tools and the blank, which is at its highest x_3-position during the process. The blank has a temperature slightly lower then T_γ. This simulated heat loss is due to the convection and radiation to the environmental air. In the upper and lower areas, the temperature is much lower due to the contact with fixture elements. After the closing step the blank has a lower x_3-position. This is shown in Fig. 8.2(b). The temperature remains nearly the same. The forming step is visualized in Fig. 8.2(c). During the tempering stage no forming action takes place, with

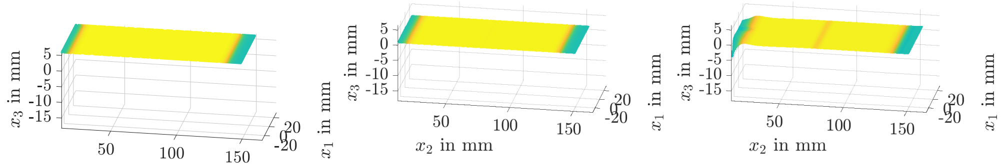

(a) Transfer step.

(b) Closing step.

(c) Forming step.

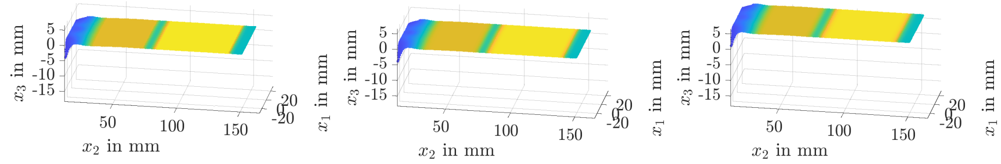

(d) Holding step.

(e) Demould step.

(f) Opening step.

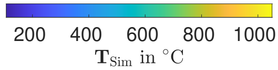

Figure 8.2.: Snapshots of the temperature distribution in the blank gained from the FE simulation at the end of each step in the tempering stage.

the exception of the part connected with the strip connection in minimum x_2-direction, which is not relevant for control. Instead the blank gets into contact with the DC resistance heating in the maximum positions of area A_2 in both x_2-directions. Here, the main heat loss is due to this contact. During the holding step in Fig. 8.2(d) the blank is cooled with air pressure in area A_1 and heated with resistance heating in area A_2. Between these areas a colder middle part growths up due to the contact with fixture elements of the DC resistance heating. The short demould step is depicted in Fig. 8.2(e). Here the temperature development and forming of the blank do not change significantly. The opening step increases the x_3-position to the level of the transfer step. There is no contact between tools and blank. This step is shown in Fig. 8.2(f).

Fig. 8.3 visualizes snapshots in the stretch-forming stage. The transfer from tempering to stretch-forming stage is shown in Fig. 8.3(a). The position and the temperature distribution do not change significantly towards the opening step of the tempering stage. After the closing step the blank again has a lower x_3-position. This is shown in Fig. 8.3(b). The temperature distribution nearly stays constant. The forming step is visualized in Fig. 8.3(c). Here, a hat shaped profile is formed. The temperature distribution does not change in a huge amount due to the short duration of the step. The geometry of the blank does not change during the holding step in Fig. 8.3(d) since the die and punch are still in their previous positions. The temperature reduces

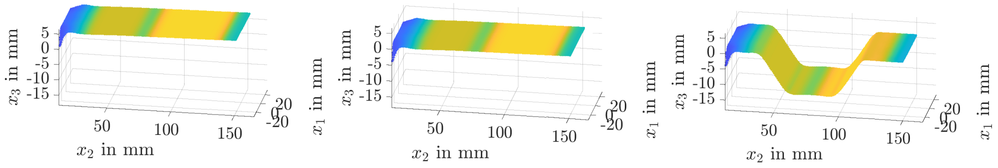

(a) Transfer step.

(b) Closing step.

(c) Forming step.

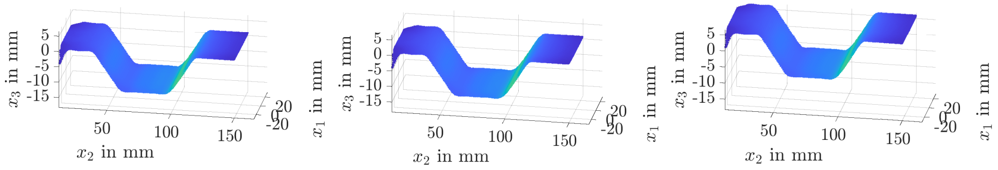

(d) Holding step.

(e) Demould step.

(f) Opening step.

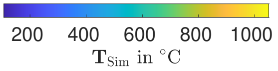

Figure 8.3.: Snapshots of the temperature distribution in the blank gained from the FE simulation at the end of each step in the stretch-forming stage.

significantly in the whole blank due to the contact with the tools. The short demould step is depicted in Fig. 8.3(e). Here, again the temperature development and forming of the blank almost remain constant. The opening step increases the x_3-position to the level of the transfer step. There is no contact between tools and blank. This step is shown in Fig. 8.3(f).

Fig. 8.4 depicts snapshots in the die bending stage. These behave in a similar way as in the previous stage since it is also a forming stage. The transfer from stretch-forming to die bending stage is shown in Fig. 8.4(a). After the closing step the blank again has a lower x_3-position, as shown in Fig. 8.4(b). The forming step is visualized in Fig. 8.4(c). Here, a side wall of the previously formed hat shaped profile is bent. During the holding step in Fig. 8.4(d) the geometry stays constant and the temperatures reduce enormously. The short demould step is depicted in Fig. 8.4(e) without significant changes. The opening step increases the x_3-position to the level of the transfer step. This step is shown in Fig. 8.4(f).

In the previous descriptions two different areas in the tempering stage were named. These are characterized more detailed in Fig. 8.5. The mesh from the unformed blank is shown in Fig. 8.5(d). Here, the dark gray parts are used for fixture elements and are not control relevant. Area A_1 is marked in blue. Here, the blank is cooled with compressed air in the tempering stage. The

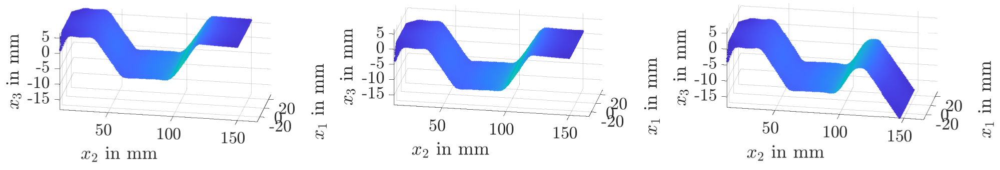

(a) Transfer step.

(b) Closing step.

(c) Forming step.

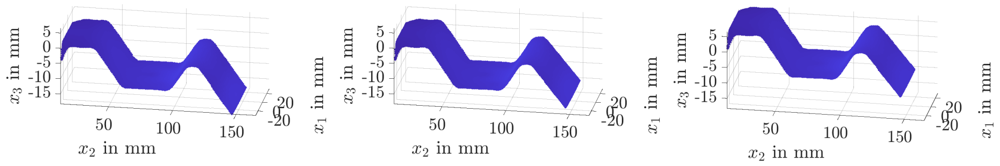

(d) Holding step.

(e) Demould step.

(f) Opening step.

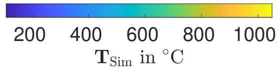

Figure 8.4.: Snapshots of the temperature distribution in the blank gained from the FE simulation at the end of each step in the die bending stage.

temperature development at the nodes in this area over the three simulated stages is shown in Fig. 8.5(a). It is nearly equal at all nodes in the tempering stage and begins to differ with the forming operations. Area A_2 is marked red. Here, the blank is heated with a resistance heating generator in the tempering stage. The temperature development at the nodes in this area over the three simulated stages is shown in Fig. 8.5(a). Because of the implemented and simulated PID control, which is described in more detail in Chapter 10, the temperature is constant just after the begin of the holding step. Due to the higher temperature level the nodes differs more significantly in the two forming stages. The light gray areas are later used for control purposes, but also have some contact to the tools. That is why the temperature development, depicted in Fig. 8.5(c), has higher cooling rates in the tempering stage.

8.2. Data-Based Reduced Order Modeling

A dynamic mode decomposition (DMD) is performed using snapshot matrices of the FE simulation in the previous section to get a data-based model with reduced system order. This is later

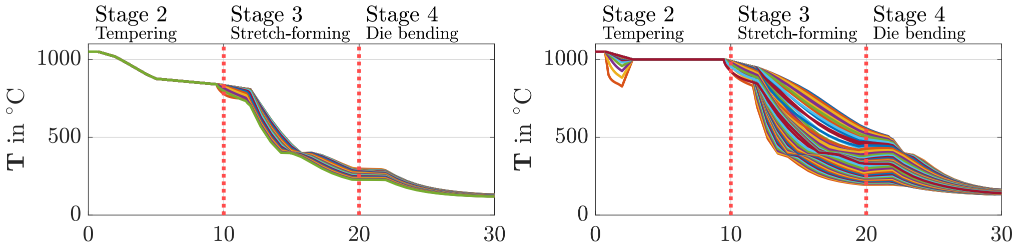

(a) Temperature development in area A_1.

(b) Temperature development in area A_2.

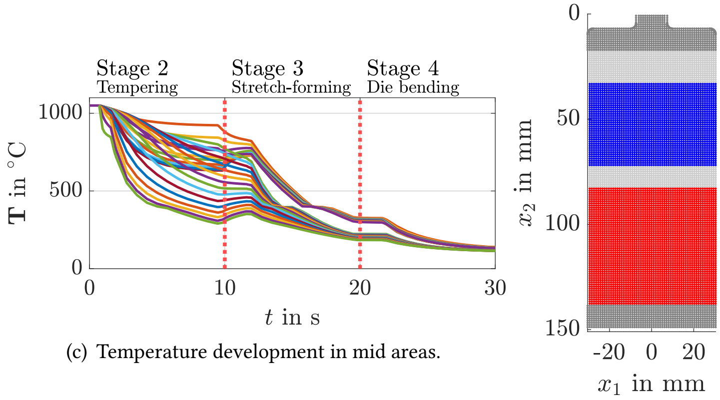

(c) Temperature development in mid areas.

(d) Mesh.

Figure 8.5.: Temperature development in the areas and the mesh with blue marked cooling area A_1, red marked heating area A_2, light gray marked mid areas and dark gray areas for fixture elements.

extended by a parametric DMD to include temperature developments with different control variable configurations.

8.2.1. Dynamic Mode Decomposition

The DMD is a model order reduction (MOR) technique to isolate spatially coherent modes each associated with a fixed frequency [40]. DMD provides not only modes, but also enables to determine a linear model for the temporal evolution of the modes. The actual evaluation makes use of either measured or simulated data summarized in the data vector $\boldsymbol{T}_{\text{Sim}}(t_k)$ collected at discrete times $t_k = (k-1)\Delta t$, $k = 0, 1, \dots m-1$. In the considered scenario $\boldsymbol{T}_{\text{Sim}}(t_k)$, $k = 0, 1, \dots m-1$ denote the sampled temperatures obtained from the detailed `LSDyna` simulation at all $n = 119$ relevant (green marked) nodes of the sheet metal (cf. Fig. 8.1) passing the three consecutive processing stages 2, 3 and 4 of Fig. 7.1. Hence, a Lagrangian perspective is taken. Fig. 8.6 shows the time evolution of $\boldsymbol{T}_{\text{Sim}}$.

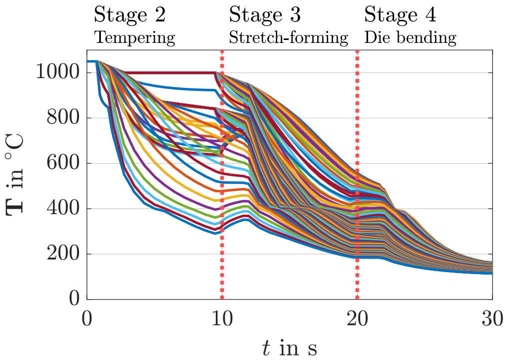

Figure 8.6.: Temperature evolution over the 3 simulated stages.

Let

$$\begin{aligned} X_1 &= \begin{bmatrix} \boldsymbol{T}_{\text{Sim}}(t_0) & \boldsymbol{T}_{\text{Sim}}(t_1) & \dots & \boldsymbol{T}_{\text{Sim}}(t_{m-2}) \end{bmatrix} \in \mathbb{R}^{n\times(m-1)} \\ X_2 &= \begin{bmatrix} \boldsymbol{T}_{\text{Sim}}(t_1) & \boldsymbol{T}_{\text{Sim}}(t_2) & \dots & \boldsymbol{T}_{\text{Sim}}(t_{m-1}) \end{bmatrix} \in \mathbb{R}^{n\times(m-1)} \end{aligned}$$

denote the snapshot matrices. The number of time steps $m = t_e/\Delta t$ depend on the process time t_e and the sampling time Δt. DMD starts from the assumption that $\boldsymbol{T}_{\text{Sim}}(t_k)$ and $\boldsymbol{T}_{\text{Sim}}(t_{k+1})$ are approximately related by a linear operator $A \in \mathbb{R}^{n\times n}$ according to $\boldsymbol{T}(t_{k+1}) \approx A\boldsymbol{T}(t_k)$ with the DMD state vector $\boldsymbol{T}(t_k)$. In view of the snapshot matrices this is equivalent to $X_2 \approx AX_1$. A least-squares solution A is obtained by minimizing the Frobenius norm of $\|X_2 - AX_1\|$, which yields $A = X_2X_1^\dagger$ with $X_1^\dagger$ the pseudoinverse of X_1. The singular value decomposition (SVD) provides an efficient way to compute $X_1^\dagger$. Moreover, this also allows to determine a reduced order representation A_r of A. The rank-r truncated DMD is computed as follows.

1. For X_1 the rank-r truncated SVD

$$X_1 \approx U_r S_r V_r^* \tag{8.1}$$

   with $U_r \in \mathbb{C}^{n\times r}$, $S_r \in \mathbb{C}^{r\times r}$ and $V_r \in \mathbb{C}^{(m-1)\times r}$ is evaluated, where $\cdot^*$ denotes the complex conjugate transpose.

2. The matrix A can be determined from the SVD using

$$A = X_2X_1^\dagger \approx X_2V_rS_r^{-1}U_r^* = \bar{A}.$$

   Hence, $\boldsymbol{T}(t_{k+1}) = \bar{A}\boldsymbol{T}(t_k)$ is obtained to approximate the evolution of the data (state) vectors. To reduce the system order, the linear transformation $\boldsymbol{T}_r(\cdot) = U_r^*\boldsymbol{T}(\cdot)$ and thus $\boldsymbol{T}(\cdot) \approx U_r\boldsymbol{T}_r(\cdot)$ with $\boldsymbol{T}_r \in \mathbb{R}^r$ for $r \ll n$ is introduced to obtain

$$\boldsymbol{T}_r(t_{k+1}) = A_r\boldsymbol{T}_r(t_k) \tag{8.2}$$

   with $A_r = U_r^*\bar{A}U_r = U_r^*X_2V_rS_r^{-1}$.

3. The eigendecomposition of A_r is computed from $A_r W = W\Lambda$. The eigenvalues of $\bar{A}$ are summarized in the diagonal matrix Λ and the related eigenvectors, the DMD modes, are given by the columns of $\Phi = X_2 V_r S^{-1} W$.

The approximate solution of (8.2) for time t is given by

$$\boldsymbol{T}(t_k) \approx \Phi\Lambda^k \boldsymbol{b} \tag{8.3}$$

with the DMD modes Φ and the diagonal matrix Λ with eigenvalues λ_k. The vector $\boldsymbol{b} = \Phi^\dagger \boldsymbol{T}(t_0)$ is calculated using the initial condition $\boldsymbol{T}(t_0) = \Phi\boldsymbol{b}$.

The sampling time $\Delta t = 0.01$ s and truncation order $r = 50$ are chosen to ensure the numerical stability of the reduced order system, see, e.g., [42]. The results depicted in Fig. 8.7 are achieved by simulating the approximate solution (8.3). The blue line shows the evolution of the mean temperature $\text{mean}(\boldsymbol{T}) = \sum_{i=1}^{n} T_i/n$ over time. The colored bars visualize the difference between the DMD model and the corresponding `LSDyna` simulation $\Delta\boldsymbol{T} = \|\boldsymbol{T} - \boldsymbol{T}_{\text{Sim}}\|_1$. The gray bars show the maximum difference denoted by $\max(\Delta\boldsymbol{T})$ at a node and the red bars visualize the mean difference $\text{mean}(\Delta\boldsymbol{T}) = \sum_{i=1}^{n} \Delta T_i/n$ over all nodes. It becomes apparent that the difference $\Delta\boldsymbol{T}$ between DMD and full model is small with slightly larger values at the transition point between two stages. In particular, the average difference over all nodes takes a maximum value of 10 °C at the stage transitions and the maximum difference of all nodes behaves in a similar way with higher values of up to 60 °C.

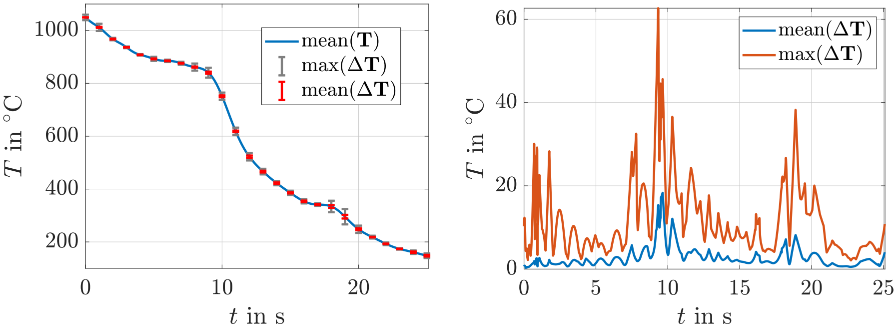

Figure 8.7.: Comparison of temperature evolution between the solution (8.3) of the reduced order DMD model (8.2) and the full order `LSDyna` simulation.

In view of the real-time application of the reduced order model for state estimation the respective simulation times are relevant: the simulation of the process using the `LSDyna` model takes 15-20 h while the DMD model requires 70 ms.

The considered multistage press hardening process is characterized by operator-defined control variables such as stroke rate f_{SR} that can be changed only at certain operating times but not continuously over time, which is why they cannot be simulated as input variables $\boldsymbol{u}$ in combination with an input matrix B. However, they have to be included into the modeling concept.

8.2.2. Parametric DMD

A parametric DMD method is the stacked DMD algorithm [63, 33]. This approach is very similar to the non-parametric DMD, except that the time series solutions for different parameter values are "stacked" to form augmented snapshot matrices $X_{1,\boldsymbol{\mu}}$ and $X_{2,\boldsymbol{\mu}}$ in (8.4) containing the vertically stacked time series for $N = 7$ parameter realizations $\boldsymbol{\mu} = [\mu_1, \mu_2, \ldots, \mu_N]^T$, which are different settings for the multistage forming process. The stacked matrices are

$$X_{1,\boldsymbol{\mu}} = \begin{bmatrix} X_{1,\mu_1} \\ X_{1,\mu_2} \\ \vdots \\ X_{1,\mu_N} \end{bmatrix}, \; X_{2,\boldsymbol{\mu}} = \begin{bmatrix} X_{2,\mu_1} \\ X_{2,\mu_2} \\ \vdots \\ X_{2,\mu_N} \end{bmatrix}, \; \Phi_{\boldsymbol{\mu}} = \begin{bmatrix} \Phi_{\mu_1} \\ \Phi_{\mu_2} \\ \vdots \\ \Phi_{\mu_N} \end{bmatrix}. \tag{8.4}$$

The realizations, summarized in Table 8.1, vary in the process or control variables, respectively, given by the stroke rate f_{SR}, blank holder force F_{BH}, and austenitization temperature T_γ. These are subsequently summarized in the tuple $\theta = (f_{\mathrm{SR}}, F_{\mathrm{BH}}, T_\gamma)$, whose elements are supposed to fulfill $6\,\mathrm{min}^{-1} \leq f_{\mathrm{SR}} \leq 8\,\mathrm{min}^{-1}$, $5\,\mathrm{kN} \leq F_{\mathrm{BH}} \leq 40\,\mathrm{kN}$, and $1000\,°\mathrm{C} \leq T_\gamma \leq 1100\,°\mathrm{C}$. Note, that the control variables T_{Heat} and p_{Air} are assumed to be only dependent from T_γ throughout this section. While $T_{\mathrm{Heat}} = T_\gamma - 50\,°\mathrm{C}$ holds, the influence of p_{Air} is treated in the mentioned simplified way, with an end temperature in A_1 during the tempering stage of $T_\gamma - 150\,°\mathrm{C}$.

i	f_{SR} in 1/min	F_{BH} in kN	T_γ in °C
1	6	20	1050
2	7	20	1050
3	8	20	1050
4	7	5	1050
5	7	40	1050
6	7	20	1000
7	7	20	1100

Table 8.1.: Parameter sets μ_i for $i = 1, \ldots, N$.

The DMD algorithm summarized before is then applied using these matrices of stacked snapshots, which provides the parametric projected DMD modes $\Phi_{\boldsymbol{\mu}}$ from (8.4). For any new parametric realization θ, the projected DMD modes $\Phi(\theta)$ are obtained from a Lagrangian interpolation between the $\Phi_{\mu,j}$, $j = 1, \ldots, N$ matrices. It is worth mentioning that other interpolation methods are also possible. For example, the use of Gaussian process regression might be an appropriate choice. The approximate solution for the temperature distribution is

$$\boldsymbol{T}(\theta, t_k) \approx \Phi(\theta)\Lambda^k \boldsymbol{b}(\theta), \tag{8.5}$$

which equals (8.3) with added parameter dependency. The different parameter configurations lead to different temperature evolutions. To compare these as results of the parametric DMD,

Fig. 8.8 shows the mean temperature mean$(\boldsymbol{T})$ over all nodes as a function of f_{SR}, F_{BH} and T_γ at the beginning $t = 0\,\mathrm{s}$ (left) and at the end $t = t_e$ (right) of the forming process.

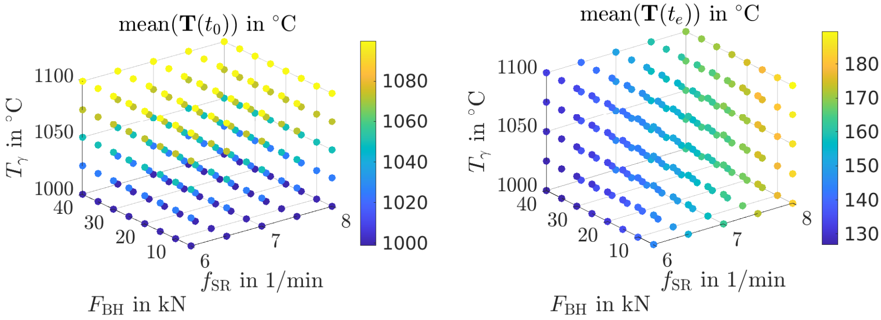

Figure 8.8.: Temperature evolutions of different parameter configurations for $t_0 = 0\,\mathrm{s}$ (left) and $t_e = 3/f_{\mathrm{SR}}$ (right).

Additionally, Fig. 8.9 provides mean temperature evolutions mean$(\boldsymbol{T}) = \sum_{i=1}^{n} T_i/n$ received from the parametric DMD for varying control parameters , i.e., five different stroke rates f_{SR} in Fig. 8.9(a). The blank holder force is set to $F_{\mathrm{BH}} = 20\,\mathrm{kN}$, and the austenitization temperature to $T_\gamma = 1050\,°\mathrm{C}$. While the temperature evolutions for $f_{\mathrm{SR}} = 6\,\mathrm{min}^{-1}$, $f_{\mathrm{SR}} = 7\,\mathrm{min}^{-1}$ and $f_{\mathrm{SR}} = 8\,\mathrm{min}^{-1}$ are obtained from the conventional DMD, $f_{\mathrm{SR}} = 6.5\,\mathrm{min}^{-1}$ and $f_{\mathrm{SR}} = 7.5\,\mathrm{min}^{-1}$ are derived by the parametric DMD using interpolation (ip.). A higher stroke rate f_{SR} speeds up the process, resulting in shorter process times t_e and higher temperatures at the end of the process. To facilitate comparison, the time is normalized using $t_N = t(f_{\mathrm{SR},h}/6\,\mathrm{min}^{-1})$. Fig. 8.9(b) shows the mean temperatures mean$(\boldsymbol{T})$ for five different blank holder forces F_{BH} with $f_{\mathrm{SR}} = 7\,\mathrm{min}^{-1}$ and $T_\gamma = 1050\,°\mathrm{C}$. $F_{\mathrm{BH}} = 5\,\mathrm{kN}$, $F_{\mathrm{BH}} = 20\,\mathrm{kN}$, and $F_{\mathrm{BH}} = 40\,\mathrm{kN}$ are derived by conventional DMD, while $F_{\mathrm{BH}} = 10\,\mathrm{kN}$ and $F_{\mathrm{BH}} = 30\,\mathrm{kN}$ are interpolated from the parameter configurations in Table 8.1. A higher blank holder force F_{BH} reduces the average temperature in the stretch-forming stage to a small degree. In the die-bending stage, this difference remains nearly constant. Five different austenitization temperatures $T_\gamma = 1000\,°\mathrm{C}$, $T_\gamma = 1050\,°\mathrm{C}$, $T_\gamma = 1100\,°\mathrm{C}$, and the interpolated $T_\gamma = 1025\,°\mathrm{C}$ and $T_\gamma = 1075\,°\mathrm{C}$ are depicted in Fig. 8.9(c). It is the only parameter that affects the starting temperature. The difference becomes smaller as the process progresses.

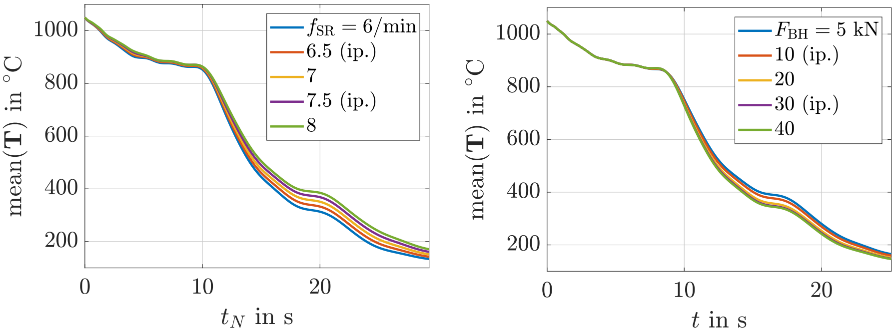

(a) Varying stroke rate f_{SR}.

(b) Varying blank holder force F_{BH}.

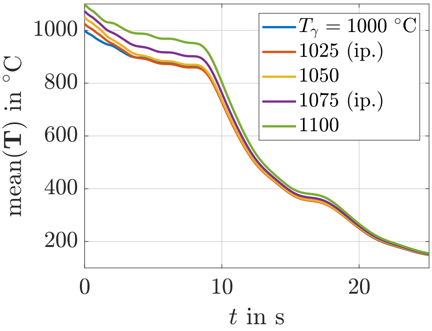

(c) Varying austenitization temperature T_γ.

Figure 8.9.: Mean temperature evolutions received from the parametric DMD for varying control parameters f_{SR}, F_{BH} and T_γ.

To evaluate the parametric DMD the resulting temperature evolution of four parameter configurations differing from the ones used for the interpolation (cf. Table 8.1) are compared with the corresponding `LSDyna` simulations. The configuration with $f_{SR} = 7.5\,\text{min}^{-1}$, $F_{BH} = 20\,\text{kN}$, and $T_\gamma = 1050\,°\text{C}$, where the stroke rate f_{SR} differs from the originally used parameter configurations, is depicted in Fig. 8.10(a). The blue line represents the mean temperature mean($\boldsymbol{T}$) simulated with the parametric DMD while gray bars visualize the maximum difference max($\Delta\boldsymbol{T}$) between the parametric DMD model and the `LSDyna` simulation at a node and the red bars visualize the mean difference mean($\Delta\boldsymbol{T}$) over all nodes. The mean difference is negligible, while the maximum difference is slightly larger especially at the two stage transitions. These results clearly confirm the functionality of the parametric DMD and its high accuracy for extremely low computational times.

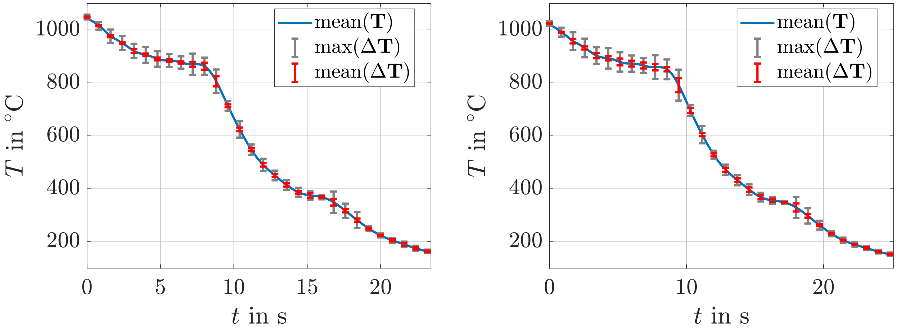

(a) $\theta = (7.5, 20, 1050)$.

(b) $\theta = (7, 20, 1025)$.

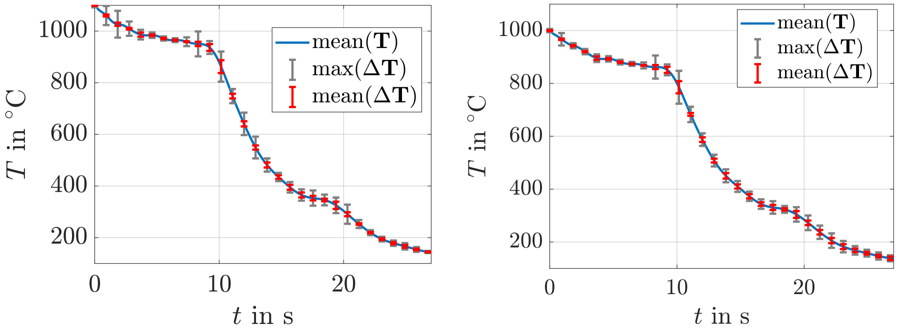

(c) $\theta = (6.5, 30, 1100)$.

(d) $\theta = (6.5, 30, 1000)$.

Figure 8.10.: Comparison of temperature evolutions obtained from parametric DMD with results from the corresponding `LSDyna` simulations for four different parameter combinations $\theta = (f_{\mathrm{SR}}$ in 1/min, F_{BH} in kN, T_γ in °C$)$.

Equally good results are obtained for the configuration $f_{\mathrm{SR}} = 7\,\mathrm{min}^{-1}$, $F_{\mathrm{BH}} = 20\,\mathrm{kN}$, and $T_\gamma = 1025\,°\mathrm{C}$, where the austenitization temperature T_γ differs from the originally used parameter configuration, see Fig. 8.10(b). Similarly, for configurations with more differing parameters the difference is small as shown for $f_{\mathrm{SR}} = 6.5\,\mathrm{min}^{-1}$, $F_{\mathrm{BH}} = 30\,\mathrm{kN}$, and $T_\gamma = 1100\,°\mathrm{C}$ in Fig. 8.10(c) and for $f_{\mathrm{SR}} = 6.5\,\mathrm{min}^{-1}$, $F_{\mathrm{BH}} = 30\,\mathrm{kN}$, and $T_\gamma = 1000\,°\mathrm{C}$ in Fig. 8.10(d).

8.3. Parameter Identification

In order to improve model accuracy this section experimentally identifies the influence of the control variable parameters. With this information the model is certainly adjusted. First the cooling rate achieved by the air pressure p_{Air} in the tempering stage is analyzed, followed by the influence of blank holder force F_{BH} concerning the temperature. Furthermore a Tikhonov regularization term is added to the model and finally the adjusted model is described.

8.3.1. Identification of the Cooling Pressure

The impact of the process parameters on the system dynamics are identified and validated with temperature measurement instruments. These are described more detailed in Section 9.1. While the model considers exact values for the austenitizing and heating temperatures T_γ and T_{Heat}, an exact value for the blank holder force F_{BH} and an exact velocity for the stroke rate f_{SR}, the influence of the cooling pressure p_{Air} of the compressed air from flat fan nozzles to the temperature is somehow unclear. As described in Section 8.1 a constant cooling rate r_c is used for modeling the influence of the cooling pressure. In the previous simulations r_c was chosen in a way that a defined end temperature is reached. To identify this value experimentally ten real tests were executed and r_c was calculated via a thermocouple measurement in the center of A_1 (see Fig. 8.5(d)) in the tempering stage. During the first four experiments the air cooling was switched off. Tests no. 5 to 8 were executed with $p_{\text{Air}} = 2\,\text{bar}$ and no. 9 and 10 with $p_{\text{Air}} = 4\,\text{bar}$. The received values for the cooling rates r_c are listed in Tab. 8.2.

The rates r_c are very similar for same values of p_{Air}, which makes the identification trustworthy. The calculated average values are $r_c = 9.76\,\text{K}\,\text{s}^{-1}$ for $p_{\text{Air}} = 0\,\text{bar}$, $r_c = 26.72\,\text{K}\,\text{s}^{-1}$ for $p_{\text{Air}} = 2\,\text{bar}$ and $r_c = 31.99\,\text{K}\,\text{s}^{-1}$ for $p_{\text{Air}} = 4\,\text{bar}$. Since the difference between the cooling rates for $p_{\text{Air}} = 2\,\text{bar}$ and $p_{\text{Air}} = 4\,\text{bar}$ is quite small the option of $p_{\text{Air}} = 4\,\text{bar}$ is neglected for control purposes. So far the cooling rate was assumed to be fully dependent on T_γ, for the further experiments with estimator and controller p_{Air} can be chosen to be either $p_{\text{Air}} = 0\,\text{bar}$ or $p_{\text{Air}} = 2\,\text{bar}$. The simulation for these cases uses the identified average cooling rates. The identification process is visualized in Fig. 8.11. The output y_1 is shown for the duration of a whole stroke for $p_{\text{Air}} = 0\,\text{bar}$ and $p_{\text{Air}} = 2\,\text{bar}$. After a transient response time of about 2 s, which is discussed in Section 9.1.2, the temperature decreases nearly constant. The green triangles show the gradients. Here, the average cooling rates are given.

p_{Air} in bar	Test No.	Cooling rate r_c in $\text{K}\,\text{s}^{-1}$	Average r_c in $\text{K}\,\text{s}^{-1}$
0	1	10.2352	9.76
	2	7.1050	
	3	10.7423	
	4	11.9881	
2	5	26.9007	26.72
	6	27.6975	
	7	25.5731	
	8	26.7322	
4	9	32.3425	31.99
	10	31.6473	

Table 8.2.: Identification of cooling pressure p_{Air}.

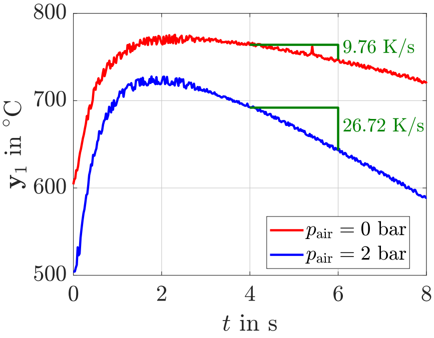

Figure 8.11.: Identification of the cooling pressure p_{Air} during the tempering stage in area 1.

8.3.2. Influence of the Blank Holder Force

The high fidelity model from Section 8.1 considers an exact value for the blank holder force F_{BH}. As visualized in Fig. 8.8 and 8.9(b) a higher force F_{BH} leads to a lower temperature $\boldsymbol{T}(t_e)$ at the end of the process. The choice of the blank holder force F_{BH} only effects the stretch-forming stage. In order to verify the influence of F_{BH} experimentally two tests were run with same control variables except from F_{BH}. Here, $F_{\mathrm{BH}} = 1\,\mathrm{kN}$ and $F_{\mathrm{BH}} = 10\,\mathrm{kN}$ were compared. While conducting the experiments, it was determined that higher forces are not feasible. The thermocouples y_2 and y_5 from Fig. 9.1 are used for comparison. The experimental results are not the same as the simulation results. While a higher F_{BH} leads to a higher cooling rate in y_5, the cooling rate at y_2 is smaller. This is shown in Fig. 8.12.

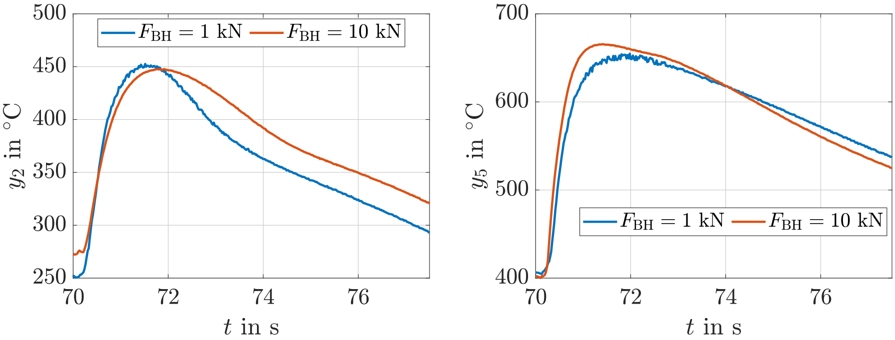

Figure 8.12.: Influence of the blank holder force F_{BH} at two different positions y_2 (left) and y_5 (right) from Fig. 9.1 during the stretch-forming stage.

As the feasible range for the force is smaller as expected, the influence of this control variable has to be reevaluated. The effect of blank holder force F_{BH} towards the temperature is quite small in the FE simulation for $F_{\mathrm{BH}} \leq 10\,\mathrm{kN}$. Additionally, the experiments cannot verify this small effect.

Finally, the blank holder force F_{BH} can be neglected as a parameter for temperature control purposes. This finding is also confirmed in the experimental validation in Section 11.2.1.

8.3.3. Regularization

So far the influence of blank holder force F_{BH} and cooling pressure p_{Air} are identified. While p_{Air} becomes a new parameter to include in the parametric DMD, F_{BH} will be ignored for the temperature model. The simulative influence of stroke rate f_{SR} can be verified experimentally so that it remains a control variable. The influence is discussed in Section 11.2.1. So far the austenitizing temperature T_γ is treated as a control variable, while heating temperature T_{Heat} is assumed to be dependent of T_γ. Another possibility is to treat T_γ as a tunable initial value instead of a control parameter. This reduces the number of parameters, but the model has to valid for a wider temperature range. This increases the possibility for the occurrence of simulation errors. Since in DMD, the ratio between the largest and smallest singular value can be large, so that the pseudoinverse may magnify small errors, regularization becomes crucial for computing an accurate model [20]. Subsequently, a Tikhonov regularization parameter α (see [25]) is added to (8.1). This leads to

$$X_1 \approx U_r \sqrt{\left(S_r^2 + \alpha^2 I\right)} V_r^*,$$

with $I \in \mathbb{R}^{r \times r}$. In order to prove the validity of such an parameter the FE model is compared with the DMD model using $\alpha = 10$ in Fig. 8.13. The blue line represents the mean temperature mean($\boldsymbol{T}$) simulated with the parametric DMD without regularization, while gray bars visualize the maximum difference max($\Delta \boldsymbol{T}$) between the parametric DMD model without and with regularization at a node and the red bars visualize the mean difference mean($\Delta \boldsymbol{T}$) over all nodes. As a result it can be seen that $\Delta \boldsymbol{T}$ is negligibly small. The Tikhonov regularization is valid.

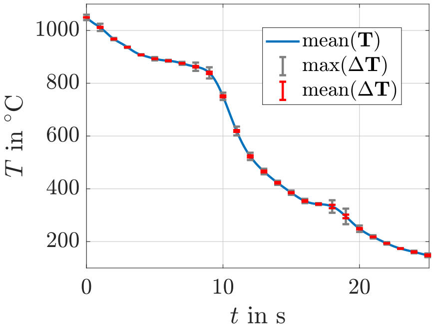

Figure 8.13.: Comparison of temperature evolution obtained from parametric DMD without and with Tikhonov regularization.

The final temperature model has the control variables: Stroke rate f_{SR} and cooling pressure p_{Air}. It has the initial value T_γ. The heating temperature is chosen to be $T_{\mathrm{Heat}} = T_\gamma$ and blank holder force F_{BH} is ignored for the temperature model. Its value is defined in the property control, which is to be discussed in Chapter 10. The DMD is performed with $\alpha = 10$ and the parametric DMD uses the tuple $\theta = (f_{\mathrm{SR}}, p_{\mathrm{Air}})$, whose elements are supposed to fulfill $6\,\mathrm{min}^{-1} \leq f_{\mathrm{SR}} \leq 8\,\mathrm{min}^{-1}$ and $0\,\mathrm{bar} \leq p_{\mathrm{Air}} \leq 2\,\mathrm{bar}$.

9. Temperature Measurement and Estimator Design

The reduced model (dimension $r = 50$) generated from the parametric DMD is used to design a spatial-temporal temperature estimator. The multistage process leads to the fact that both type and location of the temperature measurements vary in the individual stages. These are described, the sensor dynamics are identified and the different instruments are compared. Finally, an estimator with a time varying or respectively stage-dependent output matrix is designed.

9.1. Temperature Measurement

This section describes the way in which the temperature is measured during the multistage press hardening process. First the different instruments used in the experimental setup are introduced, followed by an identification of the transient response of the thermocouples. The section closes with a comparison of the temperature values of these instruments.

9.1.1. Measurement Instruments

In the experimental setup three different temperature measurement instruments are used. A pyrometer is placed to read the temperature y_γ centrally in the austenitizing stage. Another one reads the temperature y_4 in the warm area A_2 of the tempering stage. Four spring-loaded thermocouples $\boldsymbol{y}$ (y_4 is not a thermocouple) are placed throughout stages two to four. In the tempering stage the first thermocouple y_1 measures the temperature in the cold area A_1. In the stretch-forming stage the second thermocouple y_2 is placed centrally, while the fifth one y_5 is located in the sink, where the blank is stretched. In the die bending stage only the third thermocouple y_3 is placed centrally. These placements are visualized in Fig. 9.1. Here, the color represents the temperature of the position with the range from dark blue (cold) over green and orange to yellow (warm). The white dashed isoclines visualize the forming of the sheet metal.

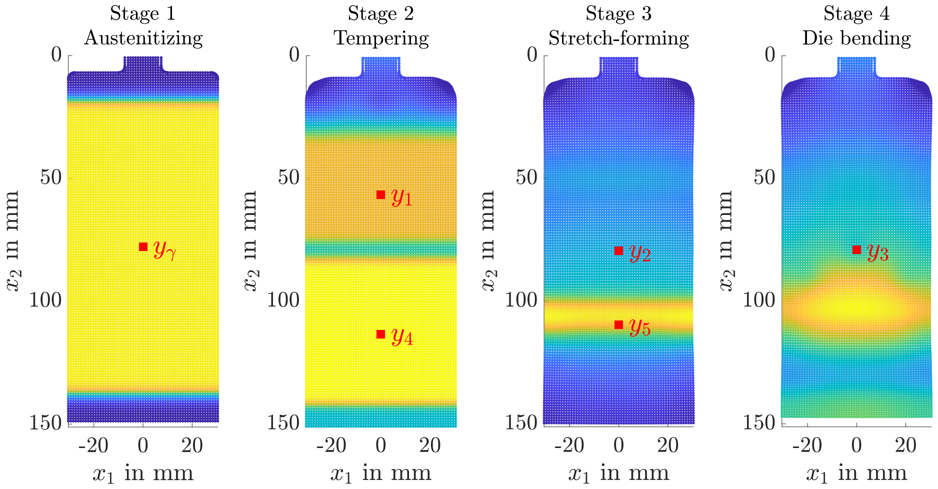

Figure 9.1.: Point measurement via the pyrometers y_γ, y_4 and four spring-loaded thermocouples y_i for $i \in 1, 2, 3, 5$ during the holding steps of the four process stages.

A thermal imaging camera evaluates the temperature distribution in the transfer step between stages 1 and 2 and between stages 2 and 3. Especially four measurement points $\boldsymbol{y}_{\text{th}}$ are extracted out of this distribution. The thermal imaging camera Micro-Epsilons thermoIMAGER TIM M-1 has been used in the experimental setup. It is a shortwave infrared camera ideal for temperature monitoring in the metal processing industry during melting, hardening and forming processes. Its temperature measuring range goes from 450 °C to 1800 °C. Fig. 9.2 shows a screenshot of the camera. The left blank is fully austenitized and transferred to the tempering stage. When the press closes it is cooled in A_1 and heated in A_2. The measurement point $y_{\text{th},1}$ is extracted for parameter identification purposes. Its position equals the one from y_γ. The blank on the right side of the screenshot is heated in A_2 and cooled in A_1. When the press closes it is stretch-formed. Here three measurement points are used. The position of $y_{\text{th},2}$ equals y_1, the position of $y_{\text{th},4}$ equals y_4 and the position of $y_{\text{th},3}$ equals y_2. The emission coefficients of the pyrometers and the thermal imaging camera have previously been experimentally determined. Note, that the thermal imaging camera is only used for model and sensor validation, since the temperature cannot be measured during the relevant holding steps.

The temperature development of the pyrometers, thermocouples and selected thermal imaging camera positions are shown in Fig. 9.3 for an real experiment lasting 60 s with the stroke rate $f_{\text{SR}} = 6\,\text{min}$, austenitizing temperature $T_\gamma = 1000\,°\text{C}$, heating temperature $T_{\text{Heat}} = 1000\,°\text{C}$, cooling pressure $p_{\text{air}} = 0\,\text{bar}$ and blankholder force $F_{\text{BH}} = 5\,\text{kN}$. Fig. 9.3(a) shows temperature development of the pyrometers. The output y_γ increases until it reaches the targeted $T_\gamma = 1000\,°\text{C}$. After a dwell time of about $t_\gamma = 2\,\text{s}$, the press opens and the pyrometers loses contact with blank. Here it shows the minimum output value of about 300 °C, which gives no meaningful information about the actual temperature. This procedure repeats every stroke. The pyrometer

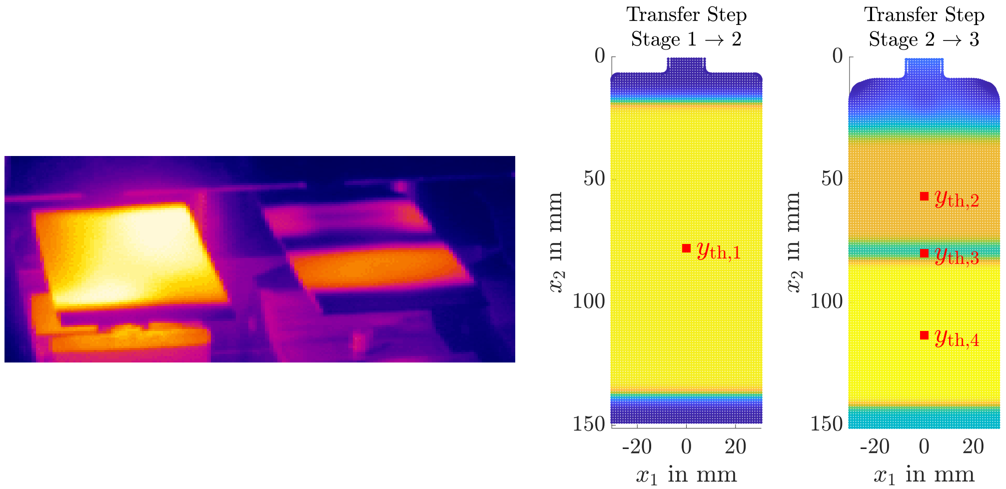

Figure 9.2.: Screenshot (left) and measurement points $\boldsymbol{y}_{\mathrm{th}}$ (right) of the thermal imaging camera.

output y_4 starts increasing in the second stroke as here the tempering stage becomes active. After some time it reaches $T_{\mathrm{Heat}} = 1000\,°\mathrm{C}$ followed by the opening of the press leading to meaningless temperature output values. Fig. 9.3(b) depicts the temperature development of the thermocouples. In the first stroke only the first stage is active, so the room temperature is measured as the thermocouples have no contact with the blank. In the second stroke y_1 shows a value, followed by y_2 and y_5 in the third and y_3 in the forth stroke. At each stroke, where the stage of a thermocouple is active, the temperature starts rising until it decreases with a nearly constant rate, followed by the loss of contact between couple and blank, when the cooling rate increases rapidly. This procedure repeats every stroke. The first temperature rising is a delay of these sensors to be addressed in Section 9.1.2. Fig. 9.3(c) show the temperature development of thermal imaging camera positions $\boldsymbol{y}_{\mathrm{th}}$. Here, values are measured when the press is in the upper dead center. After the first stroke temperatures are only measured at $y_{\mathrm{th},1}$, after the following strokes at all $\boldsymbol{y}_{\mathrm{th}}$. Fig. 9.3(d) shows a smaller time period at about $t = 59$ s to illustrate temperature measure. The camera is always activated and reads at least the minimum value 450 °C. When the press opens for a small time period the left picture of Fig. 9.2 becomes visible and the true temperatures can be read. This time period is longer for $y_{\mathrm{th},1}$ as this output moves along the x_2-direction of the blank when the press opens, where the temperature is (nearly) the same in this stage. The time period is especially shorter for $y_{\mathrm{th},3}$ as it has the same temperature in x_2-direction in a very small range, which can be seen in the right picture of Fig. 9.2. All these measurements are related to each other in Section 9.1.3.

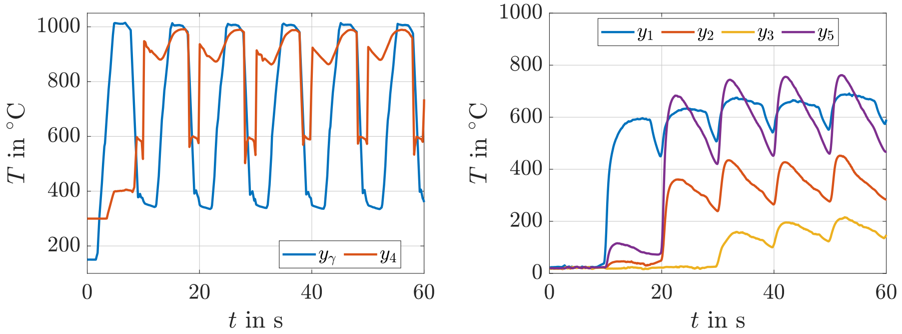

(a) Temperature development of pyrometers.

(b) Temperature development of thermocouples.

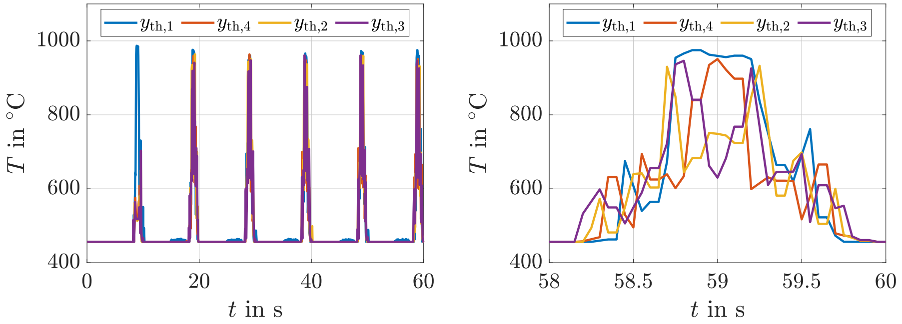

(c) Temperature development of selected thermal imaging camera positions.

(d) Temperature development of selected thermal imaging camera positions at $t = 59$ s.

Figure 9.3.: Temperature development of the pyrometers, thermocouples and selected thermal imaging camera positions.

9.1.2. Delay of Thermocouples

The temperature development of the thermocouples is exemplarily depicted in Fig. 9.4 for y_1 in an experimental scenario with $f_{\text{SR}} = 8\,\text{min}^{-1}$. Due to the set stroke rate, eight process cycles take place in 60 s. During the first stroke, only the first stage, the austenitizing stage, is active, which is why the thermocouple y_1 is at room temperature. It can be seen that the sensors exhibit a delay at the beginning of each stroke. At the end of each stroke, as the press opens, the sensor loses contact and cools rapidly. Looking at the upper envelope $y_{1,\text{env}}$ it also emerges that there is a delay over all strokes, as the maximum value of each individual stroke increases in the first strokes until it reaches the actual value. Both delays can be described by a 1st order lag element (PT_1). In this section two optimization problems are set up and solved in order to identify and take these behaviors into account.

In twelve real experiments with a duration of 60 s each, the time constants of the PT_1 behavior were identified for four thermocouples on the basis of an optimization problem. Depending on

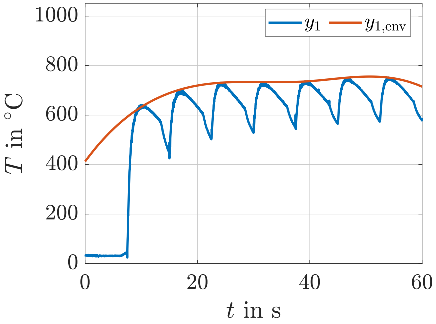

Figure 9.4.: Temperature development of thermocouple y_1 and its upper envelope $y_{1,\text{env}}$.

the stroke rate f_{SR} this leads to a number between six and eight strokes used for identification. The optimization problem

$$\min_{\boldsymbol{\tau}} J = \sum_{e=1}^{E} \sum_{h=H_{s,1}}^{H_i} \sum_{k=0}^{K-1} \left\| \bar{\boldsymbol{y}}(e,h,t_k) - \boldsymbol{y}(e,h,t_k) \right\|_1, \tag{9.1}$$

is set up to determine the PT$_1$ parameter $\boldsymbol{\tau}$, where the total number of evaluated experiments $E = 12$, the number of strokes per experiment H_i, which is six, seven or eight, depending on the stroke rate f_{SR}, the first active stroke $H_{s,1}$, the number of time steps per stroke K and the approximation function

$$\begin{aligned} \bar{\boldsymbol{y}}(e,h,t_k) &= D\left(\boldsymbol{y}_{\text{a}}(e,h,t_k) - \boldsymbol{y}(e,h,t_0)\right) + \boldsymbol{y}(e,h,t_0), \\ d_i &= \left(1 - e^{-k\Delta t/\tau_i}\right), \quad i = 1,2,3,5, \\ \boldsymbol{y}_{\text{a}}(e,h,t_k) &= m_{\text{dec}} k \boldsymbol{\Delta t} + n_{\text{start}}, \end{aligned}$$

are given, with diagonal matrix D with entries $[d_1, d_2, d_3, 1, d_5]$. Here, m_{dec} denotes the degree of the temperature decrease during the stroke, while n_{start} represents the starting value. The right picture of Fig. 9.5 shows an exemplary development of $\bar{y}_1$ and $y_{\text{a},1}$. The left picture of Fig. 9.5 shows a stroke of all the four thermocouples, where the solid lines are the optimized temperature developments $\bar{\boldsymbol{y}}$ and the dotted lines are measured data $\boldsymbol{y}$. The right picture of the same figure visualizes the same stroke in more detail for y_1. Here, the measured data y_1 fits the simulated approximation extended by the optimized delay behavior $\bar{y}_1$ quite well, while the non-extended approximation function $y_{\text{a},1}$ does not capture the delay behavior. The determined optimized PT$_1$ element parameters are listed in Table 9.1.

A similar optimization problem is solved for the delay arising over all strokes. This is necessary due to the fact, that especially in the first active stroke the temperature is lower than in the

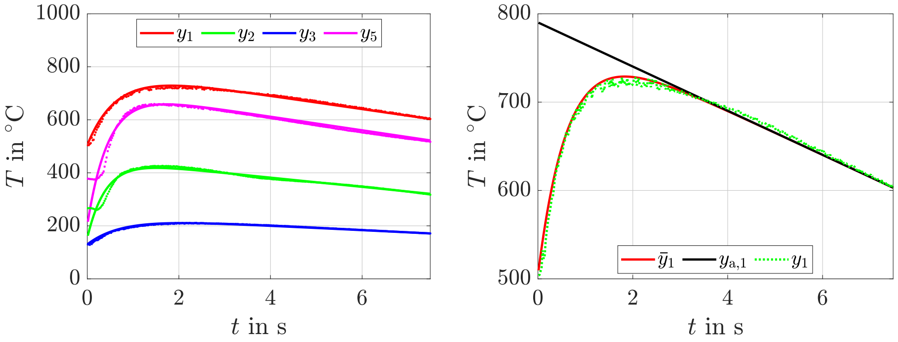

Figure 9.5.: Measurements $\boldsymbol{y}$ (dotted) and optimized approximations $\bar{\boldsymbol{y}}$ (solid) for an exemplary stroke in the left picture and measurement y_1, approximation $y_{a,1}$ and its optimization $\bar{y}_1$ of the same stroke in the right picture.

following ones. For this setup only the maximum temperatures at each thermocouple $\boldsymbol{y}_{\max}(e, h)$ during the h-th stroke of the e-th experiment are taken into account. The optimization problem

$$\min_{\boldsymbol{\tau}_{\text{Str}}} J = \sum_{e=1}^{E} \sum_{h=H_{s,1}}^{H_i} \left\| \bar{\boldsymbol{y}}_{\max}(e, h) - \boldsymbol{y}_{\max}(e, h) \right\|_1 \tag{9.2}$$

determines the PT$_1$ parameters $\boldsymbol{\tau}_{\text{Str}}$. Here, the number of evaluated experiments $E = 12$, the number of strokes H_i, the first active stroke $H_{s,1}$ and the approximation function

$$\begin{aligned} \bar{\boldsymbol{y}}_{\max}(e, h) &= D_{\text{str}} \left(\boldsymbol{y}_{\text{a,max}}(e, h) - \boldsymbol{y}_{\max}(e, H_{s,1}) \right) + \boldsymbol{y}_{\max}(e, H_{s,1}), \\ d_{\text{str},i} &= \left(1 - e^{-h/\tau_{\text{Str},i}} \right), \qquad i = 1, 2, 3, 5, \\ \boldsymbol{y}_{\text{a,max}}(e, h) &= \boldsymbol{y}_{\max}(e, H_i). \end{aligned}$$

are given, with diagonal matrices D_{str} with entries $[d_{\text{str},1}, d_{\text{str},2}, d_{\text{str},3}, 1, d_{\text{str},5}]$ and the maximum measured value of the last evaluated stroke $\boldsymbol{y}_{\max}(e, H_i)$. The right picture of Fig. 9.6 shows an exemplary development of $\bar{y}_{\max,1}$ and $y_{\text{a,max},1}$. The left picture of Fig. 9.6 shows a temperature development of all the four thermocouples over the strokes, where the maximum values of each stroke are connected, the solid lines are the optimized temperature developments $\bar{\boldsymbol{y}}_{\max}$ and the dotted lines are measured data $\boldsymbol{y}_{\max}$. The right picture of the same figure visualizes the same experiment in more detail for $y_{\max,1}$. Here, the measured data $y_{\max,1}$ fits the approximation with added optimized delay behavior $\bar{y}_{\max,1}$ quite well. The non-extended approximation $y_{\text{a,max},1}$ is also given for reasons of comparison. The determined optimized PT$_1$ element parameters $\boldsymbol{\tau}_{\text{Str}}$ are listed in Table 9.1.

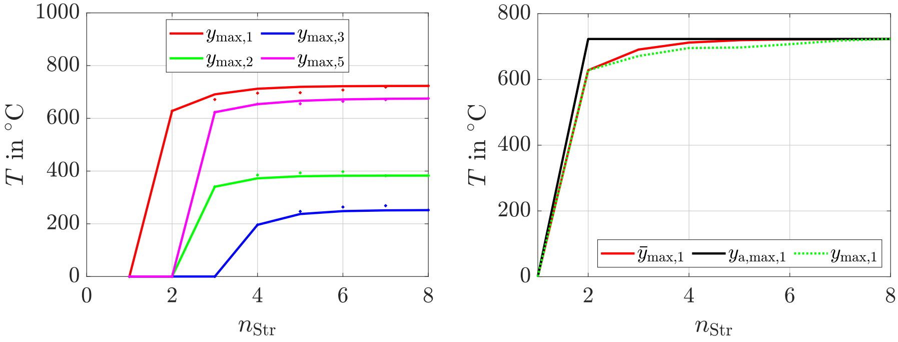

Figure 9.6.: Maximum measurements $\boldsymbol{y}_{\mathrm{max}}$ (dotted) and optimized approximations $\bar{\boldsymbol{y}}_{\mathrm{max}}$ (solid) for eight consecutive strokes in the left picture and maximum measurement $y_{\mathrm{max},1}$, approximation $y_{\mathrm{a,max},1}$ and its optimization $\bar{y}_{\mathrm{max},1}$ of the same strokes in the right picture.

Thermocouple	τ	τ_{Str}
y_1	0.6684	0.9224
y_2	0.4201	0.7126
y_3	0.7751	0.7573
y_5	0.4746	1.1418

Table 9.1.: Opimized values of the PT$_1$ parameters in each stroke τ and over all strokes τ_{Str}.

9.1.3. Comparison of Temperature Values

To validate the functionality of different measurement instruments, the resulting temperature values y_γ, $\boldsymbol{y}$, and $\boldsymbol{y}_{\mathrm{th}}$ are compared. Sixteen experiments have been conducted, with the measurements starting in first holding step at $t = 0$. The sixth stroke of an exemplarily experiment with $f_{\mathrm{SR}} = 6\,\mathrm{min}^{-1}$ is shown in Fig. 9.7 and 9.8.

Fig. 9.7 presents a comparison of pyrometer and thermal imaging camera outputs. In Fig. 9.7(a), the rising pyrometer y_γ and the camera output $y_{\mathrm{th},1}$ are shown, both situated at the same position of the blank. The pyrometer measures the temperature at the right position of the blank during the holding step ($t = 50$ to 57.5 s), while the camera measures at the right position at about $t = 59$ s. When the temperature reached 1000 °C and was held for a few seconds, y_γ decreased rapidly, attributed to the loss of contact with the blank. During the subsequent transfer step, the temperature gradually decreased due to heat convection with the surrounding air, as indicated by the camera value $y_{\mathrm{th},1}$. The measurements from the pyrometer and the thermal imaging camera connect well to each other, as seen by the black dotted temperature trend line.

Fig. 9.7(b) provides a similar comparison, where temperatures of $y_{\mathrm{th},1}$ (equivalent to the position of y_4), y_4 and $y_{\mathrm{th},4}$ are compared. The agreement between the instruments is once again evident.

The camera output $y_{\mathrm{th},1}$ connects well with y_4 at about $t = 50\,\mathrm{s}$ and $y_{\mathrm{th},4}$ connects well with y_4 at about $t = 59\,\mathrm{s}$. Both connections are shown by black dotted temperature trend lines.

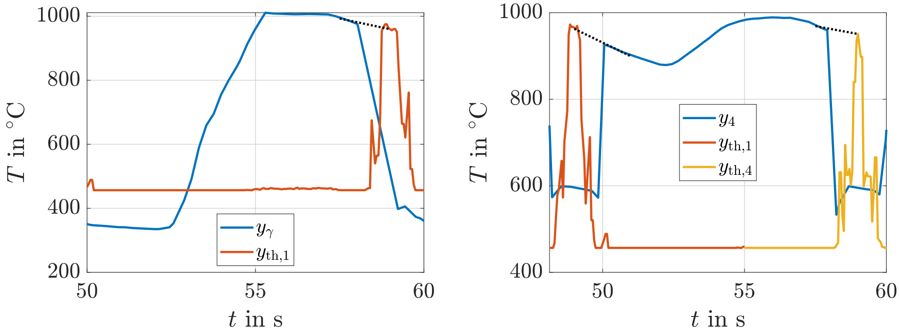

(a) Output y_γ in stage 1 and $y_{\mathrm{th},1}$ during the following transfer step.

(b) Output $y_{\mathrm{th},1}$ during the transfer to stage 2, y_4 in stage 2 and $y_{\mathrm{th},4}$ during the transfer to stage 3.

Figure 9.7.: Comparison of pyrometers y_γ, y_4 and thermal imaging camera outputs $\boldsymbol{y}_{\mathrm{th}}$.

The thermocouples can be placed in the tools, so they have contact with the blank during the holding steps. Looking at Fig. 9.8, the delays of the thermocouples (blue lines), which have been already taken into account in Section 9.1.2, can be seen. In order to compensate these delays, temperature trends $\boldsymbol{y}_a$ are constructed as yellow lines with the linear decrease of the thermocouples after the transient response. These are compared with the thermal imaging camera values at the same positions (orange lines). The comparisons take place at the transfer before the tempering stage at y_1 (see Fig. 9.8(a)), after the same stage at y_1 (see Fig. 9.8(b)) and before the stretch-forming stage at y_2 and y_5 (see Fig. 9.8(c) and 9.8(d)). Note that these comparisons are not exact. The thermocouple behavior is not exactly linear and the temperature decrease might differ in the transfer step, when the comparison with the thermal imaging camera is made and during the holding step. These comparisons only give an approximate difference between thermocouple and camera.

The values of y_2 and y_5 connect quite well with the camera outputs. The differences between these instruments are 77.8615 °C and 39.1991 °C on average of all experiments. They are listed as offsets $\boldsymbol{N}_{\mathrm{Off,b}}$ in Tab. 9.2. These differences seem to be negligibly small since the comparisons are only approximate. Further experimental analysis in Chapter 11 verifies this assumption.

The value of y_1 is much lower than the camera outputs before and after the stage. The average differences $\boldsymbol{N}_{\mathrm{Off,b}}$ and $\boldsymbol{N}_{\mathrm{Off,a}}$ are listed in Tab. 9.2. A reason for this difference might be the fact that these thermocouples have problems to read very high temperatures. In order to be able to use y_1 as measurement instrument during the holding step an offset function $y_{1,\mathrm{Off}}(t_k)$ is added to the output value to take this difference into account

$$y_{1,\mathrm{Off}}(t_k) = \frac{(-120\,^\circ\mathrm{C})k\boldsymbol{\Delta t}}{\tau_{\mathrm{Ho}}} + 200\,^\circ\mathrm{C}. \tag{9.3}$$

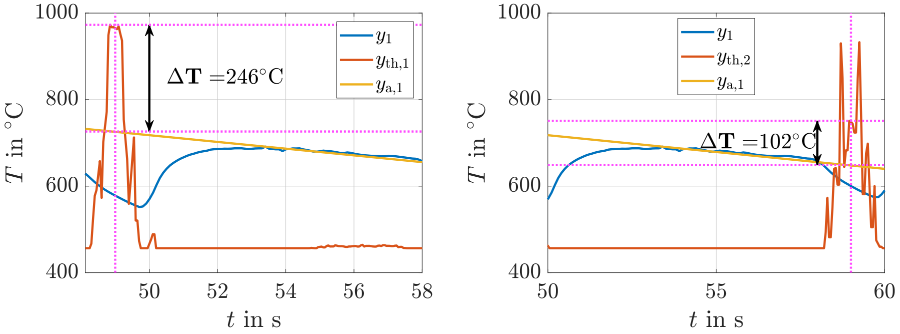

(a) Output $y_{\mathrm{th},1}$ during the transfer to stage 2 and y_1 in stage 2.

(b) Output y_1 in stage 2 and $y_{\mathrm{th},2}$ during the following transfer step.

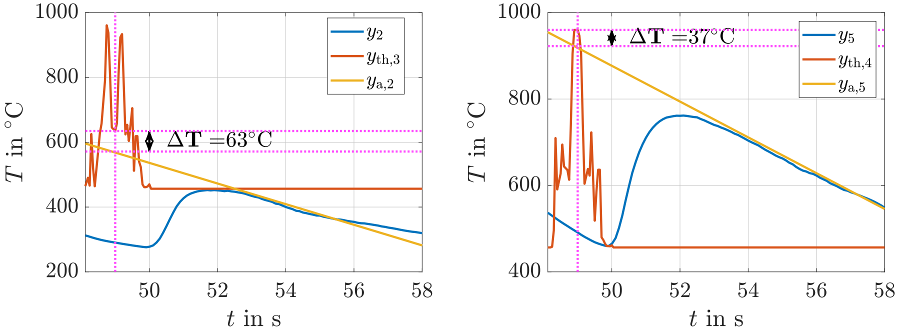

(c) Output $y_{\mathrm{th},3}$ during the transfer to stage 3 and y_2 in stage 3.

(d) Output $y_{\mathrm{th},4}$ during the transfer to stage 3 and y_5 in stage 3.

Figure 9.8.: Comparison of thermocouples $\boldsymbol{y}$ and thermal imaging camera outputs $\boldsymbol{y}_{\mathrm{th}}$.

This function is linear with $y_{1,\mathrm{Off}}(t_0) = 200\,°\mathrm{C}$ at the holding step's beginning t_0 and a value of 80 °C at the holding step's end. The value of y_3 could not be verified with the thermal imaging camera. Its functionality is assumed as is verified by further analysis in Chapter 11.

Thermocouple	$\boldsymbol{N}_{\mathrm{Off,b}}$	$\boldsymbol{N}_{\mathrm{Off,a}}$
y_1	237.4167 °C	92.2822 °C
y_2	77.8615 °C	-
y_3	-	-
y_5	39.1991 °C	-

Table 9.2.: Average differences between thermocouple and thermal imaging camera before $\boldsymbol{N}_{\mathrm{Off,b}}$ and after $\boldsymbol{N}_{\mathrm{Off,a}}$ the holding step.

9.2. Estimator Design

The model derived by the parametric DMD combined with the temperature measurements $\boldsymbol{y}(t_k)$ implies the discrete time representation

$$\boldsymbol{T}_r(t_{k+1}) = \Lambda \boldsymbol{T}_r(t_k), \qquad k \in \mathbb{N}, \quad \boldsymbol{T}_r(t_0) = \boldsymbol{T}_r^0, \tag{9.4a}$$

$$\boldsymbol{y}(t_k) = C_r(t_k)\boldsymbol{T}_r(t_k), \tag{9.4b}$$

with $\boldsymbol{T}_r(\cdot) = \boldsymbol{T}_r(\theta, \cdot) \in \mathbb{R}^r$ the reduced state vector and initial values $\boldsymbol{T}_r^0$ at time $t_0 = 0$ s. Note that the mapping $\boldsymbol{T}(\theta, t_k) \approx \Phi(\theta)\boldsymbol{T}_r(\theta, t_k) \in \mathbb{R}^n$ provides the full (nodal) temperature vector. The sampling time $\Delta t = t_{k+1} - t_k$ and the system matrix $\Lambda \in \mathbb{R}^{r \times r}$ are determined by the parametric DMD, while the time varying output matrix $C_r(t_k) \in \mathbb{R}^{n_{\text{sen}} \times r}$ with the number of sensors n_{sen} has to be set up from the actual sensor configuration.

9.2.1. Design of the Output Matrix

As already elaborated in Section 9.1 the temperature is measured with four spring loaded thermocouples installed in the die stages and two pyrometers. Each thermocouple and pyrometer measures the temperature in the sheet blank in one of the stages while the ram is near the bottom dead center. These measurements take place at four different locations $p_1 = 93$, $p_2 = 90$, $p_3 = 60$ and $p_4 = 37$ as depicted in Fig. 9.9 during three simulated stages. Here, the values correspond to the node positions in x_2-direction. In the tempering stage the temperature is measured at two positions p_1 and p_4, in the stretch-forming stage at p_2 and p_3 and in the die bending stage only at p_3.

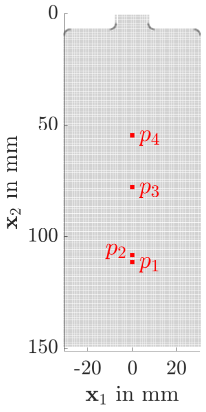

Figure 9.9.: Measurement positions $\boldsymbol{p}$ on the sheet blank.

Consequently the output matrix $C(t_k) \in \mathbb{R}^{n_{\mathrm{sen}} \times n}$ for the full order (non-reduced nodal) system is stage-dependent, which in view of the stroke rate f_{SR} can be transferred to a time varying setting. Let $t_{e,1}$ denote end-time of the tempering stage, $t_{e,2}$ the end-time of the stretch drawing stage, and t_e the process time when passing all simulated stages, the number of rows of $C(t_k)$ is given by

$$n_{\mathrm{sen}} = \begin{cases} 2, & t_k < t_{e,2}, \\ 1, & t_{e,2} < t_k \leq t_e. \end{cases}$$

The respective non-zero elements $C_{i,j}(t_k)$ of $C(t_k)$ can be defined as $C_{1,p_1}(t_k < t_{e,1}) = 1$, $C_{2,p_4}(t_k < t_{e,1}) = 1$, $C_{1,p_3}(t_{e,1} < t_k \leq t_e) = 1$ and $C_{2,p_2}(t_{e,1} < t_k \leq t_{e,2}) = 1$. Applying the projection $C_r(t_k) = C(t_k)\Phi(\theta)$ yields the corresponding output matrix for (9.4).

9.2.2. Kalman Filter

The estimator is set up in the simulator-corrector form including the determined delays of Section 9.1.2 and the offset (9.3) of Section 9.1.3.

$$\hat{\boldsymbol{T}}_r(t_{k+1}) = \Lambda \hat{\boldsymbol{T}}_r(t_k) + L(t_k)\left(\boldsymbol{y}_{\mathrm{c}}(t_k) - \hat{\boldsymbol{y}}(t_k)\right), \quad \hat{\boldsymbol{T}}_r(t_0) = \hat{\boldsymbol{T}}_r^0, \tag{9.5a}$$

$$\hat{\boldsymbol{y}}(t_k) = \underbrace{D_{\mathrm{str}}(\underbrace{D(\underbrace{C_r(t_k)\hat{\boldsymbol{T}}_r(t_k)}_{\substack{\text{Estimated output}\\ \text{without delays}}} - \boldsymbol{y}_{\mathrm{c}}(t_s))}_{\substack{\text{Estimated output}\\ \text{including delays inside each stroke}}} + \boldsymbol{y}_{\mathrm{c}}(t_s) - \boldsymbol{y}_{\max}(H_{s,1})) + \boldsymbol{y}_{\max}(H_{s,1})}_{\text{Estimated output including delays inside each stroke and over all strokes}}, \tag{9.5b}$$

with $k \in \mathbb{N}_0$, the starting index of each stroke $s = (h-1)\tau_{\mathrm{cyc}}/\Delta t$, stroke number $h \in \mathbb{N}$, the maximum temperatures at each thermocouple $\boldsymbol{y}_{\max}(H_{s,1})$ during the first active stroke $H_{s,1}$, diagonal matrices D_{str} with entries $[d_{\mathrm{str},1}, d_{\mathrm{str},2}, d_{\mathrm{str},3}, 1, d_{\mathrm{str},5}]$ and D with entries $[d_1, d_2, d_3, 1, d_5]$ and

$$d_{\mathrm{str},i} = \left(1 - e^{-h/\tau_{\mathrm{Str},i}}\right), \; d_i = \left(1 - e^{-k\Delta t/\tau_i}\right), \quad i = 1, 2, 3, 5.$$

Here, D_{str} includes the delays over all stokes and D the delays inside each individual stroke. The offset $\boldsymbol{y}_{\mathrm{Off}}(t_k)$ of Section 9.1.3 is added to the measurement output $\boldsymbol{y}(t_k)$ defining

$$\boldsymbol{y}_{\mathrm{c}}(t_k) = \boldsymbol{y}(t_k) + \boldsymbol{y}_{\mathrm{Off}}(t_k),$$

where $y_{i,\mathrm{Off}}(t_k) = 0$ for $i = 2, \dots, 5$ holds.

In particular a discrete time Kalman filter [37] is designed minimizing the variance of the estimation error $\tilde{\boldsymbol{T}}_r(t_k) = \boldsymbol{T}_r(t_k) - \hat{\boldsymbol{T}}_r(t_k)$ under the assumption of zero mean Gaussian process and measurement noise with covariance matrices $Q \in \mathbb{R}^{n \times n}$ and $R(t_k) \in \mathbb{R}^{n_{\text{sen}} \times n_{\text{sen}}}$ [24]. The time varying estimator gain matrix

$$L(t_k) = P(t_k)C_r(t_k)^T \left(C_r(t_k)P(t_k)C_r(t_k)^T + R(t_k)\right)^{-1}$$

with the matrix $P(t_k)$ is obtained from solving the discrete time algebraic Riccati equation

$$\begin{aligned} P(t_k) =& \Lambda P(t_k)\Lambda^T - (\Lambda P(t_k)C_r(t_k)^T)(R(t_k) \\ &+ C_r(t_k)P(t_k)C_r(t_k)^T)^{-1}(C_r(t_k)P(t_k)\Lambda^T) + Q. \end{aligned}$$

With this estimator the reconstruction of the spatial-temporal temperature distribution on the sheet metal $\boldsymbol{T}(\theta, t)$ is possible for all parameter configurations θ. It is experimentally validated in Section 11.3.

10. Optimal Control Design

Making use of the designed estimator, this chapter presents an optimal control for the multistage press hardening process. First the underlying control loop is described, followed by a the design of an optimal temperature control.

10.1. Control Loop

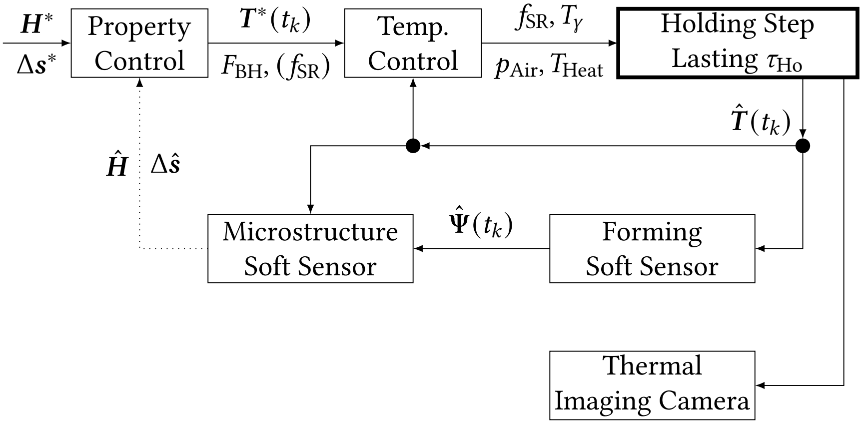

Figure 10.1.: Control loop of the multistage press hardening process including the property and temperature control, the microstructure and forming soft sensors, the thermal imaging camera and the process holding step, which is described more detailed in Fig. 10.2.

Fig. 10.1 shows the closed control loop of the multistage press hardening process. Here, the target temperature trajectories $\boldsymbol{T}^*(t_k)$ are provided by the property control. It takes the defined target properties, hardness $\boldsymbol{H}^*$ and sheet thinning $\Delta \boldsymbol{s}^*$ at the end of the process as inputs and calculates the desired temperature trajectory $\boldsymbol{T}^*(t_k)$ as an output. Furthermore it sets the blank holder force F_{BH} and it might set a desired range for the stroke rate f_{SR}, as these two control variables have direct influence on the properties. Its design is developed within the project 424334660 of the Priority Program SPP2183 ”Property-controlled forming processes” funded by the Deutsche Forschungsgemeinschaft (DFG). With these results the optimal temperature control, which is described in more detail in Section 10.2, calculates the actuator configuration,

$\theta = (f_{\mathrm{SR}}, p_{\mathrm{Air}})$ and initial value T_γ for the upcoming holding step with a duration of τ_{Ho}. When this is finished, the estimated temperature trajectory of the last holding step $\hat{\boldsymbol{T}}(t_k)$ is fed back to the temperature control.

The temperature also serves as an input for two developed soft sensors [31]. The forming soft sensor is a gray box model, which calculates the estimated forming degree $\hat{\boldsymbol{\Psi}}(t_k)$ with the temperature knowledge. The microstructure soft sensor is a neural network, which is trained to predict the final properties, hardness $\hat{\boldsymbol{H}}$ and sheet thinning $\Delta\hat{\boldsymbol{s}}$, based on the knowledge of the temperature's $\hat{\boldsymbol{T}}(t_k)$ and forming degree's $\hat{\boldsymbol{\Psi}}(t_k)$ history. These soft sensors are described in detail in [46]. The estimated properties are used for the property control. This path (dotted line) is not realized within the scope of this thesis, but it is an upcoming task in the project. With the property control, the target properties $\boldsymbol{H}^*$ and $\Delta\boldsymbol{s}^*$ are given and the needed temperature trajectory $\hat{\boldsymbol{T}}(t_k)$ is calculated. After the holding step also the thermal imaging camera starts its measurement, which is used for parameter identifications.

Fig. 10.2 describes the block 'Holding Step Lasting τ_{Ho}' in detail. It shows the influence of the actuators towards the different process stages and the sensor measurement combined with the Kalman filter. The thick left bar visualizes the start of the holding step of the process at $t_k = \tau_{\mathrm{Ho,s}} = \tau_{\mathrm{Tr}} + \tau_{\mathrm{Cl}} + \tau_{\mathrm{Fo}}$ and the the bar to the right the end of the holding step at $t_k = \tau_{\mathrm{Ho,e}} = \tau_{\mathrm{Tr}} + \tau_{\mathrm{Cl}} + \tau_{\mathrm{Fo}} + \tau_{\mathrm{Ho}}$. At the beginning all five actual actuator parameters, chosen from the optimal temperature control problem described in Section 10.2, take their way. The actual austenitizing temperature $T_{\gamma,h}$ sets the desired value of the input/output PID controller and in this way the power of the induction generator heating the blank in the first stage. Via a pyrometer the actual temperature y_γ is fed back to the PID controller. The same procedure is implemented for A_2 of the tempering stage with the desired temperature $T_{\mathrm{Heat},h}$, whereby here a DC resistance heating generator and the pyrometer y_4 are used for control and measurement. Area A_1 of this stage is cooled with the air pressure $p_{\mathrm{Air},h}$ using flat fan nozzles. The area's positions can be seen in Fig. 8.5. The blank holder force $F_{\mathrm{BH},h}$ is the input of a valve influencing the third stage. A reduced order DMD model of the stages 2, 3 and 4 simulates the temperature development in the blank $\boldsymbol{T}(t_k)$. It receives its initial value from the austenitizing temperature of the previous stroke $T_{\gamma,h-1}$ for stage 2, the starting value for stage 3 from the last value of stage 2 from the previous stroke $\boldsymbol{T}_{\mathrm{T},h-1}$ and the starting value for stage 4 from the last value of stage 3 from the previous stroke $\boldsymbol{T}_{\mathrm{SF},h-1}$. For the estimation of these models five different measurement positions $\boldsymbol{y}$ are used as sensors. These are the pyrometer y_4 in A_2 of stage 2 and the thermocouples y_1 in A_1 of stage 2, y_2 and y_5 in stage 3 and y_3 in stage 4. These measurements are used for the Kalman filter design, which minimizes the difference between estimated $\hat{\boldsymbol{y}}$ and measured sensor outputs $\boldsymbol{y}$. It calculates the temperature trajectory $\hat{\boldsymbol{T}}_h(t_k)$, which is later used for the optimal control problem of the next stroke. The stroke rate $f_{\mathrm{SR},h}$ determines the velocity of the servo-hydraulic press and though the duration of the holding step. Its end is determined via a sensor, which measures the position of the ram h_{Ram}. When its value exceeds a defined trigger h_{Ho}, the holding step ends. The position of the ram h_{Ram} activates and deactivates the control variables. For $f_{\mathrm{SR}} = 6\,\mathrm{min}^{-1}$ the temporal development as depicted in Fig. 10.3 evolves. If h_{Ram} has fallen below the green dotted line at $h_{\mathrm{Ho}} = 290\,\mathrm{mm}$ the holding step starts and it ends, if $h_{\mathrm{Ram}} > h_{\mathrm{Ho}}$. The start and end of the holding step is visualized with magenta dotted lines.

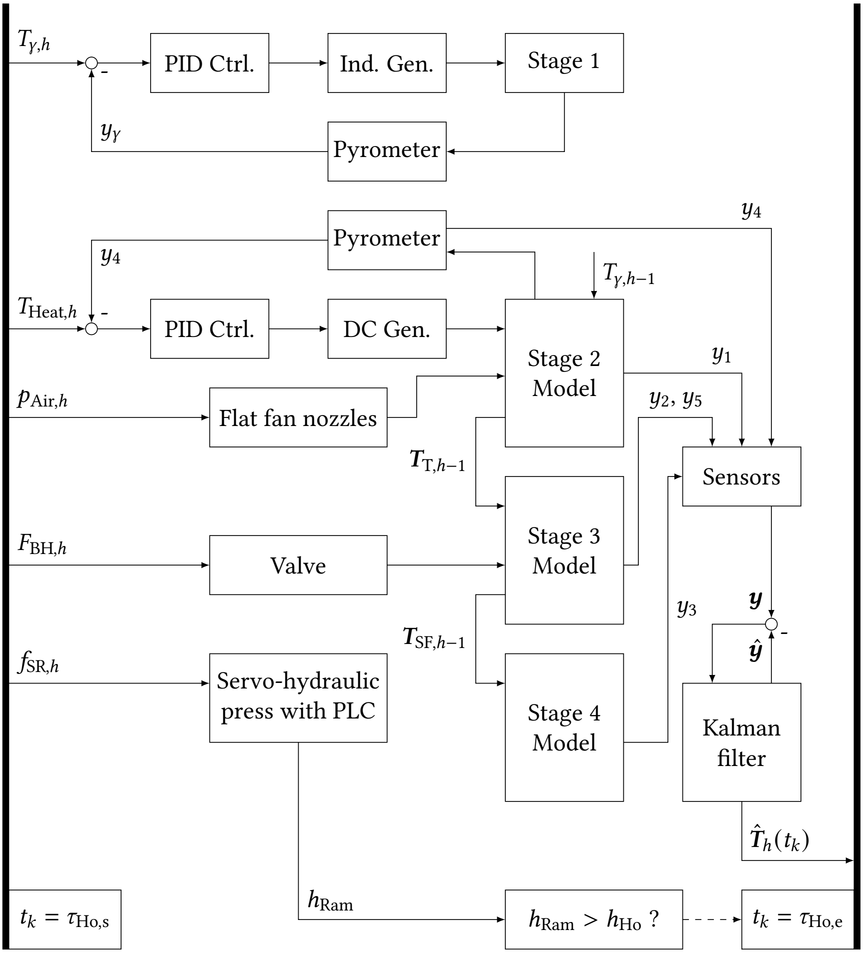

Figure 10.2.: Overview of the relations between actuators, process models and sensors for the holding step of stroke h.

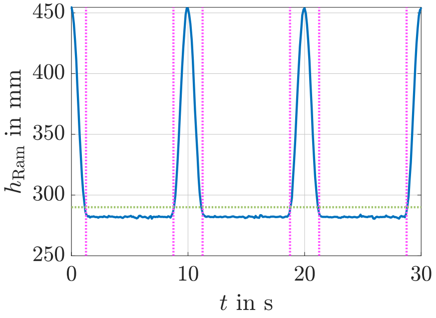

Figure 10.3.: Position h_{Ram} of the ram in a scenario with $f_{\mathrm{SR}} = 6\,\mathrm{min}^{-1}$.

10.2. Optimal Control Problem

The property control in this multistage press hardening process goes hand in hand with the control of the blank's temperature, so that the properties of the finished blank can be influenced in a targeted manner.

This control design involves the estimator (9.5) based on the reduced model derived from the parametric DMD (8.5). Regarding Fig. 10.2 three stages are modeled in parallel during each holding step. This leads to the three estimated state vectors in the tempering (T), stretch-forming (SF) and die bending (DB) stages

$$\hat{\boldsymbol{T}}_{\mathrm{T},h}(t_k) = \hat{\boldsymbol{T}}_h(t_k), \quad \hat{\boldsymbol{T}}_{\mathrm{SF},h}(t_k) = \hat{\boldsymbol{T}}_h(t_k + \tau_{\mathrm{cyc}}), \quad \hat{\boldsymbol{T}}_{\mathrm{DB},h}(t_k) = \hat{\boldsymbol{T}}_h(t_k + 2\tau_{\mathrm{cyc}})$$

and their reduced order representations (see (9.5))

$$\begin{aligned} &\hat{\boldsymbol{T}}_{r,\mathrm{T},h}(t_k) = \hat{\boldsymbol{T}}_{r,h}(t_k), \quad \hat{\boldsymbol{T}}_{r,\mathrm{SF},h}(t_k) = \hat{\boldsymbol{T}}_{r,h}(t_k + \tau_{\mathrm{cyc}}), \\ &\hat{\boldsymbol{T}}_{r,\mathrm{DB},h}(t_k) = \hat{\boldsymbol{T}}_{r,h}(t_k + 2\tau_{\mathrm{cyc}}). \end{aligned}$$

Again, $\tau_{\mathrm{Ho,s}} = \tau_{\mathrm{Tr}} + \tau_{\mathrm{Cl}} + \tau_{\mathrm{Fo}}$ denotes the time at which the holding step starts, $\tau_{\mathrm{Ho,e}} = \tau_{\mathrm{Tr}} + \tau_{\mathrm{Cl}} + \tau_{\mathrm{Fo}} + \tau_{\mathrm{Ho}}$ the time at which the holding step ends. The austenitizing temperature $T_{\gamma,h-1}$ and the estimated temperatures $\hat{\boldsymbol{T}}_{\mathrm{T},h-1}(\tau_{\mathrm{Ho,e}})$ and $\hat{\boldsymbol{T}}_{\mathrm{SF},h-1}(\tau_{\mathrm{Ho,e}})$ at the end of the previous holding step are used as initial values to simulate the temperatures in the next holding step related to (8.5) with

$$\begin{aligned} \bar{\boldsymbol{T}}_{\mathrm{T},h}(t_k) &= \Phi(f_{\mathrm{SR},h}, p_{\mathrm{Air},h}) \Lambda^{\frac{t_k}{\Delta t}} \Phi^{\dagger}(f_{\mathrm{SR},h}, p_{\mathrm{Air},h}) T_{\gamma,h-1} \mathbf{1}, \\ \bar{\boldsymbol{T}}_{\mathrm{SF},h}(t_k) &= \Phi(f_{\mathrm{SR},h}, p_{\mathrm{Air},h}) \Lambda^{\frac{t_k + (\tau_{\mathrm{cyc}} - \tau_{\mathrm{Ho,e}})}{\Delta t}} \Phi^{\dagger}(f_{\mathrm{SR},h}, p_{\mathrm{Air},h}) \hat{\boldsymbol{T}}_{\mathrm{T},h-1}(\tau_{\mathrm{Ho,e}}), \\ \bar{\boldsymbol{T}}_{\mathrm{DB},h}(t_k) &= \Phi(f_{\mathrm{SR},h}, p_{\mathrm{Air},h}) \Lambda^{\frac{t_k + (\tau_{\mathrm{cyc}} - \tau_{\mathrm{Ho,e}})}{\Delta t}} \Phi^{\dagger}(f_{\mathrm{SR},h}, p_{\mathrm{Air},h}) \hat{\boldsymbol{T}}_{\mathrm{SF},h-1}(\tau_{\mathrm{Ho,e}}). \end{aligned}$$

The temperature control aims for the minimization of the difference between the specified target temperature $\boldsymbol{T}_h^*$ and the estimator-based one $\bar{\boldsymbol{T}}_h$ in the blank. For this purpose, in each stroke h target temperature trajectories are designed in the holding steps of the tempering, stretch-forming and die bending stages: $\boldsymbol{T}_{\mathrm{T},h}^*(t_k)$, $\boldsymbol{T}_{\mathrm{SF},h}^*(t_k)$ and $\boldsymbol{T}_{\mathrm{DB},h}^*(t_k)$. The difference is minimized at certain positions N_T of the blank, where N_T is a set of elements from temperature vector $\boldsymbol{T}_h$. At the beginning of each stroke h, the optimal control problem

$$\begin{aligned} \min_{f_{\mathrm{SR},h}, T_{\gamma,h}, p_{\mathrm{Air},h}} J_h = \sum_{k=\tau_{\mathrm{Ho,s}}}^{\tau_{\mathrm{Ho,e}}} \sum_{i \in N_T} &\left\| \bar{T}_{\mathrm{T},i,h}(t_k) - T_{\mathrm{T},i,h}^*(t_k) \right\|_1 \\ &+ \left\| \bar{T}_{\mathrm{SF},i,h}(t_k) - T_{\mathrm{SF},i,h}^*(t_k) \right\|_1 \\ &+ \left\| \bar{T}_{\mathrm{DB},i,h}(t_k) - T_{\mathrm{DB},i,h}^*(t_k) \right\|_1, \end{aligned} \tag{10.1a}$$

s.t.

$$f_{\mathrm{SR},h} \in \{6, 6.5, 7, 7.5, 8\}, \quad T_{\gamma,h} \in (900, 1000), \quad p_{\mathrm{Air},h} \in \{0, 2\}, \tag{10.1b}$$

is solved.

In order to fulfill the requirement of real-time applicability, the solution of this problem must not exceed a duration of $t_{\max} = \tau_{\mathrm{cyc}} - \tau_{\mathrm{Ho}}$. This corresponds at least to $t_{\max} = 1.875$ s for $f_{\mathrm{SR}} = 8\,\mathrm{min}^{-1}$ and at most to $t_{\max} = 2.5$ s for $f_{\mathrm{SR}} = 6\,\mathrm{min}^{-1}$.

The whole optimization problem (10.1) minimizes the deviation between the development of target $\boldsymbol{T}_h^*(t_k)$ and estimator-based temperature distributions $\bar{\boldsymbol{T}}_h(t_k)$ in the three stages at the beginning of stroke h using the available control variables. These are the austenitizing temperature T_γ, which enters the model in the tempering stage as an initial value, the air pressure p_{Air} for cooling A_1 and the heating temperature $T_{\mathrm{Heat}} = T_\gamma$ of A_2 in the tempering stage. Furthermore the stroke rate f_{SR} is the only control variable with an influence in all three simulated stages. All these parameters are set at the beginning of stroke h and stay constant for the whole holding step. When this is finished, a new parameter set is calculated for the next stroke $h + 1$. The estimated temperature is determined by the designed Kalman filter.

The control design is integrated into the production process for creating a produced blank, offering the flexibility to adjust control variables at the beginning of each stage of this multistage setup. During the individual stages, control is not feasible, given the parameters are not tunable. Moreover, the control design enhances product quality through a stitch-to-stitch regulation approach. The data and insights employed for one finished blank contribute to enhancing the production of subsequent blanks.

Fig. 10.4 shows two specifications of the target temperature trajectories $\boldsymbol{T}^*(t_k)$ at three selected points over the three simulated stages. While positions 1 and 2 are placed in A_2 of the blank, position 3 lays in A_1 (see Fig. 10.4(e)). These positions represent relevant points at the blank, because they are placed in both areas and include different hardness thinning developments during the two forming steps. It would also be possible to select more or other positions. Fig. 10.4(c) and 10.4(d) depict the trajectories. In the tempering stage these are equal within the same area, while they differ afterwards. For the evaluation it should be noted that the process is not fully controllable so that not every temperature trajectory can be realized. The reasons are model related physical limits of the temperature development during the multistage press hardening process and the limited actuation options. The possible trajectories differ in such a way that it is worth to implement the designed optimal control problem for the controllable subspace of this multistage press hardening process.

Fig. 10.4 also shows two specifications of the target hardness distribution $\boldsymbol{H}^*$ (see Fig. 10.4(a)) and one thinning distribution $\Delta\boldsymbol{s}^*$ (see Fig. 10.4(b)). All are defined along the x_2-direction at $x_1 = 0$ mm (green nodes of Fig. 8.1), while the mid part (central light gray area of Fig. 8.5(d)) is neglected. The hardness is chosen to be $\boldsymbol{H}_1^* = 220$ HV in A_1 and the center of A_2, while it is $\boldsymbol{H}_1^* = 400$ HV at the boundaries of A_2. The second specification has $\boldsymbol{H}_2^* = 420$ HV in the whole blank. The sheet thinning always has five peaks resulting from the forming stages (compare with Fig. 10.4(e)). The defined target values for these peaks are each 0.15 mm or 0.1 mm, for

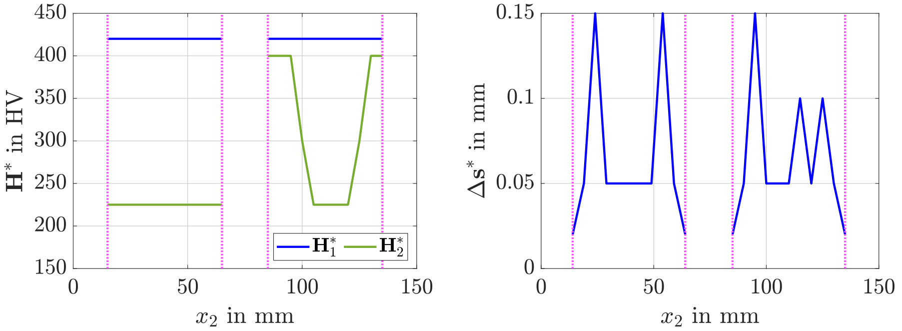

(a) Target hardness distributions $\boldsymbol{H}^*$.

(b) Target sheet thinning $\Delta \boldsymbol{s}^*$.

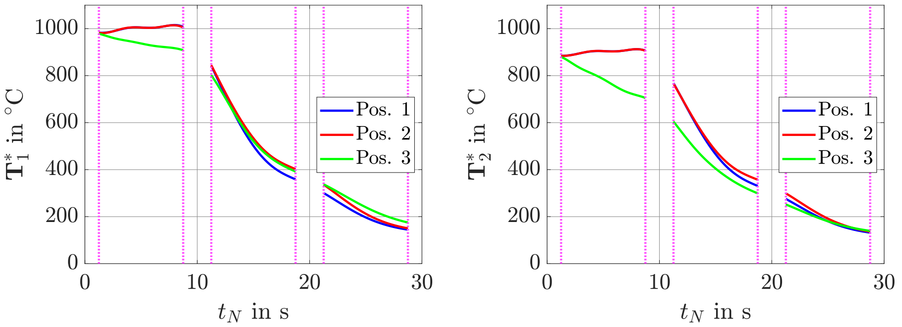

(c) Target temperature trajectories $\boldsymbol{T}_1^*(t_k)$.

(d) Target temperature trajectories $\boldsymbol{T}_2^*(t_k)$.

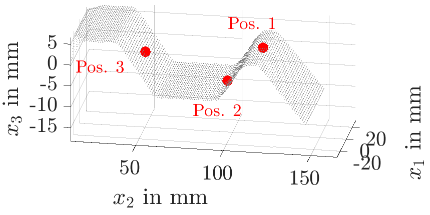

(e) Selected positions.

Figure 10.4.: Target property distributions $\boldsymbol{H}^*$, $\Delta \boldsymbol{s}^*$ and target temperature trajectories $\boldsymbol{T}^*(t_k)$ for the selected positions.

the area boundaries 0.025 mm and for the rest 0.05 mm. It is worth mentioning that also the properties are not fully controllable as only some target distributions are possible to reach. In the upcoming Chapter 11 these temperature trajectories and property distributions are used in an experimental validation of this control approach.

11. Experimental Validation

The subsequent chapter provides the experimental validation of the previously outlined theoretical framework from the whole Part II. Commencing with an overview, Section 11.1 details the experimental setup. Subsequently, Section 11.2 critically assesses the model's accuracy, as expounded in Chapter 8. This section encompasses both an analysis of the control variables' functionality and a direct comparison between the simulation and measurement outputs. Moving forward, Section 11.3 validates the functionality of the estimator (9.5), evaluating its real-time capability. Finally, in Section 11.4, the validation of the controller (10.1) at the multistage forming plant is presented.

11.1. Experimental Setup

The process underlying the experiment is comprehensively detailed in Chapter 7. The material examined throughout the four consecutive stages is a 22MnB5 steel with a thickness $s = 2\,\mathrm{mm}$. An example of a completed blank is depicted in Fig. 11.1.

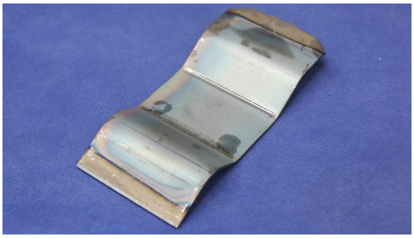

Figure 11.1.: Completed blank after the multistage press hardening process.

The stages are arranged within a progressive die, which is mounted within a servo-hydraulic press (MSD2-400 from Schuler) as illustrated in Fig.11.2(a). This press is connected to a programmable logic controller (PLC, central gray device), allowing for adjustment of the stroke rate f_{SR}. On the right side of the image is a computer, where the model, estimator, and controller are programmed using LabVIEW. In Fig.11.2(b), a snapshot of the ongoing process is presented. At this point, the press is open, the thermal imaging camera is active, the thermocouples do not have contact to the blanks, and the pyrometers measure at shifted wrong positions. The blanks have already been transferred to the next stage, which will be followed by the closure

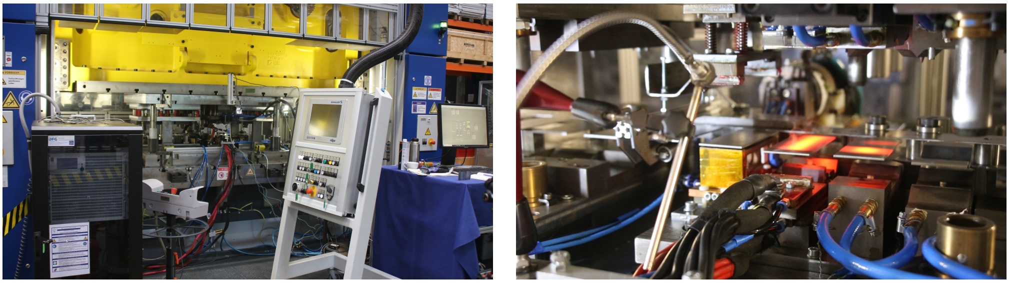

(a) Servo-hydraulic press with a mounted progressive die and the PLC.

(b) Snapshot of the ongoing process after the transfer step.

(c) Snapshot of the ongoing process during the holding step.

(d) Snapshot of the ongoing process after the transfer step with side view.

Figure 11.2.: Pictures of the experimental setup.

of the press. Fig.11.2(c) provides a snapshot of the holding step. Here, the camera cannot be used, while the thermocouples and pyrometers measure at the chosen positions. In Fig.11.2(d) the process with opened press is seen from a side view. Many precut blanks are seen, while only four of them are placed in the active stages. For the inductive heating in the initial stage a 40 kW generator (TrueHeat MF 7040 from Trumpf) is utilized. Temperature measurement during austenitizing is accomplished using a pyrometer (Metis M318 from Sensortherm) and controlled through a PID controller. Moving on to the second stage, the air pressure p_{Air} for cooling in A_1 is regulated using a controllable valve (VPPM from Festo), while A_2 is heated by a 44 kW DC generator (LAB/HP 4020 from FE-Systems) located on the left side in Fig. 11.2(a). In the third stage, the application of the blank holder force F_{BH} is facilitated by a hydraulic cylinder, with hydraulic pressure adjustment achieved through a pressure-limiting valve (PMV 41-43 from HAWE).

In Fig.11.3, an illustration of the various measurement instruments is provided. The positions of the four thermocouples (spring-loaded surface thermocouples of type K from Therma) are indicated by red circles in Fig.11.3(a). These thermocouples are connected to the computer through a data acquisition device (RedLab-2408-2AO from Meilhaus Electronics). Fig.11.3(b) displays the placement of the pyrometer utilized during the austenitizing stage, also marked with

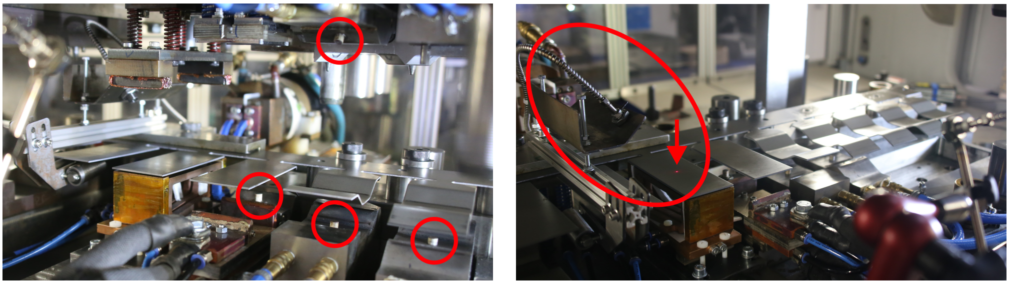

(a) Positions of the four thermocouples $\boldsymbol{y}$ indicated by red circles.

(b) Placement of the pyrometer y_γ utilized during the austenitizing stage (red circle).

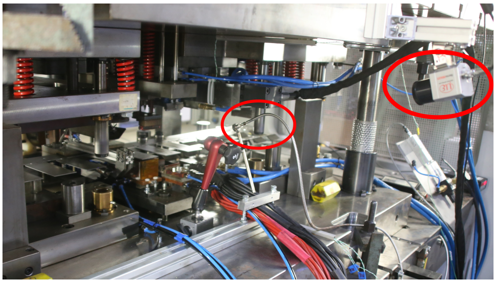

(c) Placement of the pyrometer y_4 utilized during the tempering stage and thermal imaging camera $\boldsymbol{y}_{\text{th}}$ (red circles).

Figure 11.3.: Pictures of the different measurement instruments.

a red circle. On the blank, the measurement position is indicated by a red laser point (marked by the red arrow). In Fig.11.3(c), both the second pyrometer (Metis M318 from Sensortherm), which is used for A_2 in the tempering stage and the thermal imaging camera (TIM-M1, Micro Epsilon) are highlighted in red. The pyrometers are linked to the PID controllers, which, in turn, are connected to the computer. The camera is directly linked to the computer.

11.2. Model Validation

In a first step the measurement instruments are used to identify and validate the impact of the process parameters on the system dynamics. Afterwards the temperature developments of the sensors are compared with those from the FE simulation (see Section 8.1).

11.2.1. Impact of the Control Variables

In order to depict the outputs of the control relevant measurement instruments on the one hand and to visualize the influence of the different control variables, on the other hand the outputs are compared for varying inputs in Fig 11.4. The comparisons are chosen in a way, that every input and output is visualized once. The chosen control variables are $f_{\mathrm{SR}} = 6\,\mathrm{min}^{-1}$, $T_\gamma = T_{\mathrm{Heat}} = 900\,^\circ\mathrm{C}$, $p_{\mathrm{Air}} = 0\,\mathrm{bar}$ and $F_{\mathrm{BH}} = 5\,\mathrm{kN}$, with the exception of the respective varying parameter. In every figure measurements of the holding steps of the sixth stroke are shown, so the timeline starts at $t = 50\,\mathrm{s}$.

The selection of the stroke rate f_{SR} impacts all stages of the process, including austenitization, tempering, stretch-forming, and die bending. A higher stroke rate f_{SR} results in a shorter holding time τ_{Ho}, consequently reducing the cooling time during the forming stages. This leads to higher temperatures at the end of the process. This effect is illustrated in Fig. 11.4(a) for $f_{\mathrm{SR}} = 6\,\mathrm{min}^{-1}$, $f_{\mathrm{SR}} = 7\,\mathrm{min}^{-1}$ and $f_{\mathrm{SR}} = 8\,\mathrm{min}^{-1}$ through the thermocouple y_3 observed during the die bending stage. To facilitate comparison, the time is normalized using $t_N = t(f_{\mathrm{SR},h}/6\,\mathrm{min}^{-1})$.

The austenitizing temperature T_γ serves as a initial value for the model of the successive stages 2 to 4. Fig. 11.4(b) depicts the temperature evolution for $T_\gamma = 900\,^\circ\mathrm{C}$, $T_\gamma = 950\,^\circ\mathrm{C}$ and $T_\gamma = 1000\,^\circ\mathrm{C}$ at the pyrometer y_γ. After a waiting time of about 2 s the generator controlled with the PID gadget starts heating up the blank with a nearly constant rate. The dwell time t_γ at the austenitizing temperature T_γ within the holding step of this stroke is about 2 s.

The heating temperature T_{Heat} influences A_2 in the tempering stage. The temperature evolution for $T_{\mathrm{Heat}} = 900\,^\circ\mathrm{C}$ and the case of a deactivated generator at the pyrometer y_4 are depicted in Fig. 11.4(c). After a waiting time of about 2 s the generator with the PID controller starts heating up the blank to the desired temperature. When the generator remains inactive, the temperature exhibits a nearly linear decrease at a consistent rate.

The cooling pressure p_{Air} influences A_1 in the tempering stage. Fig. 11.4(d) depicts the temperature evolution for $p_{\mathrm{Air}} = 0\,\mathrm{bar}$, $p_{\mathrm{Air}} = 2\,\mathrm{bar}$ and $p_{\mathrm{Air}} = 4\,\mathrm{bar}$ at the thermocouple y_1. As already elaborated in Section 8.3 a higher pressure leads to a higher cooling rate, and the difference between $p_{\mathrm{Air}} = 2\,\mathrm{bar}$ and $p_{\mathrm{Air}} = 4\,\mathrm{bar}$ is much small than between $p_{\mathrm{Air}} = 0\,\mathrm{bar}$ and $p_{\mathrm{Air}} = 2\,\mathrm{bar}$.

The blank holder force F_{BH} influences the stretch-forming stage. The unknown and insignificancy small impact towards the temperature evolution has been discussed in Section 8.3. This finding can be confirmed in Fig. 11.4(e) and 11.4(f) with the comparison of $F_{\mathrm{BH}} = 1\,\mathrm{kN}$ and $F_{\mathrm{BH}} = 5\,\mathrm{kN}$ at the thermocouples y_2 and y_5.

11.2.2. Model Comparison

In order to prove the validity of the underlying process model developed in Chapter 8, the outputs $\boldsymbol{y}$ are compared with the FE simulation results for identical process parameters in terms of $\boldsymbol{T}_{\mathrm{Sim}}$ at the same positions in Fig. 11.5 and 11.6. Here, no estimator or controller is used, the process

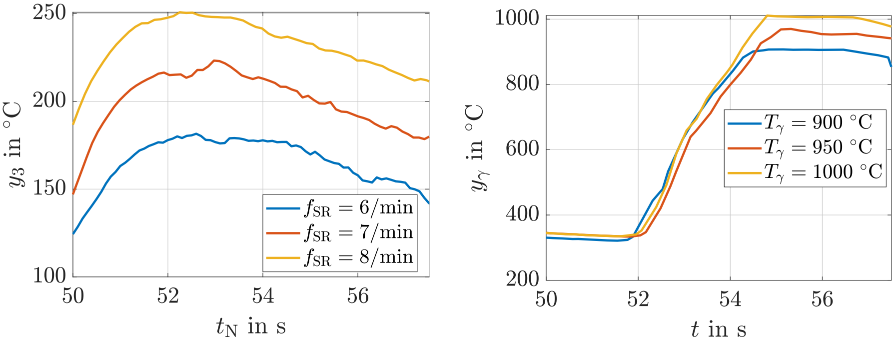

(a) Impact of different stroke rates f_{SR} at thermocouple y_3.

(b) Impact of different austenitizing temperatures T_γ at pyrometer y_γ.

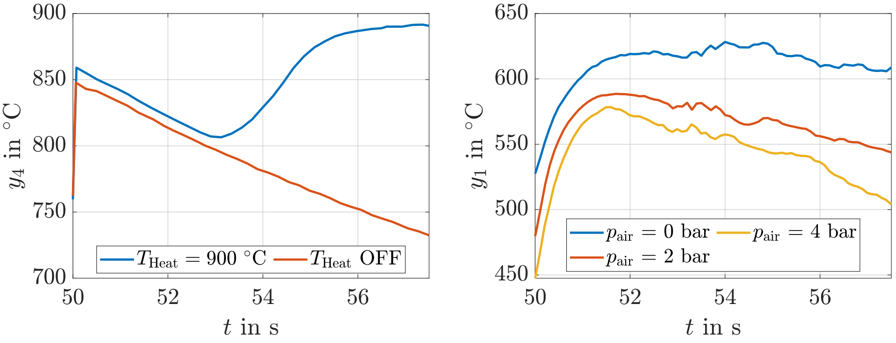

(c) Impact of different heating temperatures T_{Heat} at pyrometer y_4.

(d) Impact of different cooling pressures p_{Air} at thermocouple y_1.

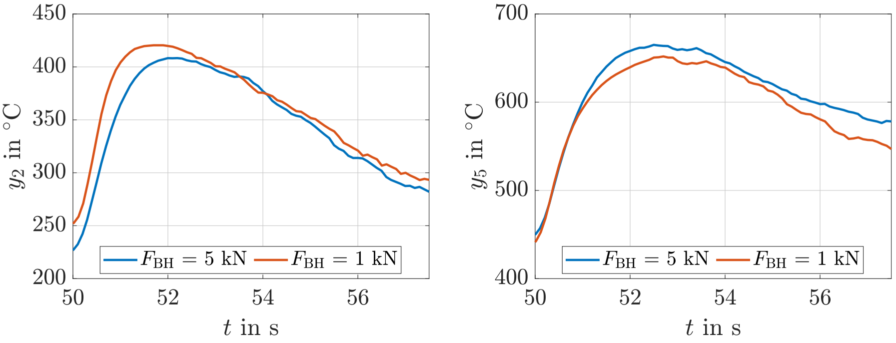

(e) Impact of different blank holder forces F_{BH} at thermocouple y_2.

(f) Impact of different blank holder forces F_{BH} at thermocouple y_5.

Figure 11.4.: Impact of the control variables at different measurement positions.

is carried out open loop. The chosen control variables are $f_{\mathrm{SR}} = 6\,\mathrm{min}^{-1}$, $T_\gamma = T_{\mathrm{Heat}} = 950\,°\mathrm{C}$, $p_{\mathrm{Air}} = 2\,\mathrm{bar}$ and $F_{\mathrm{BH}} = 5\,\mathrm{kN}$.

In Fig. 11.5(a) the output value y_1 of the first thermocouple (yellow) is compared with the FE simulation $T_{\mathrm{Sim},37}$ at the same position (blue). The difference is quite large, but with the adjustments of Chapter 9, the consideration of the delay of the thermocouples (see (9.5)) and the offset for the first thermocouple (9.3), the temperature developments show similar behaviors. For visualization the delay is added to the simulation gaining $T_{\mathrm{Sim},37,\mathrm{PT1}}$ (red) and the offset to the sensor gaining $y_1 + y_{1,\mathrm{Off}}$ (violet).

The output of the pyrometer y_4 shows a different behavior than the simulation $T_{\mathrm{Sim},93}$ at the same point. As discussed in Chapter 10 a PID-controller aims to reach the target value T_{Heat} at this position. The controller in the simulation acts faster and stronger than in the measurement. As the target value is nearly reached in the end of the stroke this difference is not significant for the next stages.

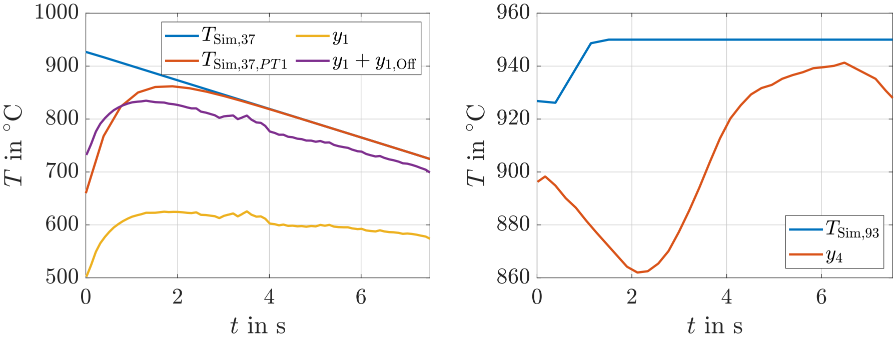

(a) Comparison of $T_{\mathrm{Sim},37}$ and y_1.

(b) Comparison of $T_{\mathrm{Sim},93}$ and y_4.

Figure 11.5.: Comparison of the FE simulation $\boldsymbol{T}_{\mathrm{Sim}}$ and the measurements at thermocouple y_1 and pyrometer y_4 in the tempering stage.

In Fig. 11.6(a) the output value y_2 of the second thermocouple (yellow) is compared with the FE simulation $T_{\mathrm{Sim},60}$ at the same position (blue). When adding the delay behavior to the simulated temperature development $T_{\mathrm{Sim},60,\mathrm{PT1}}$ both the system dynamics and the temperature range of simulation and measurement fit quite well. The same observation can be made for the output y_3 and simulation $T_{\mathrm{Sim},60,\mathrm{PT1}}$ in Fig. 11.6(b) and output y_5 and simulation $T_{\mathrm{Sim},90,\mathrm{PT1}}$ in Fig. 11.6(c).

11.3. Estimator Validation

In the closed loop setup, where estimator (9.5) and controller (10.1) are activated, estimated $\hat{\boldsymbol{y}}$ and real measurement outputs $\boldsymbol{y}$ are compared in order to verify the functionality of the developed

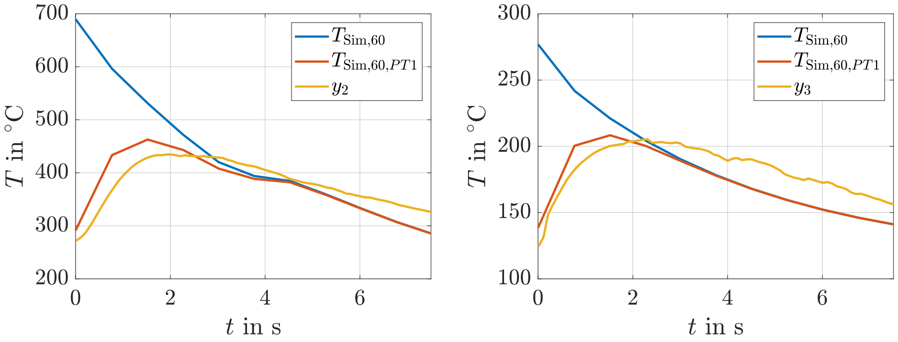

(a) Comparison of $T_{\mathrm{Sim},60}$ and y_2.

(b) Comparison of $T_{\mathrm{Sim},60}$ and y_3.

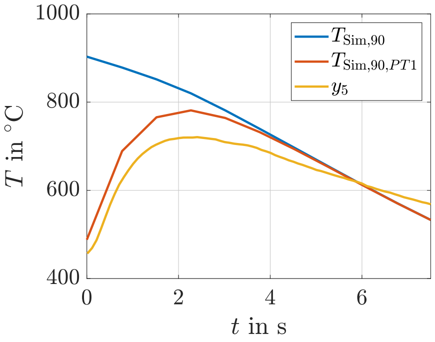

(c) Comparison of $T_{\mathrm{Sim},90}$ and y_5.

Figure 11.6.: Comparison of the FE simulation T_{Sim} and the measurements at thermocouple y_2, y_3 and y_5 in the stretch-forming and die bending stages.

estimator in a scenario with ten successive strokes. The resulting control variable configuration is listed in Tab. 11.1. Two finished blanks are taken into account for this evaluation in Fig. 11.7. The target temperature trajectories from the first are $\boldsymbol{T}_1^*(t_k)$ and those from the second $\boldsymbol{T}_2^*(t_k)$, both depicted in Fig. 10.4. The temperatures of both blanks are simulated and measured over stages 2 to 4. The holding steps of these stages are depicted, where their ends and beginnings are marked with dashed violet lines. Since $t = 0$ holds for the start of the whole scenario, the comparisons start at different time points. The control variable configuration for the whole first blank is $f_{\mathrm{SR}} = 6\,\mathrm{min}^{-1}$, $T_\gamma = 1000\,°\mathrm{C}$, $T_{\mathrm{Heat}} = 1000\,°\mathrm{C}$, $p_{\mathrm{Air}} = 0\,\mathrm{bar}$ and $F_{\mathrm{BH}} = 5\,\mathrm{kN}$. For the second one it is $f_{\mathrm{SR}} = 6\,\mathrm{min}^{-1}$, $T_\gamma = 900\,°\mathrm{C}$, $T_{\mathrm{Heat}} = 900\,°\mathrm{C}$, $p_{\mathrm{Air}} = 2\,\mathrm{bar}$ and $F_{\mathrm{BH}} = 5\,\mathrm{kN}$. All sensor outputs $\boldsymbol{y}$ and the estimated ones $\hat{\boldsymbol{y}}$ merge very fast for both blanks, as shown in Fig. 11.7(a) and 11.7(b). This leads to the small estimation errors $\tilde{\boldsymbol{y}}$ with $\tilde{y}_i = |y_i - \hat{y}_i|$ for $i = 1, 2, \ldots, 5$ in Fig. 11.7(c) and 11.7(d).

In order to gain more convenience about the functionality of the estimator, the estimated temperature distribution $\hat{\boldsymbol{T}}$ of the second compared blank is depicted in Fig. 11.8. The temperature

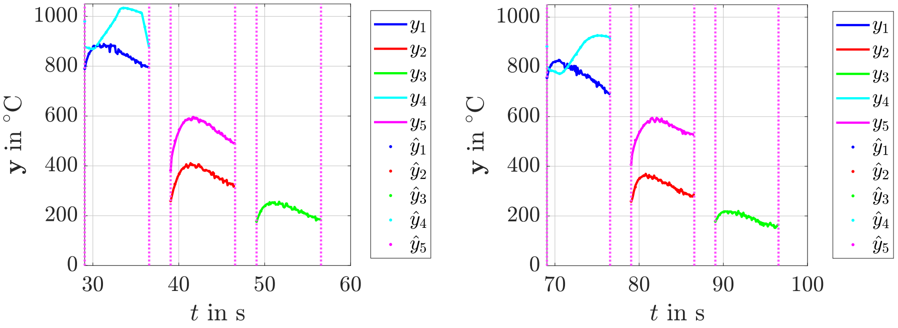

(a) Estimated outputs $\hat{\boldsymbol{y}}$ and measurements $\boldsymbol{y}$ in the first blank.

(b) Estimated outputs $\hat{\boldsymbol{y}}$ and measurements $\boldsymbol{y}$ in the second blank.

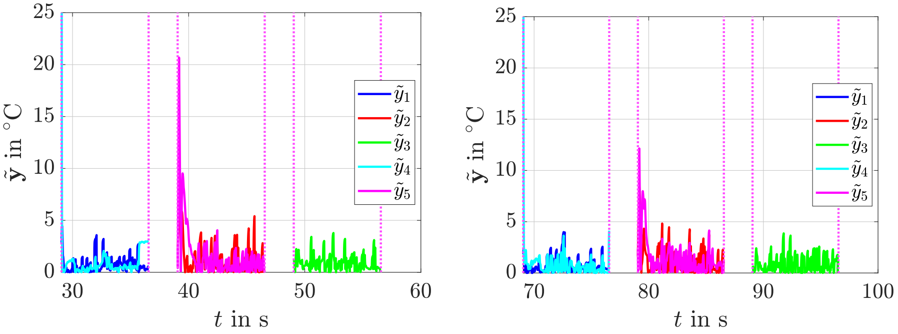

(c) Estimation errors $\tilde{\boldsymbol{y}}$ in the first blank.

(d) Estimation errors $\tilde{\boldsymbol{y}}$ in the second blank.

Figure 11.7.: Temperature development of estimated outputs $\hat{\boldsymbol{y}}$, measurements $\boldsymbol{y}$ and estimation errors $\tilde{\boldsymbol{y}}$ over stages 2,3 and 4 in two produced blanks.

is only estimated at $x_1 = 0$ and is supposed to be constant for varying x_1 (see Section 8.1). The legend of the temperature distribution throughout this stroke is shown below in Fig. 11.8. Every simulated stage is shown with four snapshots. The spatial and temporal temperature development is very plausible. At the beginning the temperature distribution is nearly uniform. During the first stage the temperature in A_1 decreases, while it stays nearly constant in A_2. This can concluded from the cooling pressure $p_{\mathrm{Air}} = 2\,\mathrm{bar}$ in A_1 and the heating temperature $T_{\mathrm{Heat}} = T_\gamma = 900\,°\mathrm{C}$ in A_2. During the stretch-forming stage, the temperature continues to drop, due to the blank's contact with the cold tools. In the areas, where the metal is stretched by the punch the temperature stays higher. This can especially be seen in A_2, as it starts with a higher temperature value. Also during the die bending stage, the blank's cooling continues. A small area with higher temperature can be located at the stretched blank in A_2. Beside the higher starting temperature value from the previous stage, this side is also bent, which leads to the development of forming heat.

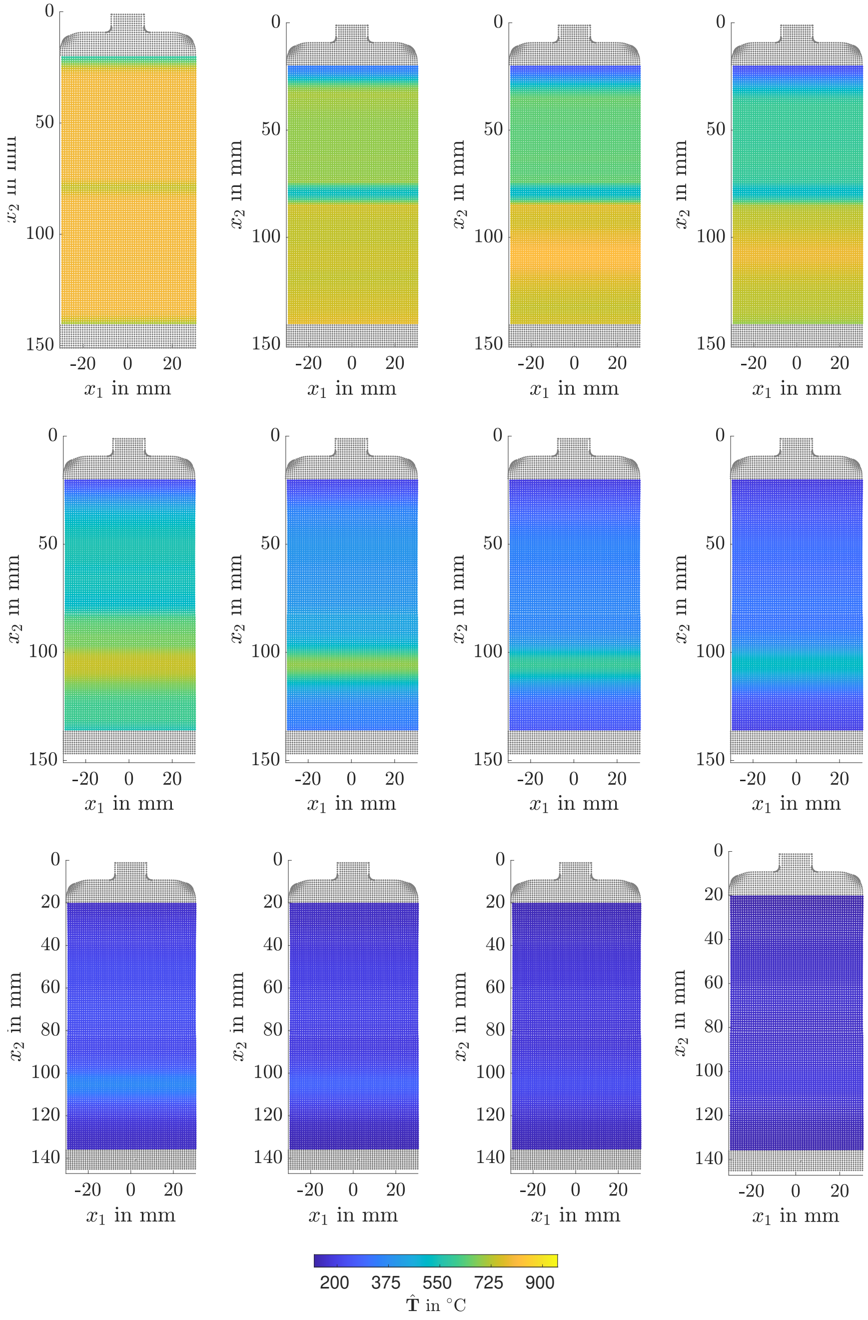

Figure 11.8.: Estimated temperature distribution $\hat{T}$ over stages 2,3 and 4 in the second compared blank.

11.4. Controller Validation

This section analyzes the functionality of the developed controller (10.1). The solution of the optimal control problem takes about 0.5 s and is therefore real-time applicable. It is implemented as a Python function, where the objectives for all possible parameter configurations are calculated and the minimum one is chosen. This function is integrated in a LabVIEW project, which contains the whole control loop including all measurement and actuation devices. In the optimal temperature control problem, time t_k of $\boldsymbol{T}^*(t_k)$ is normalized via $t_{k,N} = t_k(f_{\mathrm{SR},h}/6\,\mathrm{min}^{-1})$ in order to be valid for all possible stroke rates f_{SR}. The process is not fully controllable, as only some target temperature trajectory $\boldsymbol{T}^*(t_k)$ are possible to reach. These are chosen by the property control in such a way that they fit with the simulative temperature developments of the different control variable configurations.

To validate its functionality the control is tested in a real experiment with ten consecutive strokes. Fig. 10.4 depicts the target property distributions of hardness $\boldsymbol{H}^*$ and sheet thinning $\Delta\boldsymbol{s}^*$ and the target temperature trajectories $\boldsymbol{T}^*(t_k)$. While the target hardness distribution $\boldsymbol{H}_1^*$ (blue lines) in Fig. 10.4(a) holds for the first six strokes, the target distribution changes to $\boldsymbol{H}_2^*$ (green lines) for the next four strokes. The target sheet thinning $\Delta\boldsymbol{s}^*$ for all ten strokes is visualized in Fig. 10.4(b). The target temperature trajectories $\boldsymbol{T}^*(t_k)$ are chosen with the evaluation of the property control (see Section 10.1). They are depicted for three positions on the blank (see Fig. 10.4(e)). Fig. 10.4(c) shows the trajectories $\boldsymbol{T}_1^*(t_k)$ for the first six strokes and Fig. 10.4(d) $\boldsymbol{T}_2^*(t_k)$ for the last four ones.

Fig. 11.9 now shows the experimental results and compares them with the target temperature trajectories $\boldsymbol{T}^*(t_k)$ from Fig. 10.4. These are visualized with solid lines and the estimated temperatures $\hat{\boldsymbol{T}}(t_k)$ with dotted lines. In Fig. 11.9(a), the first finished blank is evaluated after it has passed through four stages. The diagram includes the holding steps of the tempering, stretch-forming and die bending stage, which are marked with the violet dashed lines. The austenitizing stage is not part of the temperature model. The difference between target and estimated trajectory is acceptably small. The same desired temperature development is given in Fig. 11.9(b). This blank was produced from stroke $h = 3$ to $h = 6$. The control variable configuration is improved by the solution of the optimal control problem 10.1, as the air pressure is now continuously $p_{\mathrm{Air}} = 0\,\mathrm{bar}$ and the stroke rate predominantly $f_{\mathrm{SR}} = 6\,\mathrm{min}^{-1}$. This leads to a difference between target and result, which is even smaller than before and can especially be seen in the stretch-forming stage.

As discussed, the target temperature trajectories $\boldsymbol{T}^*(t_k)$ changes with the start of stroke $h = 7$. Fig. 11.9(c) depicts the product from stroke $h = 5$ to $h = 8$. This includes the trajectory change. The depicted $\boldsymbol{T}^*(t_k)$ is still the old one in the tempering stage and the new one in the two forming stages. In spite of that difficulty the difference is acceptably small again. The finished blank in Fig. 11.9(d) totally aims to reach the new target trajectories $\boldsymbol{T}^*(t_k)$. Since this control problem now has coherent target temperature trajectories $\boldsymbol{T}^*(t_k)$, the difference is even smaller than in the previous discussed case.

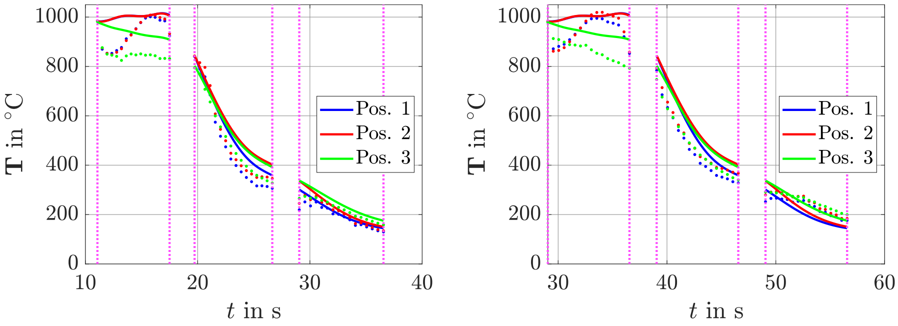

(a) Blank produced in strokes $h = 1$ to $h = 4$. (b) Blank produced in strokes $h = 3$ to $h = 6$.

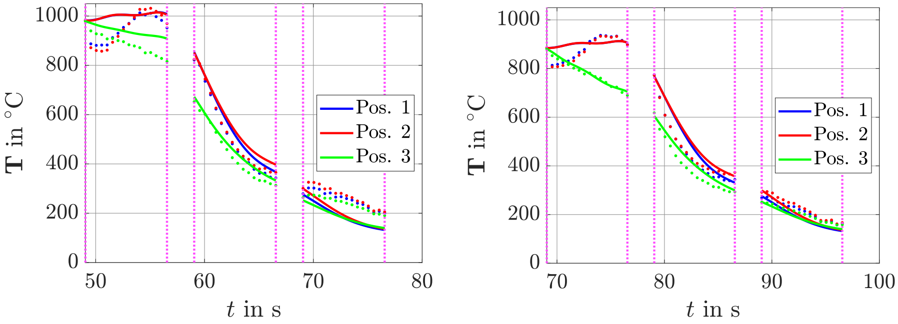

(c) Blank produced in strokes $h = 5$ to $h = 8$. (d) Blank produced in strokes $h = 7$ to $h = 10$.

Figure 11.9.: Target temperature trajectories $\boldsymbol{T}^*(t_k)$ (solid lines) and estimated temperature developments $\hat{\boldsymbol{T}}(t_k)$ (dotted lines) in three positions over stages 2,3 and 4 for four finished blanks.

The evolution of the control variables over the strokes is given in Tab. 11.1. The austenitizing temperature T_γ and the dependent heating T_{Heat} are always the same, for the same target trajectory $\boldsymbol{T}^*(t_k)$. The first value of T_{Heat} is given in the second stroke, because in the first stroke only the austenitizing stage is active. The optimal stroke rate f_{SR} varies for the first $\boldsymbol{T}^*(t_k)$ between $6\,\text{min}^{-1}$ and $7\,\text{min}^{-1}$ until it reaches the calculated optimal result $f_{\text{SR}} = 6\,\text{min}^{-1}$. For the second $\boldsymbol{T}^*(t_k)$ the stroke rate $f_{\text{SR}} = 6\,\text{min}^{-1}$ is directly reached. The air pressure behaves in a similar way until reaching $p_{\text{Air}} = 0\,\text{bar}$ for the first target trajectory and $p_{\text{Air}} = 2\,\text{bar}$ for the second one. Blank holder force F_{BH} is calculated by the property control and is not affected by the optimal temperature control. Its first value in stroke $h = 3$ is $F_{\text{BH}} = 5\,\text{kN}$, which holds for the whole process. In an uncontrolled process it is not possible to change the parameters between the stages in the production of a finished blank. This enables a faster correction of not optimal control variable configurations and proves the advantage of the designed controller.

Stroke h	$f_{\mathrm{SR},h}$ in min^{-1}	$T_{\gamma,h}$ in °C	$T_{\mathrm{Heat},h}$ in °C	$p_{\mathrm{Air},h}$ in bar	$F_{\mathrm{BH},h}$ in kN
1	6	1000	-	-	-
2	7	1000	1000	2	-
3	6.5	1000	1000	0	5
4	6	1000	1000	0	5
5	6	1000	1000	0	5
6	6	1000	1000	0	5
7	6	900	900	2	5
8	6	900	900	2	5
9	6	900	900	2	5
10	6	900	900	2	5

Table 11.1.: Development of the control variables over the strokes.

The last validation step of the controller's functionality is the comparison of the target property distributions with the actual ones. Both hardness and sheet thinning of finished blanks are not measured within the control loop as they are only fed back via the soft sensors (see Section 10.1). They are measured afterwards following the methodology outlined in [47] with the hardness tester (Dia Testor 2 RC, Wolpert) according to HV10 and the coordinate measuring machine (PRISMO VAST 5 HTG from Zeiss) to prove the control success.

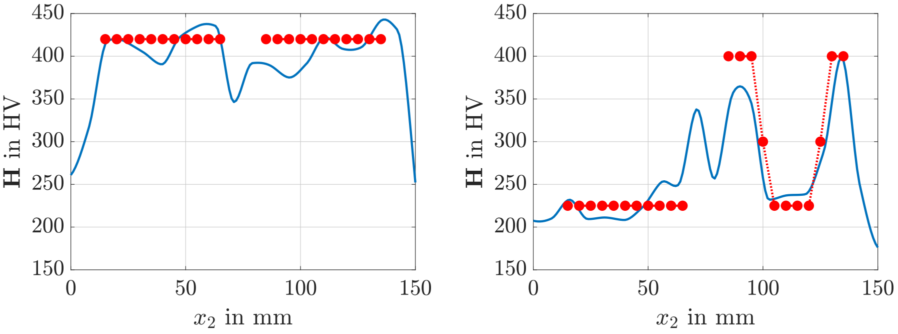

(a) Blank produced in strokes $h = 3$ to $h = 6$.

(b) Blank produced in strokes $h = 7$ to $h = 10$.

Figure 11.10.: Measured hardness distribution $\boldsymbol{H}$ along the x_2-direction (blue line) and target hardness $\boldsymbol{H}^*$ (red connected points) of two finished blanks.

Fig. 11.10 visualizes the target hardness distributions $\boldsymbol{H}^*$ with connected red points and the measured ones $\boldsymbol{H}$ with solid lines. In Fig. 11.10(a) the blank finished in stroke $h = 6$ is depicted. The difference between target $\boldsymbol{H}_1^*$ and measurement is quite small in the two areas A_1 and A_2. A target hardness is not defined in the rest of the blank. The same can be said for hardness $\boldsymbol{H}_2^*$ for the blank finished in stroke $h = 10$ (see Fig. 11.10(b)). As the two target hardness distributions $\boldsymbol{H}_1^*$ and $\boldsymbol{H}_2^*$ differ a lot, it can be concluded that the property control is able to achieve products with various hardness profiles by the definition of target temperature trajectories $\boldsymbol{T}^*(t_k)$ and the adjustment of control variables.

Fig. 11.11 visualizes the sheet thinning distribution $\Delta\boldsymbol{s}^*$ of the blank finished after stroke $h = 10$ with connected red points and the measured one $\Delta\boldsymbol{s}$ with solid lines. This property mainly depends on the blank holder force F_{BH}. By setting $F_{\mathrm{BH}} = 5\,\mathrm{kN}$ during the whole process the difference between target and measurement is very small.

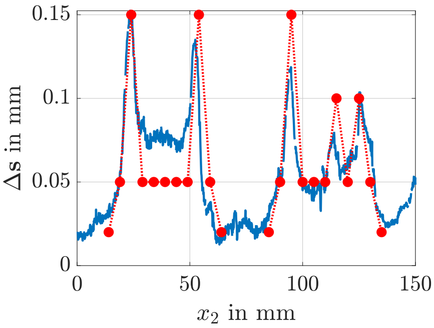

Figure 11.11.: Measured sheet thinning distribution $\Delta\boldsymbol{s}$ along the x_2-direction (blue line) and target sheet thinning $\Delta\boldsymbol{s}^*$ (red connected points) of the finished blank produced in strokes $h = 7$ to $h = 10$.

The applicability of this consistent design process is clearly supported by the experimental results obtained and the performance of the estimator-based control concept to achieve the desired target temperature trajectories during the multistage press hardening process is confirmed. This, in turn, allows for the implementation of product property control, which is designed with the aim of reaching the desired hardness $\boldsymbol{H}^*$ and sheet thinning $\Delta\boldsymbol{s}^*$ at the end of the process. Further evaluations and potential improvements of the presented approach will be addressed in Chapter 12 and 13 of Part III.

Part III.

Concluding Remarks

12. Summary

This chapter provides a summary from the results of Parts I and II.

Model-Based Temperature Control for a Deep Drawing Process

In Part I a temperature control strategy is developed for a deep drawing tool with embedded actuation and sensing devices to reduce wrinkles and cracks by increasing the formability of the metal sheet to be formed.

Based on a continuum model of the spatial-temporal temperature distribution in the die a finite element approximation is deduced. By systematically making use of model order reduction techniques the large-scale approximation is projected onto a suitable subspace of significantly smaller dimension to obtain a model setup that can be used for control and estimator design. A parameter identification is performed based on experimental data to determine the heating power of the actuators and the heat transfer coefficient. Optimal sensor placement is performed using a suitable optimization strategy involving the determined reduced order models. The sensor locations obtained from different cost functionals in terms of the observability Gramian are compared based by setting up a Kalman filter to evaluate the resulting estimation performance. This serves as basis for the targeted intervention by built-in actuators. The best result was achieved by maximizing the smallest eigenvalue of the reduced order model obtained by balanced truncation. The estimator-based feedback control is set up as a linear-quadratic regulator extended by an integral part to react efficiently to disturbances. Furthermore a PD controller is designed in order to compare the results. For the experimental validation the system design in terms of optimal sensor placement is realized in an experimental forming tool and the developed control strategies involving the estimator based on a reduced order model is implemented under real-time requirements. As a result, the LQ regulator leads to better performances, if steady-state of the temperature distribution is not reached.

The obtained experimental results clearly support the applicability of this consistent design process and illustrate the performance of the estimation and control concept to maintain desired prescribed local target temperatures during forming. It is also shown that in a scenario with multiple consecutive forming steps the demanded temperature can be kept at the prescribed level. Possible improvements of the presented approach in future research are summarized 13.

Data-Based Control of a Multistage Press Hardening Process

In Part II a data-driven estimation and the control of the resulting temperature trajectories are developed and evaluated for a multistage press hardening process with a sheet material in a progressive die in order to control the product properties of the formed blanks.

Based on data generated by a high fidelity FE simulation model realized in `LSDyna` for three subsequent process stages (tempering, stretch-forming, and die bending) a reduced order model is determined using DMD. An extension to a parameter-dependent formulation including the process parameters stroke rate, blank holder force, and austenitization temperature, is proposed to enable the adjustment of the process parameters during estimation and control. It is shown that the simulation results for the parametric DMD model and the original FE model match rather accurately despite the reduction of the computational time from hours to milliseconds. In order to improve model accuracy, the influence of the control variable parameters is analyzed experimentally. With this information the model is certainly adjusted. Different instruments are used for temperature measurement during the process. These are described, compared and their dynamics are identified. The estimation of the spatial-temporal temperature distribution is addressed by developing a Kalman filter based on the parametric DMD model. Herein, a time varying or stage-dependent, respectively, output matrix is considered to represent the different number and location of thermocouples in the three stages. In order to reach a desired temperature trajectory throughout the process, an optimal control is implemented. As a consequence the geometry and properties of the blank can be influenced in a targeted manner. For the experimental validation the system design is realized in an experimental setup and the developed control strategy involving the estimator based on a reduced order model is implemented under real-time requirements.

The applicability of model, estimator and controller is clearly supported by the experimental results obtained. The aim of achieving the desired target temperature trajectories during the multistage press hardening process is confirmed. However, there are many ideas, how to improve the presented approach.

General Findings

Two different metal forming processes, which differ in complexity and objective, are discussed throughout this thesis. The first one is a singlestage deep drawing process, where the temperature distribution of the die, which is equipped with thermocouples and actuators, is controlled in combination with a model-based estimation concept, in order to reduce the occurrence of wrinkles and cracks. The second one is a multistage press hardening process, where the development of the temperature distribution in the blank, which can be influenced with by constant process parameters is controlled together with a temperature estimation. Here, the aim is to control the product properties using the temperature knowledge. With these two different setups several methods are investigated for temperature modeling, estimation and control.

The temperature modeling of both the die and the blank involves deriving and applying the heat equation, followed by spatial discretization using finite element analysis. Various techniques for order reduction are employed to enable real-time implementation. For the deep drawing process, model-based methods like balanced truncation are used, while data-based dynamic mode decomposition is applied for the multistage process. This technique is expanded to accommodate parameter-dependent formulations that account for different process parameters. Additionally, model and actuator parameter identification methods are performed using experimental data to enhance model accuracy.

An optimal sensor placement strategy is devised for the deep drawing tool to achieve efficient temperature estimation. This framework can also be adapted to address the dual problem of optimal actuator placement for temperature control. In the case of the multistage process, various measurement instruments are employed, compared, and their dynamics identified. In both setups, a Kalman filter is deployed as a state estimator. The feedback control for temperature distribution in the die is established as a linear-quadratic regulator extended with an integral component in the deep drawing process, while in the other setup, feedback is only applied before each stroke. This allows for solving an optimal control problem to manage the entire temperature evolution in the blank.

13. Outlook

This chapter concludes the thesis with some suggestions of possible improvements and ideas for further research.

Model-Based Temperature Control for a Deep Drawing Process

The obtained experimental results clearly support the applicability of the design process of Part I and confirm the control and estimation performance to maintain desired prescribed local target temperatures during forming. It is also shown that in a scenario with multiple consecutive forming steps the demanded temperature can be kept at the demanded level. Possible improvements of the presented approach in future research are summarized subsequently.

Within the project only the local heating of one half of the tool, the bottom die, is considered. It is also possible to think of a local heating of the punch of the tool in order to reduce the cooling of the die as a result of a forming process. Other aspects can be the heating of the blank before forming or the targeted use of oil at the die's surface. These adjustments could also improve the formability. An evaluation of the process performance with the usage of blanks, which have other properties is worth investigating, since the calotted blank have had much less wrinkles and cracks than the standard one (see Chapter 6).

Moreover, the placement of another sensor could improve the validation of the estimator. This enables the possibility to proof the functionality of the Kalman filter using all placed sensors. Furthermore, another optimization algorithm can be used to compare the results of the optimal sensor placement problem. Here, a simple greedy algorithm as discussed in [72] could be considered. As already pointed out the number of sensors can be fixed to reduce the complexity of the sensor placement problem. It is important to test this framework in a production line with higher stroke rate, as the maximum number of forming operations per time interval at which the actuator and the controller can reliably operate has not been evaluated in this work. However, a significant improvement has been achieved to maintain the operating condition by the proposed temperature control.

Data-Based Control of a Multistage Press Hardening Process

The applicability of model, estimator and controller of Part II is clearly supported by the experimental results obtained. The aim of achieving the desired target temperature trajectories during the multistage press hardening process is confirmed. However, there are many ideas, how to improve the presented approach. As already mentioned in Section 10.1 the predicted final properties hardness and sheet thinning can be used to define the target temperatures in the property control. An interesting aspect lies in the transferability of the model, estimator, and control design to other materials, such as X46Cr13, and to modifications or additions of stages to the process. To assess the applicability of the approach, the data basis for the reduced dynamic mode decomposition model can be adapted.

Other aspects are changes in actuation and sensing. In addition to the spring-loaded thermocouples a sensor placement in the die of the forming tool is possible. In contrast to all previous measurement instruments, the temperature can be evaluated permanently, during both holding and transfer step. The information of the tool's temperature could be used for the implementation of a disturbance estimator similar to [59]. The thermal imaging camera can be implemented in the closed control loop. With this knowledge the so far previously identified thermocouple offsets can be calculated online. The measurements from thermocouples, pyrometer and camera can also be used for the design of a filter bank. It is furthermore possible to carry out an optimal sensor placement problem, in order to find useful positions as done for the deep drawing process in Chapter 4. Moreover, the placement of another sensor could improve the validation of the estimator.

While snapshots of a FE simulation are the data basis for dynamic mode decomposition so far, a possible improvement could be the addition of experimental data to this basis. Another possibility is the extension of the reduced system in order to take model inaccuracies into account. For this purpose, a low-rank perturbation of the dynamic matrix can be generated based on the linear time-invariant model structure through a matrix to be determined based on the available measurement data. This matrix could be included in the previous setup and estimated adaptively via a Kalman filter [68]. The controllable subspace of this process is limited to the placed actuators. In order to increase this subspace the implementation of additional actuators like heating coils or cartridges could be useful. Furthermore, the design of the parametric dynamic mode decomposition could be improved by other interpolation methods, like the Gaussian process regression, as already discussed. An important aspect is the testing under industrial manufacturing conditions with several successive strokes. However, a significant improvement has been achieved to reach the desired temperature trajectories by the proposed estimation and control. This enables the possibility to achieve the desired final product properties.

Final Remarks

In this chapter many suggestions have been made for future research. Beside experimental improvements like the implementation of validation sensors, the main objects are robustness and transferability of model, estimator and controller. In this context experiments should run under industrial manufacturing conditions and with the forming of different materials. However, model, estimator and controller were developed for two different metal forming processes, and their effectiveness could be proved. Finally, this thesis clearly supports the usage of control theory methods in metal forming processes.

List of Figures

List of Tables

Bibliography

[1] J. M. Allwood, S. R. Duncan, J. Cao, P. Groche, G. Hirt, B. Kinsey, T. Kuboki, M. Liewald, A. Sterzing, and A. E. Tekkaya. “Closed-loop control of product properties in metal forming”. In: *CIRP Annals* 65.2 (2016), pp. 573–596. DOI: `10.1016/j.cirp.2016.06.002`.

[2] J. Andrej and T. Meurer. “Flatness-based constrained optimal control of reaction-diffusion systems”. In: *2018 Annual American Control Conference (ACC)*. IEEE, 2018, pp. 2539–2544. DOI: `10.23919/ACC.2018.8431201`.

[3] A. C. Antoulas. *Approximation of Large-Scale Dynamical Systems*. Philadelphia: Society for Industrial and Applied Mathematics, 2005. DOI: `10.1137/1.9780898718713`.

[4] A. K. Aziz and P. Monk. “Continuous finite elements in space and time for the heat equation”. In: *Mathematics of Computation* 52.186 (1989), pp. 255–274. DOI: `10.1090/S0025-5718-1989-0983310-2`.

[5] M. Bambach, J. Buhl, T. Hart-Rawung, M. Lechner, and M. Merklein. “Towards virtual deformation dilatometry for the design of hot stamping process”. In: *Procedia Engineering* 207 (2017), pp. 1821–1826. DOI: `10.1016/j.proeng.2017.10.945`.

[6] E. Barocio, B. C. Pal, N. F. Thornhill, and A. R. Messina. “A dynamic mode decomposition framework for global power system oscillation analysis”. In: *IEEE Transactions on Power Systems* 30.6 (2014), pp. 2902–2912. DOI: `10.1109/TPWRS.2014.2368078`.

[7] C. Beattie and S. Gugercin. “Model reduction by rational interpolation”. In: *Model Reduction and Approximation: Theory and Algorithms*. Ed. by P. Benner, M. Ohlberger, A. Cohen, and K. Willcox. 1st ed. Philadelphia: Society for Industrial and Applied Mathematics, 2017. Chap. 7, pp. 297–334.

[8] P. Benner, S. Gugercin, and K. Willcox. “A Survey of Projection-Based Model Reduction Methods for Parametric Dynamical Systems”. In: *SIAM Review* 57.4 (2015), pp. 483–531. DOI: `10.1137/130932715`.

[9] P. Benner, R. Herzog, N. Lang, I. Riedel, and J. Saak. “Comparison of model order reduction methods for optimal sensor placement for thermo-elastic models”. In: *Engineering Optimization* 51.3 (2019), pp. 465–483. DOI: `10.1080/0305215X.2018.1469133`.

[10] P. Benner, C. Himpe, and T. Mitchell. “On reduced input-output dynamic mode decomposition”. In: *Advances in Computational Mathematics* 44.6 (2018), pp. 1751–1768. DOI: `10.1007/s10444-018-9592-x`.

[11] P. Benner, P. Kürschner, and J. Saak. “An improved numerical method for balanced truncation for symmetric second-order systems”. In: *Mathematical and Computer Modelling of Dynamical Systems* 19.6 (2013), pp. 593–615. DOI: `10.1080/13873954.2013.794363`.

[12] P. Benner and J. Saak. *Linear-Quadratic Regulator Design for Optimal Cooling of Steel Profiles.* Preprint SFB393/05-05. Sonderforschungsbereich 393 - Parallele Numerische Simulation für Physik und Kontinuumsmechanik, Chemnitz University of Technology, 2005.

[13] T. Böhm and T. Meurer. "Trajectory planning and tracking control for the temperature distribution in a deep drawing tool". In: *Control Engineering Practice* 64 (2017), pp. 127–139. DOI: `10.1016/j.conengprac.2017.04.004`.

[14] V. Boljanovic. "Sheet Metal Forming Processes and Die Design". In: 2nd ed. South Norwalk: Industrial Press, Inc., 2014. Chap. 6 Deep Drawing, pp. 87–113.

[15] S. L. Brunton and J. N. Kutz. "Data-Driven Science and Engineering: Machine Learning, Dynamical Systems, and Control". In: Cambridge University Press, 2019. Chap. 9 Balanced Models for Control, pp. 321–344.

[16] A. Castagnotto, M. Cruz Varona, L. Jeschek, and B. Lohmann. "sss & sssMOR: Analysis and Reduction of Large-Scale Dynamic Systems in MATLAB". In: *at-Automatisierungstechnik* 65.2 (2017), pp. 134–150. DOI: `10.1515/auto-2016-0137`.

[17] P. R. N. Childs, J. R. Greenwood, and C. A. Long. "Review of temperature measurement". In: *Review of Scientific Instruments* 71.8 (2000), pp. 2959–2978. DOI: `10.1063/1.1305516`.

[18] D. R. Cooper, K. E. Rossie, and T. G. Gutowski. "The energy requirements and environmental impacts of sheet metal forming: An analysis of five forming processes". In: *Journal of Materials Processing Technology* 244 (2017), pp. 116–135. DOI: `10.1016/j.jmatprotec.2017.01.010`.

[19] N. Demazel, H. Laurent, J. Coër, M. Carin, P. Le Masson, J. Favero, R. Canivenc, and H. Salmon-Legagneur. "Investigation of the progressive hot die stamping of a complex boron steel part using numerical simulations and Gleeble tests". In: *The International Journal of Advanced Manufacturing Technology* 99.1 (2018), pp. 803–817. DOI: `10.1007/s00170-018-2532-6`.

[20] N. B. Erichson, L. Mathelin, J. N. Kutz, and S. L. Brunton. "Randomized Dynamic Mode Decomposition". In: *SIAM Journal on Applied Dynamical Systems* 18.4 (2019), pp. 1867–1891. DOI: `10.1137/18M1215013`.

[21] K. Ersoy-Nürnberg, G. Nürnberg, M. Golle, and H. Hoffmann. "Simulation of wear on sheet metal forming tools—An energy approach". In: *Wear* 265.11-12 (2008), pp. 1801–1807. DOI: `10.1016/j.wear.2008.04.039`.

[22] J. Fisher and R. Bhattacharya. "Linear quadratic regulation of systems with stochastic parameter uncertainties". In: *Automatica* 45.12 (2009), pp. 2831–2841. DOI: `10.1016/j.automatica.2009.10.001`.

[23] M. Fliess, J. Lévine, P. Martin, and P. Rouchon. "Flatness and defect of non-linear systems: introductory theory and examples". In: *International Journal of Control* 61.6 (1995), pp. 1327–1361. DOI: `10.1080/00207179508921959`.

[24] A. Gelb. *Applied Optimal Estimation.* 1st ed. Cambridge: MIT Press, 1974.

[25] G. H. Golub, P. C. Hansen, and D. P. O'Leary. "Tikhonov Regularization and Total Least Squares". In: *SIAM Journal on Matrix Analysis and Applications* 21.1 (1999), pp. 185–194. DOI: `10.1137/S0895479897326432`.

[26] Z. Gronostajski, Z. Pater, L. Madej, A. Gontarz, L. Lisiecki, A. Łukas-zek-Sołek, J. Łuksza, S. Mróz, Z. Muskalski, W. Muzykiewicz, M. Pietrzyk, R. E. Śliwa, J. Tomczak, S. Wiewiórowska, G. Winiarski, J. Zasadziński, and S. Ziółkiewicz. "Recent development trends in metal forming". In: *Archives of Civil and Mechanical Engineering* 19.3 (2019), pp. 898–941. DOI: `10.1016/j.acme.2019.04.005`.

[27] S. Gugercin, A. Antoulas, and C. Beattie. "H2 Model Reduction for Large-Scale Linear Dynamical Systems". In: *SIAM Journal on Matrix Analysis and Applications* 30.2 (2008), pp. 609–638. DOI: `10.1137/060666123`.

[28] P. Hippchen, A. Lipp, H. Grass, P. Craighero, M. Fleischer, and M. Merklein. "Modelling kinetics of phase transformation for the indirect hot stamping process to focus on car body parts with tailored properties". In: *Journal of Materials Processing Technology* 228 (2016), pp. 59–67. DOI: `10.1016/j.jmatprotec.2015.01.003`.

[29] P. Hippe. "Prevention of Controller Windup". In: *Windup in Control: Its Effects and Their Prevention*. London: Springer, 2006. Chap. 2, pp. 21–57. DOI: `10.1007/1-84628-323-X_2`.

[30] B. Hochholdinger. "Simulation des Presshärteprozesses und Vorhersage der mechanischen Bauteileigenschaften nach dem Härten". Dissertation. ETH Zürich, 2012.

[31] W. Homberg, B. Arian, V. Arne, T. Borgert, A. Brosius, P. Groche, C. Hartmann, L. Kersting, R. Laue, J. Martschin, T. Meurer, D. Spies, A. E. Tekkaya, A. Trächtler, W. Volk, F. Wendler, and M. Wrobel. "Softsensors: key component of property control in forming technology". In: *Production Engineering* (2023). DOI: `10.1007/s11740-023-01227-1`.

[32] C.-W. Hsu, A. G. Ulsoy, and M. Y. Demeri. "Development of process control in sheet metal forming". In: *Journal of Materials Processing Technology* 127.3 (2002), pp. 361–368. DOI: `10.1016/S0924-0136(02)00321-7`.

[33] Q. A. Huhn, M. E. Tano, J. C. Ragusa, and Y. Choi. "Parametric dynamic mode decomposition for reduced order modeling". In: *Journal of Computational Physics* 475 (2023). 111852. DOI: `10.1016/j.jcp.2022.111852`.

[34] G. Ingarao, R. Di Lorenzo, and F. Micari. "Sustainability issues in sheet metal forming processes: an overview". In: *Journal of Cleaner Production* 19.4 (2011), pp. 337–347. DOI: `10.1016/j.jclepro.2010.10.005`.

[35] J. Jeswiet, M. Geiger, U. Engel, M. Kleiner, M. Schikorra, J. Duflou, R. Neugebauer, P. Bariani, and S. Bruschi. "Metal forming progress since 2000". In: *CIRP Journal of Manufacturing Science and Technology* 1.1 (2008), pp. 2–17. DOI: `10.1016/j.cirpj.2008.06.005`.

[36] S. Kakac, Y. Yener, and A. Pramuanjaroenkij. *Convective heat transfer*. 3rd ed. Boca Raton: CRC press, 2014.

[37] R. E. Kalman. "A New Approach to Linear Filtering and Prediction Problems". In: *Journal of Basic Engineering* 82.1 (1960), pp. 35–45. DOI: `10.1115/1.3662552`.

[38] D. Kloeser, J. Martschin, T. Meurer, and E. Tekkaya. “Reduced order modelling for spatial-temporal temperature and property estimation in a multi-stage hot sheet metal forming process”. In: *Advances in Industrial and Manufacturing Engineering* 3 (2021). 100055. DOI: `10.1016/j.aime.2021.100055`.

[39] K. Kunisch and S. Volkwein. “Galerkin proper orthogonal decomposition methods for parabolic problems”. In: *Numerische Mathematik* 90.1 (Nov. 2001), pp. 117–148. DOI: `10.1007/s002110100282`.

[40] J. N. Kutz, S. L. Brunton, B. W. Brunton, and J. L. Proctor. *Dynamic Mode Decomposition: Data-Driven Modeling of Complex Systems.* Philadelphia: Society for Industrial and Applied Mathematics, 2016. DOI: `10.1137/1.9781611974508`.

[41] R. W. Lewis, K. Morgan, H. R. Thomas, and K. N. Seetharamu. *The finite element method in heat transfer analysis.* Chichester: John Wiley & Sons, 1996.

[42] G. Mamakoukas, I. Abraham, and T. D. Murphey. “Learning Stable Models for Prediction and Control”. In: *IEEE Transactions on Robotics* 39.3 (2023), pp. 2255–2275. DOI: `10.1109/TRO.2022.3228130`.

[43] J. Mann and J. N. Kutz. “Dynamic mode decomposition for financial trading strategies”. In: *Quantitative Finance* 16.11 (2016), pp. 1643–1655. DOI: `10.1080/14697688.2016.1170194`.

[44] K. Manohar, J. N. Kutz, and S. L. Brunton. “Optimal Sensor and Actuator Selection Using Balanced Model Reduction”. In: *IEEE Transactions on Automatic Control* 67.4 (2022), pp. 2108–2115. DOI: `10.1109/TAC.2021.3082502`.

[45] J. Martschin, P. Rethmann, J. Grodotzki, M. Wrobel, T. Meurer, and A. E. Tekkaya. “Quick prediction of thinning in stretch forming of hat-shaped profiles during multi-stage hot sheet metal forming”. In: *Journal of Materials Processing Technology* 327 (2024), p. 118365. DOI: `https://doi.org/10.1016/j.jmatprotec.2024.118365`.

[46] J. Martschin, M. Wrobel, J. Grodotzki, T. Meurer, and A. E. Tekkaya. “Soft Sensors for Property-Controlled Multi-Stage Press Hardening of 22MnB5”. In: *Automotive Innovation* 6 (2023), pp. 252–363. DOI: `10.1007/s42154-023-00238-z`.

[47] J. Martschin, M. Wrobel, J. Grodotzki, and A. E. Tekkaya. “Tailoring the Hardness in Multi-stage Press Hardening of 22MnB5 Sheet Material in a Progressive Die”. In: *Proceedings of the 14th International Conference on the Technology of Plasticity - Current Trends in the Technology of Plasticity.* Ed. by K. Mocellin, P. O. Bouchard, R. Bigot, and T. Balan. Cham: Springer Nature Switzerland, 2024, pp. 90–100. DOI: `10.1007/978-3-031-40920-2_10`.

[48] J. Martschin, M. Wrobel, T. Meurer, F. Kolpak, and A.E. Tekkaya. “Entwicklung von Softsensoren für das eigenschaftsgeregelte mehrstufige Presshärten”. In: *36. Aachener Stahlkolloquium – Umformtechnik “Ideen Form geben“.* Ed. by G. Hirt. Aachen: Verlagshaus Mainz GmbH, 2022, pp. 283–292.

[49] V. Mehrmann and T. Stykel. “Balanced Truncation Model Reduction for Large-Scale Systems in Descriptor Form”. In: *Dimension Reduction of Large-Scale Systems.* Ed. by P. Benner, D. C. Sorensen, and V. Mehrmann. Berlin, Heidelberg: Springer, 2005, pp. 83–115. DOI: `10.1007/3-540-27909-1_3`.

[50] T. Meurer and J. Andrej. “Flatness-based model predictive control of linear diffusion-convection-reaction processes”. In: *2018 IEEE Conference on Decision and Control (CDC)*. 2018, pp. 527–532. DOI: `10.1109/CDC.2018.8619837`.

[51] T. Meurer and M. Zeitz. “Feedforward and Feedback Tracking Control of Nonlinear Diffusion- Convection- Reaction Systems Using Summability Methods”. In: *Industrial & Engineering Chemistry Research* 44.8 (2005), pp. 2532–2548. DOI: `10.1021/ie0495729`.

[52] J. Saak, M. Köhler, and P. Benner. *M-M.E.S.S.-2.0.1 – The Matrix Equations Sparse Solvers library*. DOI:10.5281/zenodo.3606345. see also:`www.mpi-magdeburg.mpg.de/projects/mess`. Feb. 2020.

[53] K. Mori, T. Maeno, M. Sakagami, M. Ukai, and Y. Agatsuma. “2-stage progressive-die hot stamping of ultra-high strength steel parts using resistance heating”. In: *Procedia Engineering* 207 (2017), pp. 681–686. DOI: `10.1016/j.proeng.2017.10.1041`.

[54] K. Mori, T. Maeno, M. Tsuchiya, and T. Nanya. “Inclusion of hot stamping operations in progressive-die plate forging of tailored high strength gear part”. In: *The International Journal of Advanced Manufacturing Technology* 90.9 (2017), pp. 3585–3594. DOI: `10.1007/s00170-016-9705-y`.

[55] A. G. Nair, B. Strom, B. W. Brunton, and S. L. Brunton. “Phase-consistent dynamic mode decomposition from multiple overlapping spatial domains”. In: *Physical Review Fluids* 5.7 (2020), p. 074702. DOI: `10.1103/PhysRevFluids.5.074702`.

[56] T. Nestorović and M. Trajkov. “Optimal actuator and sensor placement based on balanced reduced models”. In: *Mechanical Systems and Signal Processing* 36.2 (2013), pp. 271–289. DOI: `10.1016/j.ymssp.2012.12.008`.

[57] T. Penzl. “A Cyclic Low-Rank Smith Method for Large Sparse Lyapunov Equations”. In: *SIAM Journal on Scientific Computing* 21.4 (1999), pp. 1401–1418. DOI: `10.1137/S1064827598347666`.

[58] J. L. Proctor, S. L. Brunton, and J. N. Kutz. “Dynamic mode decomposition with control”. In: *SIAM Journal on Applied Dynamical Systems* 15.1 (2016), pp. 142–161. DOI: `10.1137/15M1013857`.

[59] J. A. Profeta, W. G. Vogt, and M. H. Mickle. “Disturbance estimation and compensation in linear systems”. In: *IEEE Transactions on Aerospace and Electronic Systems* 26.2 (1990), pp. 225–231. DOI: `10.1109/7.53455`.

[60] F. Rathgeber, D. A. Ham, L. Mitchell, M. Lange, F. Luporini, A. T. T. McRae, G.-T. Bercea, G. R. Markall, and P. H. J. Kelly. “Firedrake: Automating the Finite Element Method by Composing Abstractions”. In: *ACM Transactions on Mathematical Software* 43.3 (2016), pp. 1–27. DOI: `10.1145/2998441`.

[61] M. Rathinam and L. R. Petzold. “A new look at proper orthogonal decomposition”. In: *SIAM Journal on Numerical Analysis* 41.5 (2003), pp. 1893–1925. DOI: `10.1137/S0036142901389049`.

[62] J. Saak. “Efficient numerical solution of large scale algebraic matrix equations in PDE control and model order reduction”. Dissertation. Chemnitz University of Technology, 2009.

[63] T. Sayadi, P. J. Schmid, F. Richecoeur, and D. Durox. “Parametrized data-driven decomposition for bifurcation analysis, with application to thermo-acoustically unstable systems”. In: *Physics of Fluids* 27.3 (2015). 037102. DOI: `10.1063/1.4913868`.

[64] P. J. Schmid. “Dynamic Mode Decomposition and Its Variants”. In: *Annual Review of Fluid Mechanics* 54.1 (2022), pp. 225–254. DOI: `10.1146/annurev-fluid-030121-015835`.

[65] P. J. Schmid. “Dynamic mode decomposition of numerical and experimental data”. In: *Journal of Fluid Mechanics* 656 (2010), pp. 5–28. DOI: `10.1017/S0022112010001217`.

[66] M. Serpas, G. Hackebeil, C. Laird, and J. Hahn. “Sensor location for nonlinear dynamic systems via observability analysis and MAX-DET optimization”. In: *Computers & Chemical Engineering* 48 (2013), pp. 105–112. DOI: `10.1016/j.compchemeng.2012.07.014`.

[67] A. Shapiro. “Finite element modeling of hot stamping”. In: *Steel Research International* 80.9 (2009), pp. 658–664. DOI: `10.2374/SRI08SP065`.

[68] D. Simon. “Kalman filtering with state constraints: a survey of linear and nonlinear algorithms”. In: *IET Control Theory & Applications* 4.8 (2010), pp. 1303–1318. DOI: `10.1049/iet-cta.2009.0032`.

[69] L. Sirovich. “Turbulence and the dynamics of coherent structures. III. Dynamics and scaling”. In: *Quarterly of Applied Mathematics* 45.3 (1987), pp. 583–590. DOI: `10.1090/qam/910464`.

[70] S. C. Stebner, J. Martschin, B. Arian, S. Dietrich, M. Feistle, S. Hütter, R. Lafarge, R. Laue, X. Li, C. Schulte, D. Spies, F. Thein, F. Wendler, M. Wrobel, J. Rozo Vasquez, M. Dölz, and S. Münstermann. “Monitoring the evolution of dimensional accuracy and product properties in property-controlled forming processes”. In: *Advances in Industrial and Manufacturing Engineering* 8 (2024). 100133. DOI: `10.1016/j.aime.2023.100133`.

[71] W. A. Strauss. *Partial differential equations: An introduction.* Hoboken: John Wiley & Sons, 2007.

[72] T. H. Summers, F. L. Cortesi, and J. Lygeros. “On Submodularity and Controllability in Complex Dynamical Networks”. In: *IEEE Transactions on Control of Network Systems* 3.1 (2016), pp. 91–101. DOI: `10.1109/TCNS.2015.2453711`.

[73] S. Toros, F. Ozturk, and I. Kacar. “Review of warm forming of aluminum–magnesium alloys”. In: *Journal of Materials Processing Technology* 207.1-3 (2008), pp. 1–12. DOI: `10.1016/j.jmatprotec.2008.03.057`.

[74] M. Wrobel, J. Martschin, T. Meurer, and E. Tekkaya. “Data-Driven Temperature Estimation for a Multi-Stage Press Hardening Process”. In: *IFAC-PapersOnLine* 56.2 (2023). 22nd IFAC World Congress, pp. 4252–4257. DOI: `10.1016/j.ifacol.2023.10.1785`.

[75] M. Wrobel and T. Meurer. “Optimal sensor placement and estimator-based temperature control for a deep drawing process”. In: *Journal of Process Control* 124 (2023), pp. 92–104. DOI: `10.1016/j.jprocont.2023.02.014`.

[76] M. Wrobel and T. Meurer. “Optimal Sensor Placement for Temperature Control in a Deep Drawing Tool”. In: *IFAC-PapersOnLine* 54.11 (2021). 6th IFAC Workshop on Mining, Mineral and Metal Processing, pp. 91–96. DOI: `10.1016/j.ifacol.2021.10.056`.

[77] M. Wrobel and T. Meurer. “Optimale Sensorplatzierung für die Temperaturregelung in einem Tiefziehwerkzeug”. In: *Tagungsband GMA-Fachausschuss 1.40 Systemtheorie und Regelungstechnik*. Ed. by T. Meurer, F. Woittennek, and A. Schaum. Christian-Albrechts-Univeristät zu Kiel, Lehrstuhl für Regelungstechnik, 2021, pp. 183–193.

[78] P. C. Young and J. C. Willems. “An approach to the linear multivariable servomechanism problem”. In: *International Journal of Control* 15.5 (1972), pp. 961–979. DOI: `10.1080/00207177208932211`.

[79] O. C. Zienkiewicz, R. L. Taylor, and J. Z. Zhu. *The Finite Element Method: Its Basis and Fundamentals*. 6th ed. Oxford: Elsevier Butterworth-Heinemann, 2013.

A. Appendix

Optimal $\mathcal{H}_2$ approximation

The $\mathcal{H}_2$ norm is defined as

$$\|H\|_{\mathcal{H}_2} = \left(\frac{1}{2\pi} \int_{-\infty}^{\infty} \left\| H(i\omega) \right\|_F^2 \right),$$

where $\|M\|_F$ denotes the Frobenius norm of a complex matrix M. The difference between the full order system $H(s)$ and the reduced model $H_r(s)$ leads to the optimization problem

$$\|H - H_r\|_{\mathcal{H}_2} = \min_{\dim(\tilde{H}_r)=r} \left\| H - \tilde{H}_r \right\|_{\mathcal{H}_2}.$$

The optimality conditions can be formulated as

$$\begin{aligned} H(-\lambda_i)\boldsymbol{r}_i &= H_r(-\lambda_i)\boldsymbol{r}_i, \\ \boldsymbol{l}_i^T H(-\lambda_i) &= \boldsymbol{l}_i^T H_r(-\lambda_i), \\ \boldsymbol{l}_i^T \frac{dH}{ds}(-\lambda_i)\boldsymbol{r}_i &= \boldsymbol{l}_i^T \frac{dH_r}{ds}(-\lambda_i)\boldsymbol{r}_i, \end{aligned}$$

for $i = 1, \ldots, r$. Specifically, when seeking an optimal $\mathcal{H}_2$ approximation denoted as $H_r(s)$, it is essential that this approximation takes the form of a bitangential Hermite interpolant to the original function $H(s)$. This theorem establishes a direct link between optimal model reduction and interpolation. The key parameters for this interpolation, namely the optimal interpolation points and tangent directions, are determined using the pole-residue representation of $H_r(s)$. The optimal interpolation points correspond to the mirrored positions of the poles of $H_r(s)$, reflected across the imaginary axis. Additionally, the ideal tangent directions are derived from the residue directions associated with each pole.

List of Publications

Journal Articles

1. M. Wrobel and T. Meurer. “Optimal sensor placement and estimator-based temperature control for a deep drawing process”. In: Journal of Process Control 124 (2023), pp. 92–104. doi: 10.1016/j.jprocont.2023.02.014. [75]
2. J. Martschin, M. Wrobel, J. Grodotzki, T. Meurer, and A. E. Tekkaya. “Soft Sensors for Property-Controlled Multi-Stage Press Hardening of 22MnB5”. In: Automotive Innovation 6 (2023), pp. 252–363. doi: 10.1007/s42154-023-00238-z. [46]
3. W. Homberg, B. Arian, V. Arne, T. Borgert, A. Brosius, P. Groche, C. Hartmann, L. Kersting, R. Laue, J. Martschin, T. Meurer, D. Spies, A. E. Tekkaya, A. Trächtler, W. Volk, F. Wendler, and M. Wrobel. “Softsensors: key component of property control in forming technology”. In: Production Engineering (2023). doi: 10.1007/s11740-023-01227-1. [31]
4. S. C. Stebner, J. Martschin, B. Arian, S. Dietrich, M. Feistle, S. Hütter, R. Lafarge, R. Laue, X. Li, C. Schulte, D. Spies, F. Thein, F. Wendler, M. Wrobel, J. Rozo Vasquez, M. Dölz, and S. Münstermann. “Monitoring the evolution of dimensional accuracy and product properties in property-controlled forming processes”. In: Advances in Industrial and Manufacturing Engineering 8 (2024). 100133. doi: 10.1016/j.aime.2023.100133. [70]
5. J. Martschin, P. Rethmann, J. Grodotzki, M. Wrobel, T. Meurer, and A. E. Tekkaya. “Quick prediction of thinning in stretch forming of hat-shaped profiles during multi-stage hot sheet metal forming”. In: Journal of Materials Processing Technology 327 (2024), p. 118365. doi: https://doi.org/10.1016/j.jmatprotec.2024.118365. [45]
6. M. Wrobel, J. Martschin, A. E. Tekkaya, and T. Meurer. “Data-based Control of a Multistage Press Hardening Process”. In progress.

Conference Contributions

1. M. Wrobel and T. Meurer. “Optimal Sensor Placement for Temperature Control in a Deep Drawing Tool”. In: IFAC-PapersOnLine 54.11 (2021). 6th IFAC Workshop on Mining, Mineral and Metal Processing, pp. 91–96. doi: 10.1016/j.ifacol.2021.10.056. [76]

2. M. Wrobel and T. Meurer. “Optimale Sensorplatzierung für die Temperaturregelung in einem Tiefziehwerkzeug”. In: Tagungsband GMA-Fachausschuss 1.40 Systemtheorie und Regelungstechnik. Ed. by T. Meurer, F. Woittennek, and A. Schaum. Christian-Albrechts-Univeristät zu Kiel, Lehrstuhl für Regelungstechnik, 2021, pp. 183–193. [77]
3. J. Martschin, M. Wrobel, T. Meurer, F. Kolpak, and A.E. Tekkaya. “Entwicklung von Softsensoren für das eigenschaftsgeregelte mehrstufige Presshärten”. In: 36. Aachener Stahlkolloquium – Umformtechnik “Ideen Form geben“. Ed. by G. Hirt. Aachen: Verlagshaus Mainz GmbH, 2022, pp. 283–292. [48]
4. M. Wrobel, J. Martschin, T. Meurer, and E. Tekkaya. “Data-Driven Temperature Estimation for a Multi-Stage Press Hardening Process”. In: IFAC-PapersOnLine 56.2 (2023). 22nd IFAC World Congress, pp. 4252–4257. doi: 10.1016/j.ifacol.2023.10.1785. [74]
5. J. Martschin, M. Wrobel, J. Grodotzki, and A. E. Tekkaya. “Tailoring the Hardness in Multi-stage Press Hardening of 22MnB5 Sheet Material in a Progressive Die”. In: Proceedings of the 14th International Conference on the Technology of Plasticity - Current Trends in the Technology of Plasticity. Ed. by K. Mocellin, P. O. Bouchard, R. Bigot, and T. Balan. Cham: Springer Nature Switzerland, 2024, pp. 90–100. doi: 10.1007/978-3-031-40920-2_10. [47]

Fortschrittsberichte aus der Regelungstechnik
und Prozessautomatisierung

Band 02

Herausgeber: Prof. Dr.-Ing. habil. Thomas Meurer

This work considers the model- and data-based estimation and control design for two distinct metal forming processes.

Deep drawing poses challenges such as wrinkle formation and crack occurrence, especially in geometrically complex areas. To enhance material formability and reduce defects, this work focuses on precisely controlling the temperature of the deep-drawing mold's die. It employs a systematic placement of sensors to develop a spatial-temporal temperature estimator, which is subsequently utilized for tracking control through embedded actuation devices. The proposed theoretical framework is experimentally validated.

In the context of multistage press hardening, where a sheet undergoes rapid austenitization, tempering, stretch-forming, and die bending, the resulting product properties are influenced by the thermo-mechanical history. This work aims to estimate and directly control the spatial-temporal temperature distribution in the sheet by developing a data-driven estimation in order to control the product properties of the formed blanks. Experimental validation of the system design and control strategy is conducted.

ISSN 2943-0887